Precursor Phases in Non-classical Crystallization

Dissertation
zur Erlangung des akademischen Grades
"doctor rerum naturalium"
(Dr. rer. nat.)
in der Wissenschaftsdisziplin
Kolloidchemie

eingereicht an der
Mathematisch-Naturwissenschaftlichen Fakultät
der Universität Potsdam
angegertigt am
Max−Planck−Institut für Kolloid− und Grenzflächenforschung Potsdam

von
Yuan Jiang

Potsdam, 13.10.2010

Published online at the
Institutional Repository of the University of Potsdam:
URL http://opus.kobv.de/ubp/volltexte/2011/5246/
URN urn:nbn:de:kobv:517-opus-52460
http://nbn-resolving.de/urn:nbn:de:kobv:517-opus-52460

Independence Declaration

I declare that I have not submitted this work at any other university. The thesis has been made independently.

Date & Place Signature

Abstract

Yuan Jiang
The Max Planck Institute of Colloids and Interfaces

Precursor Phases in Non-classical Crystallization

The main objective of this thesis is to understand molecular crystallization as a multistep process with or without polymeric additives, including transient liquid-liquid phase separation, nanocrystal nucleation within the dense phase, and subsequent nanocrystal self-assembly or self-organization in sequence.

The thesis starts with a quaternary model system, containing DL-Glutamic acid (Glu), polyethyleneimine (PEI), water, and EtOH, for the understanding of multistep precipitation of Glu with PEI as an additive. The experiments were performed by mixing Glu-PEI aqueous solution with a non-solvent EtOH. First, the phase diagram of the quaternary system is determined, obtaining precipitate, coacervates, or homogeneous mixtures by varying Glu/PEI *w/w* and water/EtOH *v/v*. Coacervation is observed to occur over a wide range of Glu/PEI with various volumes. The composition of coacervates is conveniently characterized by nuclear magnetic resonance spectroscopy. The observed coacervates are thermodynamically stable phases rich in solute, which is different from metastable polymer-induced liquid precursors. The combination of atomic force microscopy, small angle scattering, and ξ-potential measurements confirms the coexistence of monomers and Glu/PEI complexes and the aggregation of complexes in Glu-PEI-water systems. This suggests that there might be a direct structural transformation between the Glu-PEI complexes in aqueous solution and the metastable liquid precursors in a water-EtOH mixture.

The multistep mechanism of Glu precipitation with PEI as an additive is investigated thereafter. The combination of stopped flow and small angle scattering demonstrates that the initially formed liquid precursors pass through an alteration of growth and coalescence. Combined with results from optical microscopy and scanning electron microscopy, the nucleation of nanoplatelets happens within each liquid precursor droplet, and nanoplatelets reorient themselves and self-organize into a radial orientation in the

crystalline microspheres. The recipe was then extended to the precipitation of organics in other oppositely charged amino acid-polyelectrolyte systems.

After the success in preparing hierarchical microspheres in solution, the similar recipe can be extended to the preparation of patterned thin films on substrate. By dipping a quaternary DL-Lys·HCl (Lys)–polyacrylic acid (PAA)–water–EtOH dispersion on a hydrophilic slide, the fast evaporation process of the volatile solvent EtOH is responsible for the homogeneous nucleation of NPs. Then, the following complete evaporation causes the mesocrystallization of a continuous spherulitic thin film along the receding line of the liquid, which again transforms into a mesocrystalline thin film. Furthermore, annealing is used to optimize the property of mesocrystalline thin films. As evaporation is a non-equilibrium process, it can be used to tune the kinetics of crystallization. Therefore, hierarchical or periodical thin films are obtainable by starting the evaporation from microspheres recrystallization, obtaining mesocrystalline thin films with 4 hierarchy levels. The results reveal that evaporation provides an easy but effective way for the formation of patterned structures via the positioning of NPs after their fast nucleation, resulting in different kinds of patterns by controlling the concentration of NPs, solvent evaporation rate, and other physical forces.

Non-classical crystallization is not limited to crystallizations with polymeric additives. We also observed the nucleation and growth of a new molecular layer on the growing DL-Glu·H_2O crystals from a supersaturated mother liquor by using an in-situ atomic force microscopy (AFM), where the nucleation and growth of a molecular layer proceed via amorphous nanoparticle (NP) attachment and relaxation process before the observation of the growth of a newly formed molecular layer. NP attachment to the crystal surface is too fast to observe by using in-situ AFM. The height shrinkage of NPs, combined to the structural transformation from 3D amorphous NPs to 2D crystalline layer, is observed during the relaxation process. The nucleation and growth of a newly formed molecular layer from NP relaxation is contradictory to the classical nucleation theory, which hypothesizes that nuclei show the same crystallographic properties as a bulk crystal. The formation of a molecular layer by NP attachment and relaxation rather than attachment of single molecules provides a different picture from the currently held classical nucleation and growth theory regarding the growth of single crystals from solution.

Zusammenfassung

Yuan Jiang

Max-Planck-Institut für Kolloid- und Grenzflächenforschung Potsdam

Vorstufenphasen in Nichtklassischer Kristallisation

Das Hauptziel dieser Arbeit ist das Verständnis der molekularen Kristallisation, sowohl mit als auch ohne polymere Additive, als einen mehrstufigen Prozess. Dieser beinhaltet eine transiente flüssig-flüssig Phasentrennung, die Nukleation von Nanokristallen in der dichten flüssigen Precursor-Phase so wie eine anschließende nanokristalline Selbstorganisation.

Die Arbeit beginnt mit Untersuchungen an einem quaternären Modelsystem bestehend aus DL-Glutamat (Glu), Polyethylenimin (PEI), Wasser und Ethanol. Das Phasendiagramm dieses quaternären Systems wird durch Variation der Glu/PEI w/w und Wasser/EtOH v/v Verhältnisse bestimmt, wobei Präzpitat aus polymerinduzierten flüssigen Precursor, Koazervate oder homogene Mischungen erhalten werden Das thermodynamisch stabile Koazervat kann als Referenz für das Verständnis von flüssigen Precursorn angesehen werden, welche in der Natur metastabil und transient sind. Der mehrstufige Mechanismus der Glu-Präzipitation mit PEI als Additiv wird dann mittels Neutronen Kleinwinkelstreuung untersucht. Dies zeigt, dass die ursprünglich gebildeten flüssigen Precursor noch vor der Nukleation von Nanokristallen einen Wechsel von Wachstum und Koaleszenz durchlaufen. Die Ergebnisse aus optischer- und Eletronenmikroskopie zeigen, dass sowohl die flüssigen Precursor Superstrukturen ausbilden als auch, dass die Nukleation von Nanoplättchen in jedem einzelnen Precursor Tropfen von statten geht. Dies geschieht noch bevor sich die Nanoplättchen selbst in einer radialen Orientierung ausrichten. Diese Studie liefert die Kinetik der Präzipitation von organischen Stoffen in Gegenwart von polymeren Additiven.

Eine ähnliche Vorgehensweise wie für die Herstellung von Mikrokügelchen kann für die Darstellung von gemusterten Filmen angewandt werden. Die homogene Nukleation von Nanopartikeln (NPs) findet während der Verdampfung einer quarternären DL-Lys·HCl-Polyacrylsäure-Wasser-Ethanol Dispersion auf einer hydrophilen Oberfläche statt. Die darauffolgende vollständige Verdampfung löst die Mesokristallisation eines kontinuierlichen sphärolithischen dünnen Films aus, welcher sich wiederum in einen mesokristallinen dünnen Film umwandelt. Mesokristalline Filme mit 4 Hierarchiestufen bzw. auch periodische Filme werden durch die Verdampfung der Mikrokügelchen-Dispersion erhalten. Die Ergebnisse zeigen, dass die Verdampfung eine einfache aber effektive Methode zur Herstellung von verschieden gemusterten hierarchischen Filmen darstellt.

Nicht-klassische Kristallisation wird auch in der Abwesenheit von polymeren Additiven beobachtet. Wir verfolgen mittels Rasterkraftmikroskop (AFM) die Nukleation und das Wachstum einer neuen molekularen Schicht auf wachsenden DL-Glu·H2O Kristallen aus übersättigter Mutterlauge. Die Bildung einer neuen molekularen Schicht verläuft durch die Anlagerung von amorphen Nanopartikeln. Das Schrumpfen der NPs zusammen mit der strukturellen Änderung von dreidimensionalen NPs zu 2D Schichten wird während dieses Relaxationsprozesses beobachtet. Schließlich kommt es zu der Ausbildung einer neuen molekularen Schicht. Die Bildung einer molekularen Schicht durch die Anlagerung von Nanopartikeln aus der Lösung und die darauffolgende Relaxation liefert ein abweichendes Bild zu der bisher gängigen klassischen Theorie des Kristallwachstums.

Table of Contents

1. Introduction

1.1. An Overview of Crystallization

Phase separation happens when a homogeneous system turns to be unstable after changing variables like temperature, pressure, chemical composition, *etc.* Liquid-solid phase separation and solid-solid phase separation are two typical phase separations in solution. Crystallization from solution is a typical liquid-solid phase separation process, where crystals are precipitated from a supersaturated mother liquor (Fig. 1.1A). Liquid-liquid (L-L) phase separation can also happen in multi-component systems, resulting in one phase rich in solute and an equilibrium phase (Fig. 1.1B). Both crystallization and L-L phase separation provide a basis for chemical separation and purification, because only few chemical reactions are complete and the components thereafter are always a mixture of the desired product, side product(s), reactant(s), solvent, and/or catalyst.

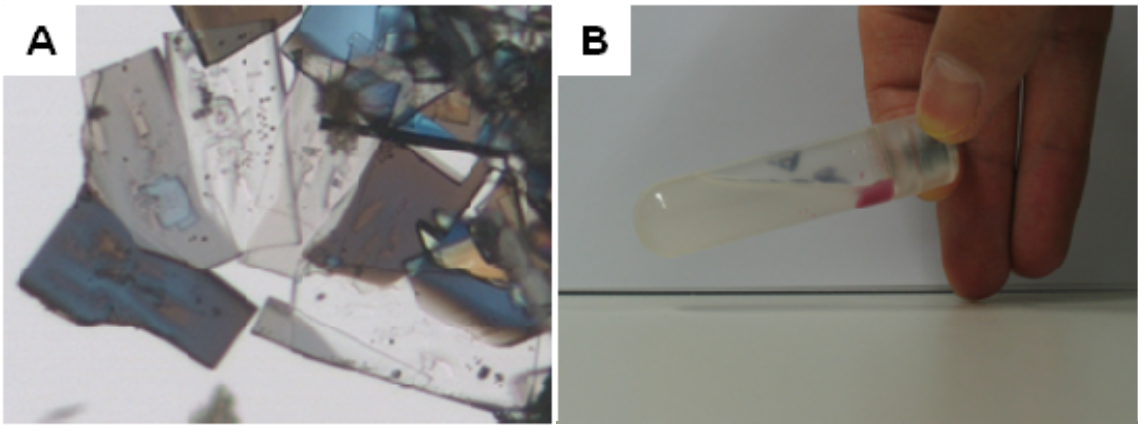

Fig. 1.1. Examples for phase separation. Image A: DL-Glutamic acid (Glu) crystals are formed in the mother liquor. Image B: an L-L phase separation in a quaternary Glu–polyethyleneimine (PEI)–water–EtOH system, where the condensed phase rich in solute is stained red for a better contrast.

Classical Understanding of Nucleation

To develop a generalized understanding of phase separation phenomena in various systems, physicists started to investigate phase separation in simple systems, usually omitting the differences in chemical structure. The classical nucleation theory (CNT) was

initially developed to describe the formation of vapor bubbles within a liquid matrix as a two-step process, namely nucleation and growth.[1] Then, it was extended to explain nucleation in crystallization systems, omitting the differences between an isotropic liquid and anisotropic crystal. Nuclei are the newly-formed phase in the supersaturated mother liquor. They lower their system free energy by a counter-play between investment of surface free energy and gain of bulk energy upon particle formation and growth. Nuclei surpassing a critical size continue to grow into bulk crystals; whilst those smaller than this size re-dissolve (Fig. 1.2A).

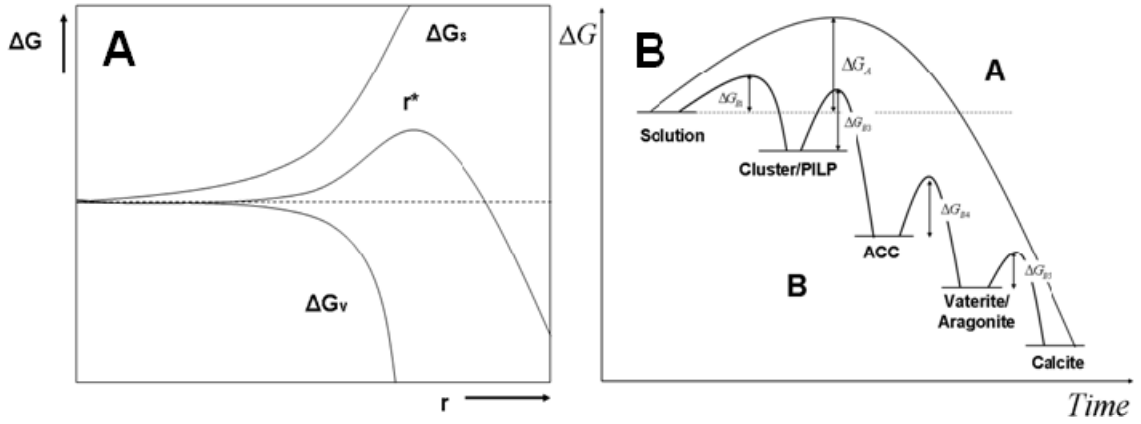

Fig. 1.2. Image **A**. Gibbs free energy (ΔG) plot for nucleation with the existence of critical droplet size r^*. Gibbs free energy contains two components: the energy gain for creating a new volume (ΔG_v) and the energy loss because of surface tension of the new interface (ΔG_s). Image **B**. The diagram shows how the activation energy (ΔG_A) is decreased according to Ostwald's rule of stages in a $CaCO_3$ crystallization system (route B), compared to CNT route (route A).

An impractical hypothesis in CNT is that nuclei show the same crystalline structure as the finally formed crystals. This hypothesis is challenged by the Ostwald's rule of stages, which states that the initially formed new phase is not the thermodynamically stable crystalline one, but an intermediate phase having the closest free energy to the initial one (Fig. 1.2B).[2] The Ostwald's rule of stages reveals the possibility that crystallization is a multi-step process, passing through a series of polymorphs as well as possible precursors. Indeed, some examples have been found that support the Ostwald rule of stages, which will be discussed in the following paragraphs. However, whether or

not this rule generally holds is still unknown because transient nucleation in molecular crystallizations happens in a small size range typically between 1 and 100 nm.

Understanding Nucleation on Colloidal Systems

A direct real-time observation of homogeneous nucleation on the micro- and nano-scale is still impossible. Simulation and theoretical routes provide the possibilities to predict the nucleation microscopically. Simulations by ten Wolde and Frenkel pioneered a two-step nucleation by proving the existence of a second phase separation in homogeneous nucleation: the nucleation of a protein-rich liquid phase followed by the nucleation of proteins within this phase.[3] Therefore, the nucleation barrier is much lowered, because the density difference between the protein-rich phase and protein crystal is smaller than that between the protein solution and the protein crystal. There is no length scale given in the simulation work. Experimentally, Galkin and Vekilov observed that the rate of nucleation went through a maximum during the cooling of a lysozyme solution in the vicinity of the metastable L-L phase separation boundary.[4] This experimental observation is contradictory to the monotonic increase of the nucleation rate with the increase of supersaturation, and it can be attributed to the formation of a protein-rich phase, which lowers the barrier of protein nucleation. The metastable liquid phase is also observable with optical microscopy.[5]

Most recently, De Yoreo and co-workers provided a microscopic observation of the nucleation of an S-layer protein by using in-situ atomic force microscopy.[6] After the attachments of amorphous- or liquid-like protein aggregates, their transformation into crystalline nuclei is convincingly shown for the first time. The conformational changes in protein aggregates are responsible for the multi-step structural transformations, whilst the possible template effect from the used lipid substrate, however, cannot be excluded. Protein crystallization systems are advantageous for the understanding of nucleation mechanisms on the molecular level as they are charged molecules, anisotropic in morphology, and monodisperse in size distribution. On the other hand, proteins are nanometers in size and are flexible in conformation, both of which impede their crystallization and are their main differences from small molecules.

Colloidal suspensions such as latexes are also advantageous systems for understanding of nucleation mechanisms for two reasons. First, colloids micrometers in size which move slowly and are visible in optical microscopy can be prepared. Second, the surface properties of colloids, which control the interactions between colloids, can be modified by chemical reactions. Indeed, important questions such as the nucleation rate in colloidal systems have been determined experimentally[7] and theoretically,[8] resulting in satisfactory agreement.

Colloidal systems are able to provide time-resolved information of nuclei structures during the multi-step nucleation. Interestingly, simulations both for hard-sphere colloid suspensions[8] and for oppositely-charged colloids[9] predict that the initially formed clusters cannot be used as a template for the subsequent crystal growth, unless they transform to the same structure as the finally formed crystals. Although there are debates about the structural details of the initially formed clusters, the existence of structural transformations during the nucleation of colloidal suspensions from simulation work microscopically proves the partial correctness of the Ostwald's rule of stages. However, Ostwald provides a thermodynamic point of view, predicting that the subsequent phase has the smallest difference in free energy from the former one; whilst simulation shows that the subsequent phase is preferred to form because it has the smallest activation energy barrier to the former one, which is a kinetic point of view.[9]

Precise simulations have to be in agreement with experiments. However, there is no structural transformation according to the experimental observations. Gasser and Weitz followed the growth of nuclei in a hard-sphere colloidal suspension by using confocal microscopy.[10] Except for the non-spherical shape of nuclei, their results agree well with CNT, i.e. the critical nuclei show the same structure as the bulk crystalline phase. Colloidal systems have some drawbacks as a model system for understanding nucleation on the molecular scale. For example, colloids such as latexes are not absolutely monodisperse systems. In addition, it is difficult to design colloids into complex and anisotropic morphologies. Both reasons alongside with others can bring unexplainable interference in the predictions of the nucleation rate and mechanism in molecular systems.

Nucleation Proofs from Material Science

Biominerals and many artificial materials show particle-based structures instead of single crystalline ones from molecular attachment.[11, 12] For example, the skeletal elements of sea urchin are single crystalline in electron diffraction analysis, whilst they are characteristic for their curved morphology and porous patterned structure instead of being single crystals with a simple geometric form. Artificial $CaCO_3$, which is synthesized using an anionic polyelectrolyte as an additive, can also form single crystalline structures with crystallographically ordered nanoparticles (NPs) as building blocks.[13] In both cases, polymeric additives are applied, which can cause the deviation of crystallization from a classical route. However, $(NH_4)_3PW_{12}O_{40}$ can precipitate from its mother liquor without polymeric additive, and exist as porous structure with crystallographically ordered nanoparticles as building blocks.[14] The concept "non-classical crystallization" is used to explain particle-based crystallization routes.[12] Generally, non-classical crystallization can be divided into three steps in sequence: the formation of precursors, their structural transformation to crystalline building blocks, and the formation of final products, all of which will be discussed as follows.

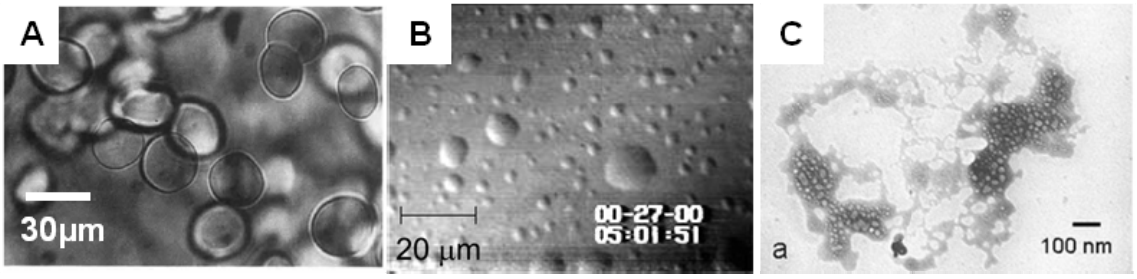

Fig. 1.2. Liquid precursors in Y_2O_3–Al_2O_3 by rapid quenching (**A**),[7] protein crystallization (**B**),[5] and $CaCO_3$ crystallization[15] systems (**C**). Images **A** and **B** are OM images, and **C** is a cryo-TEM image.

There are several kinds of precursors, including liquids, amorphous phases, clusters, nanoparticles (NPs), and metastable polymorphic structures.[16] Metastable liquid precursors are formed if the homogeneous system enters the metastable L-L phase separation zone (although "fluid" is a more precise description, "liquid" is used instead because of being used most frequently in the literature). It has been found in the formation of ceramics (Fig. 1.2A),[7] protein crystallization (Fig. 1.2B),[4] and $CaCO_3$

mineralization (Fig. 1.2C)[15] systems. In the ceramics and protein cases, the newly formed metastable liquid phases can grow to macroscale, as observed in optical microscopy. Although crystals are indeed observed in the precursors phases, there is still no sufficient information about the underlying mechanism. The length- and time-scale are suggested to be the main reasons because nucleation is a fast process and happens on the nano-scale. Indeed, an emulsion-like $CaCO_3$ phase is captured 100 ms after reaction by using cryo-transmission electron microscopy (cryo-TEM; Fig. 1.2C). Then it solidifies into an amorphous phase, which acts as embryo for the crystallization of one $CaCO_3$ polymorph–vaterite. The process follows the Ostwald rule of stages. The crystallization of $CaCO_3$ passing through a liquid precursor was also suggested for systems containing anionic polyelectrolytes such as polyaspartic acid[17] and polyacrylic acid (PAA).[15] Liquid precursors in crystallization with polymeric additives have to be distinguished from the non-crystallizing coacervates, which can be thermodynamically stable or deeply trapped in a metastable state.[18]

Clusters are another precursor, which have been suggested as a possibly existing phase for crystallization for a long time. They have been connected with the concentration gradient in supersaturated solutions from the 1960's, when Mullen and Leci found the existence of a concentration gradient in aqueous citric acid solution.[19] However, conclusive results for their existence are still missing. The rising question is whether clusters are prenucleation species or they are just transient structures during the nucleation.[20, 21] Analytical ultracentrifugation is a powerful tool to prove the existence of clusters in solution in supersaturated as well as unsaturated solutions, providing information about their size and mass fraction.[22] The underlying hypothesis in this work is that the local coordination structure of clusters is equal to that of a certain precursor or polymorph. Therefore, the size of clusters is getting smaller when the assumed particle density is getting higher, and *vice versa*. With cryo-TEM technique, Pouget *et al.* observed the existence of $CaCO_3$ clusters ~1 nm in size, supporting the existence of clusters during the nucleation of $CaCO_3$.[23] It is still difficult to distinguish their structure and their stability with this technique and others because of the small size of cluster. A different opinion from a simulation report predicted the existence of transient inhomogeneities in a supersaturated colloidal suspension, and suggested that nucleation

preferentially happens within the more structured zones by increasing the bond order. To summarize, there may be an increase of structural order from transient and loosely-ordered networks to the crystalline clusters during the nucleation from a supersaturated solution.

In addition to liquid precursors and clusters, amorphous phases and nanocrystals can be used as precursors in crystallization too. For example, an amorphous phase can be formed from either liquid precursors[15] or from cluster aggregation[22] in the crystallization of $CaCO_3$. In another case, crystalline Pt nanocrystals can grow by monomer attachment as well as by the coalescence of nanocrystals.[24] Therefore, the appearance of precursors and their properties depend heavily on the systems used, and their formation and transformation is usually still too fast to capture. We are still at the early stage in understanding nucleation.

Non-crystalline precursors disappear after the formation of nanocrystals, which can aggregate into superstructures (routes b, c, and d in Fig. 1.3) or grow to single crystalline structures (route a). Without the existence of polymeric additives, the crystalline NPs can grow up into single crystals by an Ostwald ripening process or by a solid-solid reaction. Biominerals and crystals prepared with polymeric additives can show superstructures with nanocrystals as building blocks. These are often so-called mesocrystals. The notation "Mesocrystal" is the abbreviation for mesoscopically structured crystals, which are aggregates of nanocrystals with mutual orientation (Fig. 1.3).[12] Mesocrystals can be stabilized as final products (route c) or recrystallize into single crystals (route b). In many cases, initially formed metastable NPs do not show a mutual crystallographic orientation because of the fast aggregation. Superstructures, (e.g. dendrites, spherulites, diffusion-limited aggregates, and randomly attached nanocrystals) are obtained from self-organization – a far from equilibrium process.[25] A special case in inorganic nanocrystal systems is that nanocrystals can merge into 1D single crystals in a head to tail manner, namely oriented attachment.[26] Oriented attachment can be treated as a special case in the formation of mesocrystalline materials.

For better understanding of the formation mechanism of a superstructure, it is necessary to understand the interactions between NPs during their aggregation. Colloidal, evaporation, and capillary forces, physical field forces, and confinement effects are

suggested to be responsible for the production of superstructures on the micro- and macro-scale. However, there are still no quantitative conclusions. On the one hand, many forces work during a far from equilibrium process. On the other hand, several forces always work co-ordinately. Therefore, people turn to biological systems to looking for the answer.

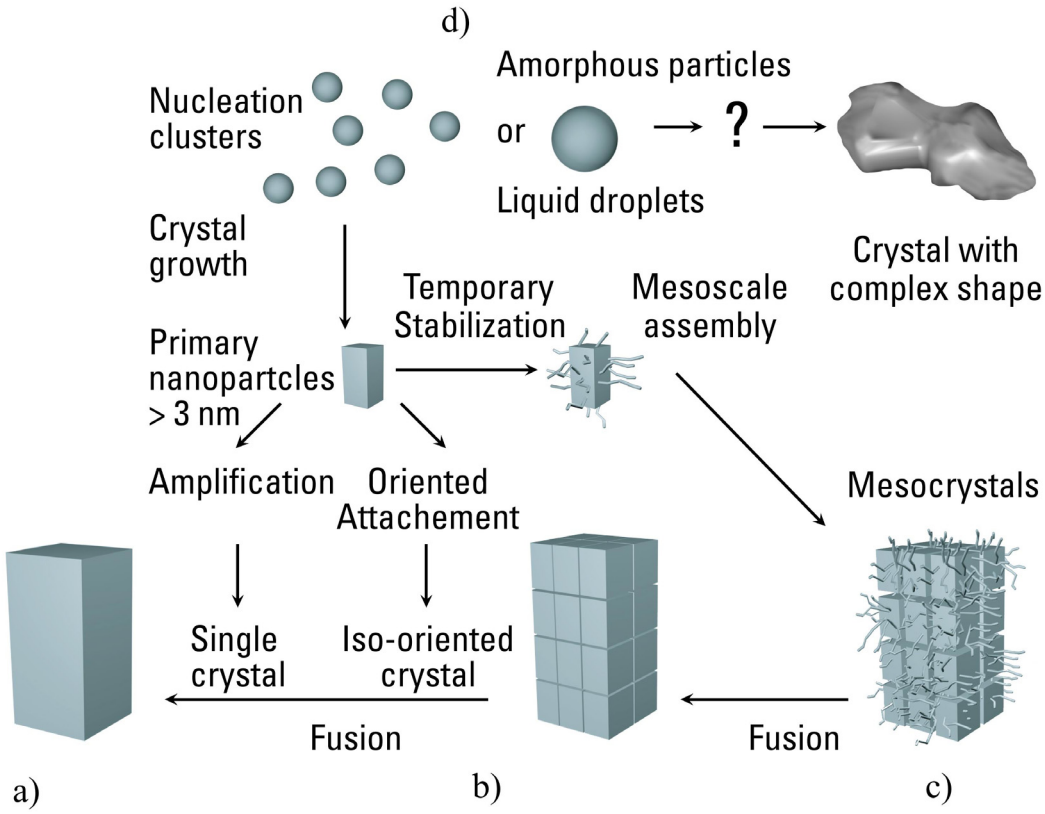

Fig. 1.3. The summary of non-classical crystallization.

Biominerals are formed by the collaboration of various forces. They are inorganic-biomacromolecular hybrid materials with hierarchical construction across nano-, micro-, and macro-scale.[27] The presence of biomacromolecules is essential for the formation and stabilization of structures on every length scale. In addition, crystallization kinetics has been influenced heavily by using soluble polymers as additives. Although there is still no precise understanding of their role, polymers are known to have multiple roles in the formation of complex structure with counter ions or molecules, stabilizing and shaping NPs, modifying nucleation kinetics, and adsorbing on certain crystal surface.[28] It is

necessary to clarify how these interesting polymeric additive polymers affect biomineralization and crystallization with polymer as additives.

On the Shoulders of Giants

Evidence shows that the detection of multi-step nucleation must be on the proper length- and time-scales. For example, nucleation in molecular systems must happen on the nanoscale. Therefore, techniques such as AFM, cryo-TEM, and small angle scattering are good for detecting the nucleation processes.

For each step in a multi-step nucleation process, the formation of a liquid precursor phase in solution is a fast process. Until now, it is still debated whether the liquid phase originates from a spinodal or binodal decomposition. The structural transformation between the amorphous- or liquid-like precursors to crystals is the rate-determining step, which can be observed by time-resolved techniques on the nanoscale such as AFM and small angle scattering. The final step – the growth of crystals is already a popular topic, which has been investigated both macroscopically and microscopically.

The direct visual detection of homogeneous nucleation in crystallization on the molecular level is still not possible. However, the detection of heterogeneous nucleation might be possible since its nucleation rate is lower than that in homogeneous nucleation and the decreasing free energy barrier can reduce the nucleation rate. The success in investigating the nucleation of proteins proved this supposition, which also indicates that the observation of 2D nucleation in molecular systems might be possible.

With these rules extracted from "the overview of crystallization", a series of experiments were designed in this study to understand molecular crystallization with or without polymeric additives as a multi-step process.

1.2 An Introduction to the Experimental Systems

The main objective of this thesis is to understand molecular crystallization as a three-step process with or without polymeric additives: the formation of non-crystalline precursors, their structural transformation into nanocrystals, and the self-assembly or self-organization of nanocrystal on the nano-, micro-, and macro-scales. The thesis also focuses on the detection of possible precursor phases in crystallization with or without

polymeric additive. In this context, the formation of hierarchical microspheres and patterned thin films extends our understanding of non-classical crystallization.

Instead of using inorganic mineralization systems, the precipitation of organics was chosen as a model system for several reasons. Compared to some inorganic mineralization systems, the precipitation of organics precludes the interference of chemical reactions. In addition, the lattice energy of organic molecules is always on the scale of tens of $kJ \cdot mol^{-1}$, compared to hundreds or even thousands of $kJ \cdot mol^{-1}$ for inorganic materials. Relatively low lattice energy results in slow crystallization kinetics, which makes the time-resolved research possible. Furthermore, organic molecules are advantageous for their large number of polymorphs and additional crystallization parameters such as chirality and dipole-dipole interactions. Practically, many functional organic molecules are water insoluble. Processing these molecules into colloidal dispersions, where they are stabilized as nano- or microcrystals in aqueous solution, is an important route to extend their applications to the pharmaceutical and painting industry.

Amino acids are zwitterions, containing amine group(s), carboxylic acid group(s) and other functional group(s) on their side chains. Functional groups on amino acids facilitate interactions with oppositely charged additives (e.g. polyelectrolytes) via electrostatic interactions, hydrogen bonding, and/or hydrophobic interactions. A four-component system to study a polymer-induced liquid precursor (PILP) system is presented in this thesis composed of amino acid, polyelectrolyte, water, and alcohol. The oppositely charged amino acid and the polyelectrolyte form complexes in aqueous solution. Then, EtOH, which is a non-solvent to amino acid, is mixed with the above aqueous solution. Consequently, precipitation from a metastable PILP phase or coacervation happens, which depends on the mass ratio of amino acid and polyelectrolyte.

1.3 Thesis Outline

Chapter two briefly introduces fundamental concepts of phase separation and crystallization. Then, important instruments used, including microscopy and small angle neutron scattering, are presented in chapter three. Results from this thesis are presented from chapter four to chapter seven. The eighth chapter provides the summary & opportunities of this thesis. Experiments and abbreviations are put in the Appendixes.

In chapter four, the phase diagram of a quaternary Glu–PEI–water–EtOH system is thoroughly investigated, where Glu/PEI (w/w) is the main variable for obtaining coacervates or precipitates from PILPs. In addition, the composition of coacervates is measured by nuclear magnetic resonance (NMR). The structural details of Glu-PEI complexes in aqueous solution are also characterized for the understanding of interactions between Glu and PEI.

The next chapter focuses on the mechanism of precipitation of Glu with PEI as an additive. The first section is mainly designed to detect the kinetics of Glu precipitation from a metastable PILP phase combining small angle scattering and stopped flow technique. The self-organization of nanostructures, which are nucleated from PILP phases, is presented in the second section. This section also focuses on the influence of various parameters such as the pH value, Glu/PEI (w/w), temperature, *etc.* onto the Glu morphogenesis process. The PILP route can be extended to other precipitation systems of amino acids with oppositely-charged polyelectrolytes as additives.

Chapter six switches to the DL-Lys·HCl (Lys)–polyacrylic acid (PAA)–water–EtOH system. Mesocrystalline thin films are prepared directly from metastable PILP dispersions, and the essential three steps are the evaporation of solvent, the formation of a continuous spherulitic thin film, and recrystallization from spherulitic to mesocrystalline thin film. Quenching is helpful for optimizing the processing of mesocrystalline thin film. In the other two cases, hierarchical thin films with at least four hierarchy levels as well as patterned structure by self-organization are introduced, starting from the redissolution and recrystallization of a microsphere dispersion.

In chapter seven, two-dimensional (2D) nucleation and growth of a DL-Glu·H_2O molecular layer is observed by using in-situ atomic force microscopy (AFM). The structural transformation from amorphous NPs to crystalline molecular layers is described and the critical size of NPs in nucleation is estimated. Our results show that the nucleation of a molecular layer can involve NP attachment and restructuring rather than molecular addition.

2. Theory and Background

2.1 Nucleation and Crystallization

Nucleation is a kind of first-order phase separation. It happens when the free energy of the coexistence of two phases is lower than that of the old homogeneous phase. Nucleation occurs only when the system surpasses a free energy barrier.

The classical nucleation theory (CNT) stems from the work of Gibbs,[29] Volmer,[1] Becker and Döring,[30] and was initially used to describe vapor bubble formation within a liquid phase. In this regard, nucleation can be divided into homogeneous and heterogeneous cases. Homogeneous nucleation occurs within a uniform phase, whilst heterogeneous one proceeds at the boundary or on an impure surface. Although homogeneous nucleation consumes more energy than heterogeneous one, it is relatively easy to solve mathematically as nuclei are assumed to be of spherical morphology: a result of surface energy minimization forces.

CNT supposes the existence of nuclei in the supersaturated solution phase, such that the growth or shrinkage of nuclei in homogeneous nucleation is determined by the Gibbs free energy ΔG. ΔG contains two components: the energy gain for creating a new volume (ΔG_v) and the energy loss because of the increasing surface tension of a new interface (ΔG_s). Therefore ΔG can be defined by the following equation:

$$\Delta G \equiv \Delta G_v + \Delta G_s = \frac{4}{3}\pi r^3 G_v + 4\pi r^2 \sigma$$

where G_v is the change of free energy per unit volume, r is the radius of the nuclei, and σ means the interfacial tension. The volume term is always negative in value, whilst creating surfaces always consumes energy. The value of ΔG_v changes with r^3, whilst ΔG_s changes with r^2. Thus ΔG is always negative at large values of r. However, the volume term and the surface term can stay at the same level in a small range of r. The relationship between r and ΔG is shown in Fig. 1.2A. In the case $r < r^*$, where r^* is the critical nucleus size, energy is required to add molecules to the nuclei, which causes the disappearance of nuclei simultaneously. If $r > r^*$, adding molecules to the nuclei is a

spontaneous process and they will continue to grow until a thermodynamic equilibrium is obtained. The value of the nucleation barrier ΔG^* can thus be obtained by solving the equation $d\Delta G / dr = 0$:

$$\Delta G^* = \frac{16\pi\sigma^3}{3G_v^{\ 2}}$$

Thus, the nucleation rate J is given by:

$$J = A\exp\left(\frac{-\Delta G^*}{k_B T}\right)$$

where A is a prefactor and is dependant on many parameters. From the above equation, the nucleation probability depends on the exponential of the barrier height divided by $k_B T$. CNT suppose that nuclei show the same crystalline structure as the bulk crystals. Therefore, σ is constant. Consequently, the only way to lower the energy barrier is to increase the supersaturation, which results in the increase of G_v.

Compared to homogeneous nucleation, both the energy barrier and volume of nuclei in heterogeneous nucleation are lowered because the wetting behavior of nuclei on a surface lowers the surface tension of the nuclei. The Gibbs energy for heterogeneous nucleation ΔG_{hetero} on a flat surface is written as:

$$\Delta G_{hetero} = \Delta G_{\mathrm{hom}o} f(\theta)$$

The wetting factor $f(\theta)$ can be written as:

$$f(\theta) = \frac{1}{2} + \frac{3}{4}\cos\theta - \frac{1}{4}\cos^3\theta$$

where θ is the contact angle and the value of $f(\theta)$ is between 0 and 1. The critical radius r^* during heterogeneous nucleation is unchanged from that in homogeneous nucleation. The above equation explains heterogeneous nucleation on an infinite flat surface. The expression of $f(\theta)$ can be written into various expressions according to the topography of the phase boundary.[31]

In spite of its apparent simplicity, CNT is based on several impractical assumptions, limiting its applications to predict the kinetics of crystallization in solution. For example, CNT supposes that nuclei show the same crystalline structure as the bulk crystal. This straightforward route has been challenged by many experimental proofs such as the

existence of 'polymorphs' and 'precursors'. The Ostwald's rule of stages fills the gap and considers crystallization as a sequential process, involving not only an increase in particle size but also structural and compositional transformations. This rule indicates that crystallization starts from the least stable form, passing through metastable polymorphs, and terminating at the thermodynamically most stable polymorph, where the stability sequence can be conveniently determined by the decrease of solubility.[32] The crystallization of $CaCO_3$ is used as an example to show how this rule works (Fig. 1.2B). Unlike route A, which have a high free energy barrier to proceed the nucleation, the sequential route B passes from the supersaturated solution to different precursor phases and polymorphs in sequence before the formation of the most stable polymorph of $CaCO_3$ – calcite. Therefore, the Ostwald's rule of stages considers the sequential process from a thermodynamic point of view.

Crystallization, however, is a kinetically controlled process. Therefore, the sequence of stages can also determined by the energy barrier between the newly formed phase and the old one. Experimentally, it is still difficult to verify whether the Ostwald's rule of stages passes through all possible precursors and polymorphs or not, because precursors and some polymorphs are transient and metastable in nature.

An advantage of the Ostwald's sequential route is that each step needs only a relatively low energy barrier. Such decreases in the energy barrier occurs by decreasing the interfacial tension σ. For example, the difference in σ between the solution and liquid-like nuclei is smaller than that between the solution and crystalline nuclei. Therefore, the Ostwald's rule of stages provide an effective way to lower the energy barrier by the decease of σ, which is supposed to be a constant in CNT.

Another series of CNT assumptions originate from the misconnection between micro- and macroscale properties. CNT neglects the possibility of size-based surface tension (i.e. the capillary approximation). Because nuclei contain hundreds of molecules, it is improper to neglect their interactions with surrounding molecules. In the 1980's, Oxtoby *et al.* began to tackle the capillary approximation problem in CNT by using density functional theory (DFT).[33] Instead of using the droplet size as a function of free energy, DFT uses a density profile across the interface between droplets and the bulk phase. Notably, DFT predicts that there is no energy barrier at the spinodal curve (the

concept of "spinodal" will be introduced in section 2.3) in the supercooled vapor or bubble formation, which represents an important improvement upon original CNT.

CNT also fails to consider the nuclei-nuclei interactions, which can create nuclei surpassing the critical size. This approach was put forward by Smoluchowski[34] and has been widely applied in explaining the aggregation of particles later on. The Smoluchowski equation describes the rates of nuclei formation and disappearance:

$$\frac{dn_k}{dt} = \frac{1}{2}\sum_{i+j=k} K(i,j) n_i n_j - n_k \sum_{i=1}^{\infty} K(i,k) n_i$$

where the K terms are reaction rate coefficients and contain complex mathematical expressions to include nuclei fragmentation, rearrangement, *etc.* The first term represents the rate of creating new nuclei of a certain size from small ones. The second term shows the disappearance of such nuclei by their reactions with other nuclei.

CNT supposes that the nuclei larger than the critical size can grow irreversibly into bulk crystals. However, it is a common phenomenon that large crystals grow preferentially at the cost of sacrificial small ones, which is named as the Ostwald ripening process.[35] The process is spontaneous since larger particles always have lower surface energy compared to small ones. The influence of particle radius r on the particle solubility c_r is described as:

$$c_r = c_0 \exp(\gamma \upsilon / rRT)$$

where c_0 is the solubility of a crystal with an infinite flat surface, γ is the surface tension, υ is the volume of one molecule. Experimentally, small crystals are kinetically preferred in the formation of particles. The number of particles then decreases whilst the existent particles increase in size by an Ostwald ripening process. The Ostwald ripening also contains the transformations between precursors and polymorphs.

Precipitation is a spontaneous and rapid crystallization process, typically generating crystals small in size and narrow in size distribution.[36] Crystals smaller in diameter than 10 μm are called precipitates. One popular way to prepare precipitates is to prepare a supersaturated solution of the solute, and mix it with a non-solvent (also named as drowning-out or reprecipitation). From a practical point of view, the processing of

precipitates can find many applications in the pharmacy and paint industries, as a large amount of small crystalline materials (e.g. less than several micrometers) are needed.

In this regard, the LaMer curve describes how to obtain precipitates small in size with narrow size distribution (Fig. 2.1.1).[37] It divides the solubility change of solutes during crystallization into three steps. The prenucleation step sees the rapid increase of concentration. During this period, nucleation does not happen even if the concentration is higher than the saturated concentration C_s. Then, nucleation immediately occurs when the concentration passes over the threshold value C_s^x and it finishes when the concentration decreases to C_s^x. Crystals grow until the concentration decreases to C_s. According to the LaMer curve, precipitates narrow in size distribution are only accessible when the nucleation period is narrow. The reason is straightforward: simultaneous nucleation produces nuclei similar in size and Ostwald ripening is highly prohibited. However, it is impossible to prepare precipitates absolutely monodisperse in their size distribution, resulting in the secondary nucleation, aggregation or reprecipitation. Therefore, additives or confined space is needed to stabilize precipitates from Ostwald ripening.

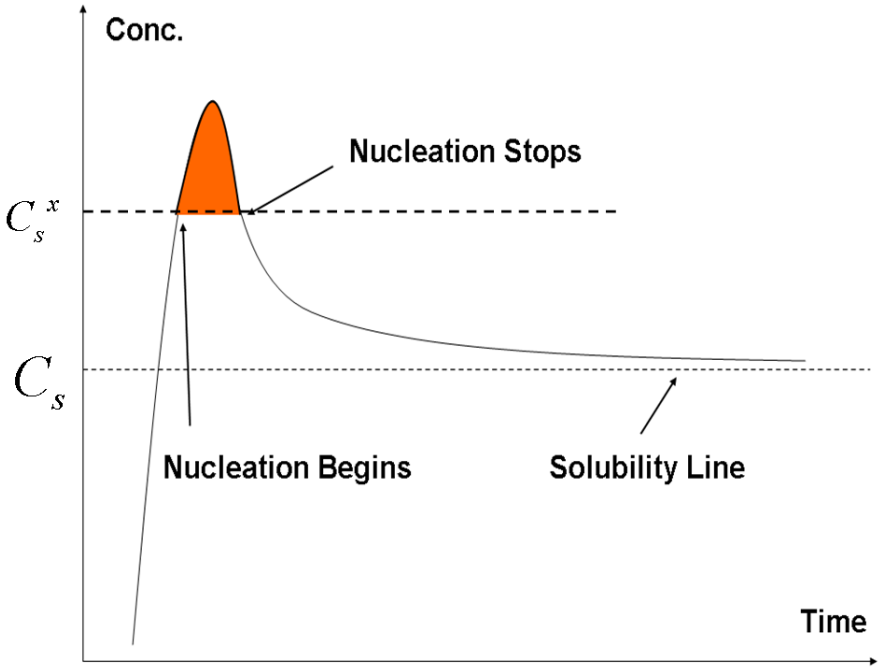

Fig. 2.1.1. The schematic LaMer mechanism, showing the nucleation and growth process with time. The brown zone is the nucleation period when the concentration is higher than the threshold value C_s^x. After nucleation, concentration goes back to the solubility line C_s.

2.2 Particle-Particle Interactions

As mentioned in the "Introduction" chapter, crystals can grow by molecular attachments as well as nanocrystals self-assembly and self-organization. Therefore, it is necessary to understand the forces, which are responsible for the interactions between the colloidal nanocrystals. The forces between colloids will be discussed herein.

Table 2.1 Electrostatic interactions

	Equation	Energy (vacuum; $kJ \cdot mol^{-1}$)	Range (nm)
Columbic	$\infty \frac{q_1 q_2}{r}$	100-1000	100
Dipole-ion	$\infty \frac{q_1 m_2}{r^2}$	30-400	0.5
Dipole-dipole	$\infty \frac{m_1 m_2}{r^3}$	< ~200	0.4
Hydrogen Bond	/	10-40	0.2

Colloids can be stabilized by electrostatic interactions as well as steric ones. Here a realistic supposition is that all colloids carry the same charges. Therefore, electrostatic interactions between colloids are repulsive. There is no precise expression for electrostatic interactions, which contains many items from direct interactions as well as induced ones. Table 2.1 summarizes the most important electrostatic interactions. The columbic interactions are long-range ones, whilst others vanish quickly after particles are taken apart.

As to steric interactions, they are repulsive in nature and are provided by the organic molecules adsorbed on the surface of colloids. Therefore, the organic layer must be of sufficient thickness and density to overcome attractive interactions between colloids. Steric interactions are short-range interactions and are effective only when the colloids approach each other at a distance less than twice the thickness of an adsorbing layer.

The attractions between colloids are mainly provided by van der Waals interactions. As the fall off with distance is given by r^{-6}, the distance between colloids is crucial in determining the strength of van der Waals interactions. Van der Waals interactions are as weak as several kT at R.T. and are difficult to calculate precisely in complex systems.

The combination of attractive and repulsive interactions can lead to the stability of colloidal systems. Fig. 2.2.1 shows how interaction potentials change with the distance between colloids. First, there is an appearance of a secondary minimum, where colloids are kinetically stabilized. To obtain thermodynamically stable aggregates, colloids have to surpass a barrier between the primary and secondary minimum. The kinetically stable colloidal systems have the energy barrier far exceeds kT, therefore, the primary minimum becomes inaccessible. If the barrier is on the order of several kT, a rapid and irreversible aggregation can occur, obtaining stable aggregates.

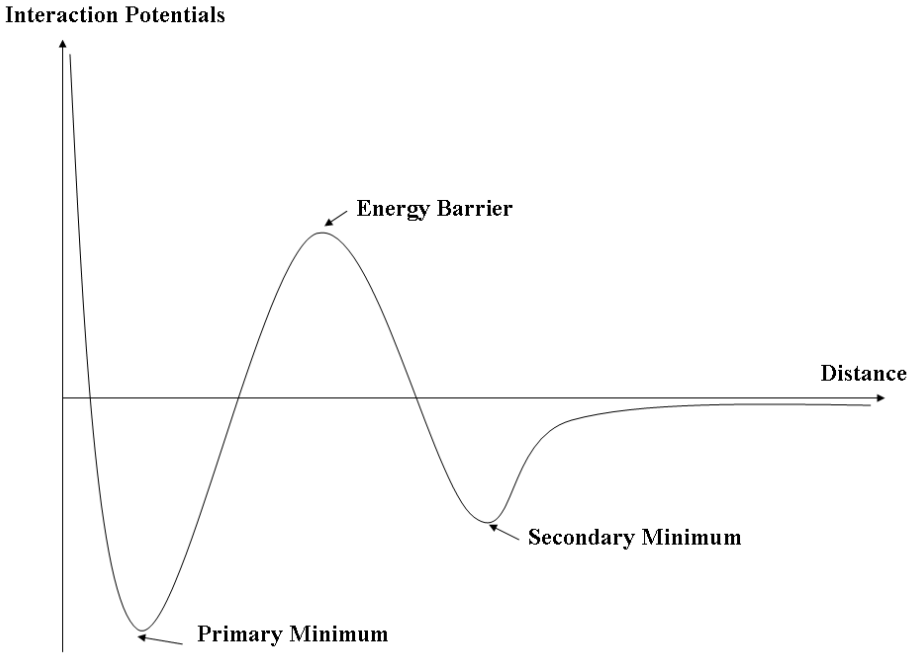

Fig. 2.2.1. The relationships between interacting potentials and the distance in colloidal systems.

The outcomes of a colloidal aggregation also depend on the processing after the initial association. Although rearrangement can sometimes happens between particles, the aggregation in colloidal systems is an irreversible process in most cases, resulting in aggregates with their initially trapped configuration. Therefore, colloidal aggregates can show the densely-packed style in an equilibrium state as well as fractal properties from a non-equilibrium process. The relationship between the mass of densely-packed aggregates and the distance can be written as

$$W(r) \propto r^3$$

whilst the relationships between the mass of fractal structures and the distance is as follows

$$W(r) \infty r^{d_f}$$

where d_f is a number between 0 and 3. Two representative topologies are from reaction-limited (d_f = 1.8) and diffusion-limited (d_f = 2.1) aggregations.[38] The formation of the first one is determined by the probability of particle attachments, whilst the rate of diffusing particles onto the growing aggregates determines the rate of diffusion-limited aggregation.

2.3 Phase Separation and the Critical Point

CNT only focuses on nucleation, which is a rare, but intense event. In his doctoral thesis, van der Waals recognized that a liquid beyond its liquid/gas critical point has a negative compressibility and is unstable to continuous changes. He named this phenomenon "spinodal". However, it was not until the 1950's that Cahn and Hilliard published a series of papers, which established them as the creators of the modern spinodal decomposition (SD) theory.[39-41] This classical work also reconciled SD to nucleation in phase separation. Unlike nucleation, SD is occurring over the whole solution phase in a cooperative fashion. Therefore, SD has no energy barrier and happens uniformly throughout the material. In this context, Binder successfully expanded SD theory to polymer and alloy science and connected theories to experimental fields.[42]

With regard to the thermodynamics of phase separation in a symmetric binary system, a pair of partially miscible liquids does not mix in all proportions over the whole temperature range. Thus mixing or demixing is determined by the systematic free energy. The free energy of mixing component A and B ΔG^{mix} has the following form:

$$\Delta G^{mix} = \Delta H^{mix} - T\Delta S^{mix}$$

where $\Delta H^{mix} = X_A X_B \beta$, $\Delta S^{mix} = -R\left(X_A \ln^{X_A} + X_B \ln^{X_B}\right)$ and X means the molar fraction of a component. The interaction term β is defined as follows:

$$\beta = k\left(2\omega_{AB} - \omega_{AA} - \omega_{BB}\right)$$

where ω_{AB}, ω_{AA} and ω_{BB} are the A-B, A-A, and B-B interactions, respectively. Therefore, ΔG^{mix} can be rewritten as:

$$\Delta G^{mix} = X_A X_B \beta + RT\left(X_A \ln^{X_A} + X_B \ln^{X_B}\right)$$

The entropic term is therefore always positive whilst the value of the enthalpic term depends on the value of β, which is temperature dependent. In the case $\beta < 0$, components A and B are miscible in any composition and at ambient temperature. If $\beta > 0$, it is possible that A and B demix when the temperature is lower than the critical value T^* (Fig. 2.3.1A). If $T > T^*$, only one peak appears in the red curve and two components are miscible in all compositions. Supposing $T < T^*$, the purple curve shows the saddle morphology and the demixing happens in some certain proportions. In the case $T \approx T^*$, the value of ΔG^{mix} is nearly constant over a wide range of X_B close to the value $X_B = 0.5$.

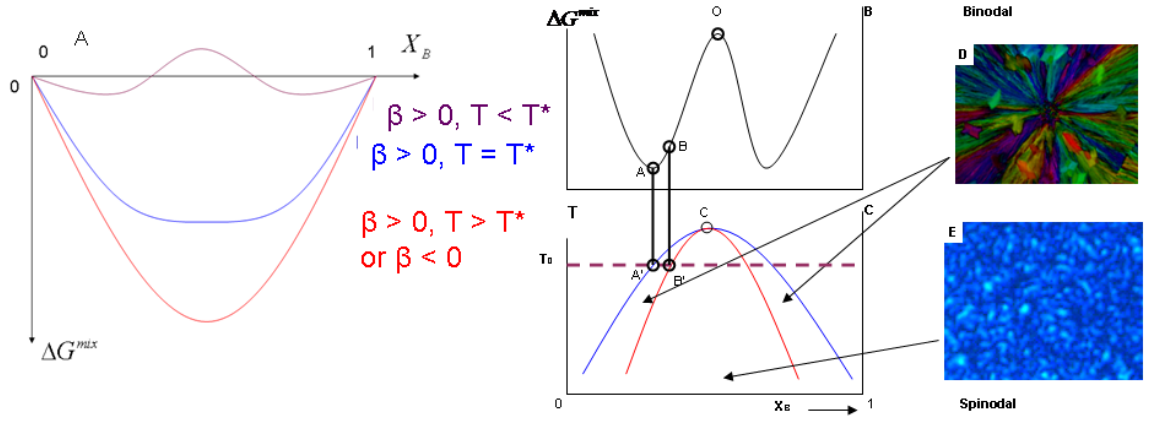

Fig. 2.3.1. Image A shows the relationships between the Gibbs energy of mixing ΔG^{mix} and composition X_B in a binary system at various temperatures and values of β. Image B shows the relationship between ΔG^{mix} and X_B. Image C represents the relationship between T and X_B, in which the red and blue curves are the spinodal and binodal lines, respectively. Images D and E describe binodal and spinodal decompositions, respectively.

In the next step, we consider the condition the situation $T < T^*$ and $\beta > 0$ .The relationship between ΔG^{mix} and X_B is considered in Fig. 2.3.1B, where the temperature is constant at T_0 . Points A and B satisfy $\partial \Delta G / \partial X_B = 0$ and $\partial^2 \Delta G / \partial X_B{}^2 = 0$, respectively. Mathematically, the A-B curve is characterized as $\partial^2 \Delta G / \partial X_B{}^2 < 0$ and the

B-O curve has the relationship $\partial^2 \Delta G / \partial X_B{}^2 > 0$. In Fig. 2.3.1C, the blue curve satisfies $\partial \Delta G / \partial X_B = 0$, which is named as the binodal line. The red curve obeys $\partial^2 \Delta G / \partial X_B{}^2 = 0$, namely the spinodal line. The area wrapped by the spinodal line is the unstable region (spinodal zone), satisfying $\partial^2 \Delta G / \partial X_B{}^2 < 0$, whilst the area between the spinodal line and the binodal line is the metastable region (binodal zone), where $\partial^2 \Delta G / \partial X_B{}^2 > 0$. The two curves meet at a critical point **c**, which can be calculated from the equation $\partial^3 \Delta G / \partial X_B{}^3 = 0$.

Understanding the phase diagram is the key to clarify the mechanism of phase separation. SD happens within the spinodal zone and nucleation and growth proceeds within the binodal zone. When the composition is near to the critical value $X_B{}^*$, decreasing the temperature slightly below the critical temperature T^* can easily bring the system into the spinodal zone. If the composition is far away from $X_B{}^*$, SD can only happen by quenching the system to the spinodal zone; otherwise, only nucleation and growth proceeds (Fig. 2.3.1C). Two representative pictures for binodal decomposition and SD are shown in Fig. 2.3.1D and E, respectively.

The dynamics of phase separation in a binary system can be described by a time-dependent Ginzburg-Landau theory:

$$\frac{\partial \sigma\phi_A(a,t)}{\partial t} = \Lambda * \nabla^2 \mu(a,t) + \xi(a,t) + HD$$

where $\sigma\phi_A(a,t)$ is the local concentration fluctuation at position a and time t, Λ is the Onsager kinetic coefficient, μ is the local chemical potential, ξ is the random thermal term, and HD is the long-range hydrodynamic interaction. Normally, HD term is omitted when $\sigma\phi_A(a,t)$ is small. Therefore, the above equation can be solved and rewritten into:

$$S(q,t) = S(q,\infty) + [S(q,0) - S(q,\infty)]\exp[2R(q)t]$$

where $S(q,t)$ is defined as $< \left|\sigma\phi_A(r,t)\right|^2 >$ and $S(q,0)$ is the initial $S(q,t)$. $S(q,\infty)$ is the virtual structure factor, which can be estimated by extrapolating the curve $S(q,t)$. The scattering vector q obeys

$$q = (4\pi \sin\theta)/\lambda$$

where 2θ is the angle between the incident light and the detector measuring the scattered intensity, and λ is the wavelength of the incident light. $R(q)$ is the growth rate for $\sigma\phi_A(r,t)$ and is expressed as:

$$R(q) = Dq^2\left[1 - \frac{q^2}{2q_m{}^2(0)}\right]$$

where $D = \Lambda\tau$ and $q_m{}^2(0) = \tau/2K$ (τ is the relaxation time and K is a positive constant).

Cahn derived the linear theory without considering the ξ term in the Ginzburg-Landau equation.[39, 40] Thus, the equation for $S(q,t)$ is simplified as:

$$S(q,t) = S(q,0)\exp[2R(q)t]$$

This equation is practically used for explaining early stage SD. However, the above theory fails in considering nonlinear effects, which are important in explaining intermediate and later SD processes. Many researchers have since proposed various extensions to the original theory, such as Cook theory[43] and Langer-Baron-Miller theory[44], with the primary intention of explaining the nonlinearity existence in early stage SD.

2.4 Thin Film Theory

Unlike crystallization from solution, the formation of thin film is explained by grain theory. In this section, current theories relating to grain growth are introduced. Metals, alloys, ceramics and biominerals are composed of polycrystalline grains. The size of each grain varies from the submicrometer to the macroscopic scale. The size and orientation of grains influences the physical properties of polycrystalline materials. Unlike dissolution and molecular diffusion within a diluted solution phase, which can be explained by CNT, grain growth occurs by the movement of grain boundaries within the condensed matrix phase. Parameters such as molecular diffusion rate, stresses at the phase boundary, and heterogeneous nucleation decide the growth rate of grains.

With regard to the nucleation of grains, nuclei are formed via a growth into spherical islands where surface tensions are isotropic. At equilibrium, this relationship stands as:

$$\gamma_{sg} = \gamma_{sl} + \gamma_{lg} \cos\theta$$

where γ_{sg}, γ_{sl} and γ_{gl} are the surface tensions between solid and gas phase, solid and liquid phase, and liquid and gas phase, respectively. θ is the contact angle of a nucleating phase (assuming nuclei are liquid-like) on the solid surface.

In the next step, molecules have to transport across the boundary to enter the nucleating phase. Generally, the rate of nucleation G can be written as:

$$G = G_0 \exp(-\frac{\tau}{t})$$

where G_0 is the steady-state rate of nucleation and τ is the induction time. τ can be written into various equations and is a parameter of interfacial energy, molecular density of particles, initial concentration, diffusion coefficient of solute, and the free energy change per unit volume of nucleating phase change.

When the grain size is sufficiently large, crystallography has to be considered to minimize the surface and interfacial energies. In this regard, nucleation prefers those routes that minimize the free energy of a thin film, whilst the free energy depends on the nature of the material, the grain size, and the anisotropy of the substrate. Importantly, grain orientation is unnecessary to be that of bulk materials and it is changeable during the nucleation and growth process.

A simplified model starts from two neighboring grains with radii r_1 and r_2 ($r_1 > r_2$) respectively. The driving force $\Delta\mu$ for the growth of grain **1** and the shrinkage of grain **2** per molecular volume v is as follows:

$$\frac{\Delta\mu}{v} = 2\gamma\left(\frac{1}{r_1} - \frac{1}{r_2}\right)$$

The velocity of boundary motion u_B is proportional to the driving force $\Delta\mu$ times the mobility of grain boundary M :

$$u_B = 2\gamma v M\left(\frac{1}{r_2} - \frac{1}{r_1}\right)$$

Practically, there are many grains with a wide size distribution within polycrystalline materials. An ideal method should include the size and number distribution of grains

surrounding a certain one. Experimentally, the rate of grain growth u follows an empirical law

$$u(t)^m - u(0)^m = \alpha t$$

where α is a constant for describing grain growth and the index number m is generally expected to be a value of 2.

Hillert applied coarsening theory to grain growth in both 2D and 3D systems.[45] He argued that growth rate of an individual grain is given by

$$\frac{du}{dt} \approx M\gamma_b(\frac{1}{r^*} - \frac{1}{r})$$

where r^* is the critical radius of grain. The value of r^* is equal to the average radius $\bar{r}$ and $\frac{9}{8}\bar{r}$ for 2D and 3D systems, respectively. γ_b is the average grain boundary energy per unit area of the grain boundary. Importantly, this equation states that grains larger than r^* will grow whilst those smaller than r^* will shrink and disappear finally.

To precisely understand the grain growth in thin film systems, two situations must be considered. First of all, real thin films are not 2D systems; in addition, thin films have surface factors, which depend on the orientation of grains. A theory of grain growth in thin films incorporates the anisotropic factor of surface energy by combining the macroscopically energetic arguments with coarsening theory:

$$\frac{du_s}{dt} = M\left[\frac{2(\bar{\gamma}_s - \gamma_s)}{h} + \bar{\gamma}\left(\frac{1}{\bar{r}} - \frac{1}{r}\right)\right]$$

where u_s is the rate of grain growth, $\bar{r}$ is the average grain radius, h is the thickness of the thin film, $\bar{\gamma}$ is the average grain boundary energy, γ_s is the surface tension of the grain being considered and $\bar{\gamma}_s$ is an average surface tension as a function of grain orientation distribution, relative to the orientation of the substrate.[46, 47] In short, the rate of grain growth u_s within thin films from the above equation contains not only the size effect from the size distribution of grains but the surface tension compared to the average surface tension of a thin film.

3. Methods of Characterization

3.1 Microscopy Techniques

3.1.1 Optical Microscopy

Optical microscopy (OM) can magnify samples small in size by using uses a series of lenses with light as a source. It is an inexpensive microscopy technique and instrumentation is not complex, as compared to electron microscopy or force microscopy. There are many kinds of OM techniques, including phase contrast microscopy, polarized optical microscopy (POM), fluorescence microscopy, stereo microscopy, and reflected light illumination, which can satisfy various research requests. In addition, the combination with charge-coupled device cameras and a convenient data reading on the computer screen simplifies the data collection process. Therefore, modern microscopy techniques can find extensive applications in materials, pharmaceutical, and medical science as well as biotechnology.

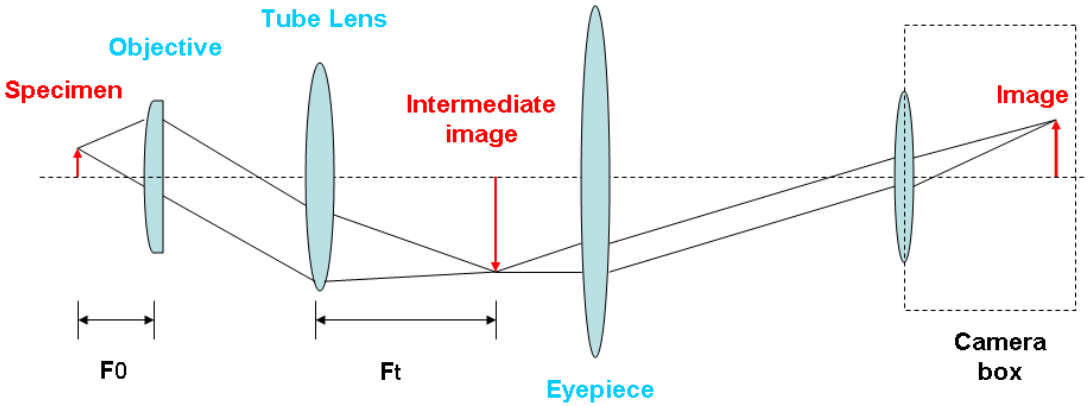

Fig. 3.1.1. Optical path of an infinity-corrected microscope. F_0 is the focal length of the objective and F_t is the focal length of the tube lens.

The basic OM mechanism is very simple in principle. The optical system contains three key lenses between the object plane and imaging plane. Fig. 3.1.1 illustrates the mechanism of a representative infinity-corrected microscopy system. The specimen is located at the focal point of the objective. Therefore, a parallel light passing through the objective is obtained between the objective and the tube lens. This area is also named as the infinity space, which can be used to input some functional accessories such as

polarizers or retardation plates. After passing through the tube lens, parallel light begins to gather at the focal point, where the intermediate image is obtained. The magnification of the objective in an infinity optics microscope is defined as the ratio of focal length of the objective F_0 and that of the tube lens F_t. Images can be obtained visually or through a camera box.

POM is a contrast enhancing technique, which can improve imaging quality of birefringent materials. Therefore POM can find wide applications in scanning specimens with optically anisotropic properties, such as minerals, ceramics, polymers, and biomacromolecules. POM techniques have also found new applications to target anisotropic assemblies in biological studies.

POM uses a polarized light as a source. In a polarized light, the electric field vector is restricted to one plane. In contrast, the electric field vectors of non-polarized lights vibrate in all directions perpendicular to the light propagation direction. To obtain non-polarized light sources, a filter (polarizer) is always needed to block light elements from the other planes in non-polarized lights. Polarized lights are sensitive to the anisotropic property of materials.

Materials can be separated as being isotropic or anisotropic, based on their optical properties. Isotropic materials demonstrate the same optical properties when a light goes through them from any direction, which means that they only have one refractive index n. Isotropic solid materials include glassy materials and cubic crystals. Anisotropic materials, however, have at least two refractive indices, showing different optical properties by varying the incident light with crystallographic axes. Around 90% of solids belong to anisotropic materials. Anisotropic materials can split lights into two orthogonal components with different velocities, namely the ordinary and extraordinary ones. This phenomenon is defined as birefringence B, which can be written as:

$$B = \left| n_{high} - n_{low} \right|$$

The POM technique features the interference of two components in polarized light since the two components reunite after passing through anisotropic materials along the same optical path (Fig. 3.1.2). Two polarizers are always used together in POM. The first polarizer is located before the specimen, producing polarized light. When the polarized light enters the birefringent material, it splits into two individual and orthogonal

components. These two components finally enter the second polarizer (analyzer) and recombine with constructive or destructive interferences. If both the thickness d and the birefringence of the sample are known, it is possible to quantitatively calculate the retardance R, which is shown as the degree of phase shift as follows:

$$R = dB$$

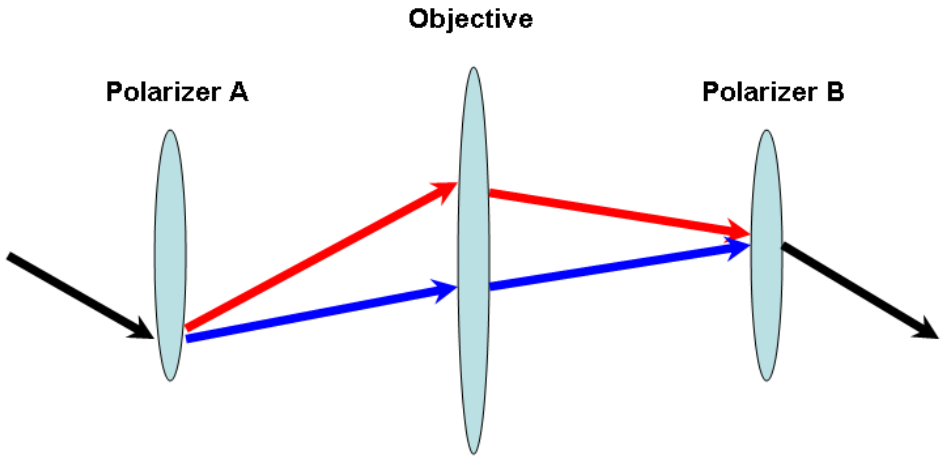

Fig. 3.1.2. The schematic figure shows the principle of POM technique. Black lines represent the incident and the recombined lights; red and blue lines show ordinary and extraordinary waves, respectively.

3.1.2 Atomic Force Microscopy

Atomic Force Microscopy (AFM) was invented by Gert Binnig and others in 1986.[48] Since then, it has become an impacting technique in material and biology science as well as in nanotechnology. Generally, AFM works by scanning the sample with a mechanical probe (Fig. 3.1.3A). A cantilever with a sharp tip scans the sample surface. The tip is made by Si or Si_3N_4 with its radius on the order of nanometers. When the tip is close to the sample, there are interactions between the tip and the sample surface. Consequently, the force between the sample and tip deflects the cantilever according to the Hooke's law (Fig. 3.1.3B). The deflection is magnified by corresponding deflections of the laser beam, the signal of which is captured by a photodiode detector for calculation. AFM mainly has three classical operating modes as follows.

Contact mode is characteristic for the close distance between the sample and tip (Fig. 3.1.3B). Therefore, the force observed is repulsive. During the measurement, the force is kept constant, which is maintained by changing the distance between the sample and tip

from the deflection of the cantilever. The relationship between the force F and the deflection x can be described by the Hooke's law:

$$F = -kx$$

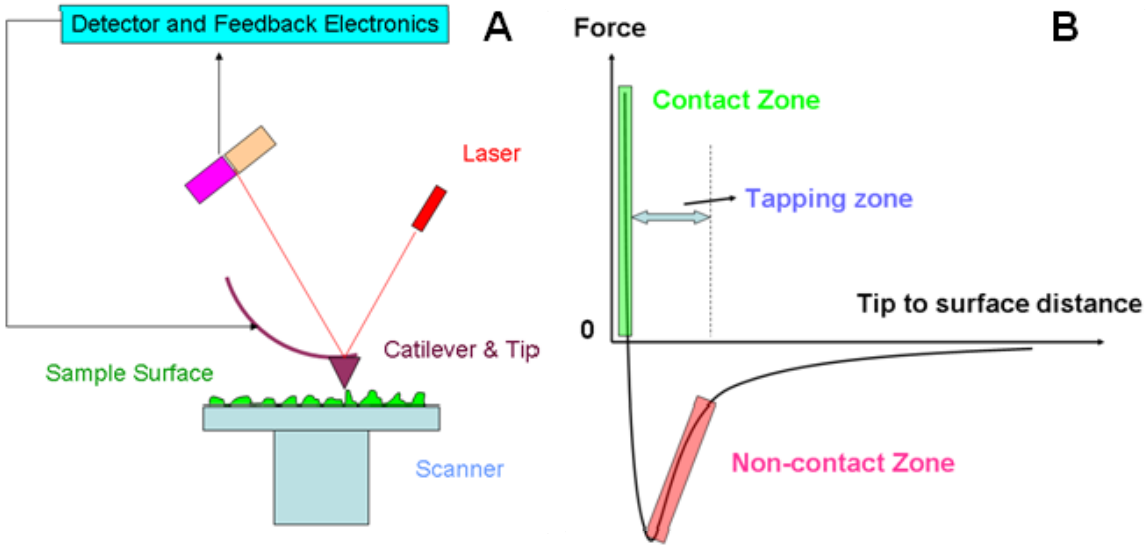

Fig. 3.1.3. Image **A** is the schematic diagram of AFM. Image **B** indicates the relationship between the scanning mode and the range of forces.

Non-contact mode works in the attractive zone, where the attractive forces are several orders of magnitude weaker than the repulsive forces (Fig. 3.1.3B). Therefore, the amplitude of oscillation in non-contact mode is just a few tens of angstroms, and stiff tips are preferred to escape from being pulled into the sample. Non-contact mode builds the relationships between the resonance frequency of the cantilever and the topography of the sample. Changes in the resonance frequency of a cantilever can be used to measure the changes in the force gradient, which reflects the distance between the surface and tip. Therefore, the topography is obtained by scanning the whole surface. In non-contact mode, the resonant frequency or vibration amplitude of the cantilever is kept as constant by using a feedback from a loop system. The topography of the sample is obtained by moving the scanner up and down when it is scanning across the sample.

In both of the above modes, the tip is more sensitive to the topography of the surface when the forces between the tip and the surface increase. However strong forces will perturb the surface, which is a severe problem in detecting the soft biological materials. This problem has been overcome by using **tapping mode**. It allows scanning of samples

which are easily damaged or stay loose on the substrate. The high frequency (50–500k Hz) and sufficient oscillation amplitude (usually ~20–100 nm) greatly reduce adhesion forces between the tip and sample. In addition, the vertical oscillation minimizes sample damage. In tapping mode, interactions between sample and tip fluctuate between being repulsive and attractive (Fig. 3.1.3B). When the tip goes near to the sample, van de Waals forces, dipole-dipole interactions, and electrostatic forces decrease the oscillation amplitude. Using a feedback circuit, the oscillation amplitude is kept constant by changing the distance between the tip and sample. Therefore, the oscillating force is mapped during scanning. Tapping mode is so gentle that it works well for scanning polyelectrolyte chains several ångströms in height.[49]

Tapping mode can work in air as well as in fluid. Since fluids tend to decrease the resonant frequency of the tip, the oscillation of the entire fluid cell drives the oscillation of the cantilever. The frequency is in the range of 5,000 to 40,000 cycles per second and very soft cantilevers are preferred for scanning with tapping mode. The combination between tapping mode and fluid devices provides an excellent opportunity for in-situ observation of soft materials without dehydration and crystallization in solution. The fluid is changeable and it is easy to control parameters such as temperature, concentration of solute and inert salts, *etc.* AFM is indeed unique in providing in-situ and continuous scanning (another choice is the combination of TEM and fluid cell), even there are technical problems such as the fragility of crystals and the fixation of substrate.

AFM is advantageous compared with OM and electron microscopy for several reasons. Primarily, AFM can operate with a high resolution in vacuum, air, and fluid environments. The lateral resolution is on the nanoscale and the height one is as precise as 0.1 nm. Secondly, there is no perturbation during the measurement. Crystals grow without feeling the existence of the tip, and a series of continuous pictures can be recorded per second. Last but not the least, AFM needs no special sample pretreatments such as coatings and drying, and the scanning can proceed under ambient conditions. However, there are still several drawbacks. Firstly, the time resolution is still not good enough for detecting fast processes. In addition, AFM cannot measure surfaces with steep walls. AFM may also give artifacts during measurements, due to thermal drifts or incorrect choices of tips.

3.1.3 Scanning Electron Microscopy

The size resolution in scanning electron microscopy (SEM) is highly improved compared with OM and it is possible to measure samples over a wide range of magnifications (e.g. between 10 and 500,000). SEM is very simple in principle. A fine beam of electrons is thermoionically emitted from the electron gun to the sample surface. The beam scans across the sample surface with energy of 5–40 keV and each spot has a diameter on the nanoscale. When the electron beam hits the sample surface, the scattering and adsorption of electrons from the sample decrease the electron energy, resulting in an interacting thickness from hundreds of nanometers to several micrometers. Interaction strength depends on the initial electron energy, the elemental composition, and the sample density. The magnification of the image depends on the electron spot size on the sample surface. The secondary electron signals are captured by a detector and are used to create images of the current distribution (Fig. 3.1.4).

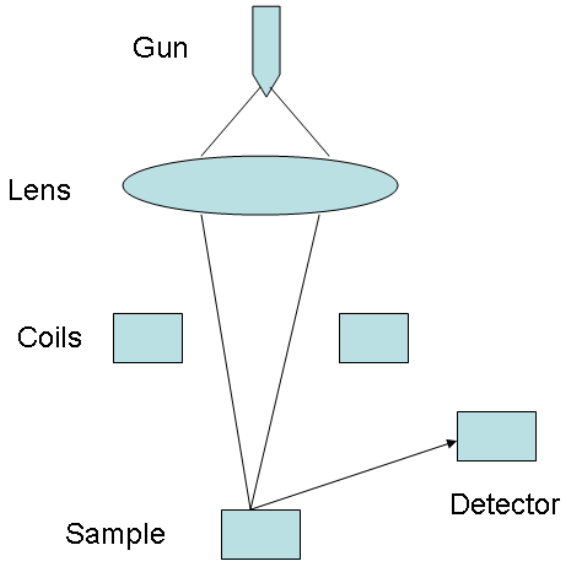

Fig. 3.1.4. The schematic figure shows the components and the mechanism of SEM. The whole system is in vacuum.

Practically, the sample surface must be electrically conductive. Non-conductive samples are normally coated with a thin layer of conducting material (e.g. gold or platinum) before SEM scanning. SEM has wide applications and can display 3D appearance of samples with a certain thickness. Special techniques, such as cryo-SEM

and environmental SEM, are designed to scan soft samples, such as biomacromolecules and polymers.

3.2 Small-angle Neutron Scattering

Small-angle Neutron Scattering (SANS) is one of three commonly used scattering techniques, alongside light scattering and small angle X-ray scattering. Using a neutron beam as the source, SANS is used to analyze non-crystalline materials and provides information regarding composition, shape, and structural size over the 10–10^4 Å range. Therefore, SANS is a popular characterization technique in the polymer, nano, biological, material, and colloid sciences.

When a neutron beam is introduced into the instrument, a velocity selector can choose neutrons with a certain wavelength to pass through (Fig. 3.2.1). Then, a series of collimators produce a parallel beam, which passes through the sample. During the interactions between the beam and sample, some neutrons are absorbed and others are scattered. A detector, located behind the sample, collects the scattered neutrons. In SANS, only coherent elastic scattering is of interest, which contains information of intra- and inter-particle interactions. The contributions from incoherent and inelastic scattering stay in the background and are subtracted before data analysis. The analysis starts from counting the flux of the scattered neutrons I' and comparing it with the incident beam density I. The scattering vector q is the modulus of the incident wave vector s and scattered wave vector s'. The structural size z is easily derived from the following equation $z = 2\pi / q$, which makes a quick judgment for the structural size from the $I(q) \sim q$ curve.

The scattering vector q is also defined by the modulus of the incident wave vector s and scattered wave vector s'. The scattered flux I' is expressed in the following way:

$$I' = I\Omega\varepsilon T V_b \frac{\partial \psi}{\partial \Omega}$$

where I is the incident flux, Ω is the solid angle, ε is the detector efficiency, T' is the sample transmission, V_b is the beam volume, and $\partial\psi / \partial\Omega$ is the differential cross section. The first three items are instrumentally specific and the other three are sample

dependent. Compared with the first five straightforward parameters, the term $\partial\psi/\partial\Omega$ needs special treatment and extensive analysis. It can be written into the following way:

$$\frac{\partial\psi}{\partial\Omega}=\frac{N_p}{V}(\rho_p-\rho_0)^2V_p{}^2P(q)S(q)$$

where N_p/V is the number density of the scattering body, $(\rho_p-\rho_0)^2$ is the contrast factor (the square of the scattering length density difference between the studied materials and medium), V_p is the volume of one scattering body, and $P(q)$ and $S(q)$ are the shape and structure factor, respectively. The concepts of $(\rho_p-\rho_0)^2$, $P(q)$, and $S(q)$ are going to be introduced separately in the following paragraphs.

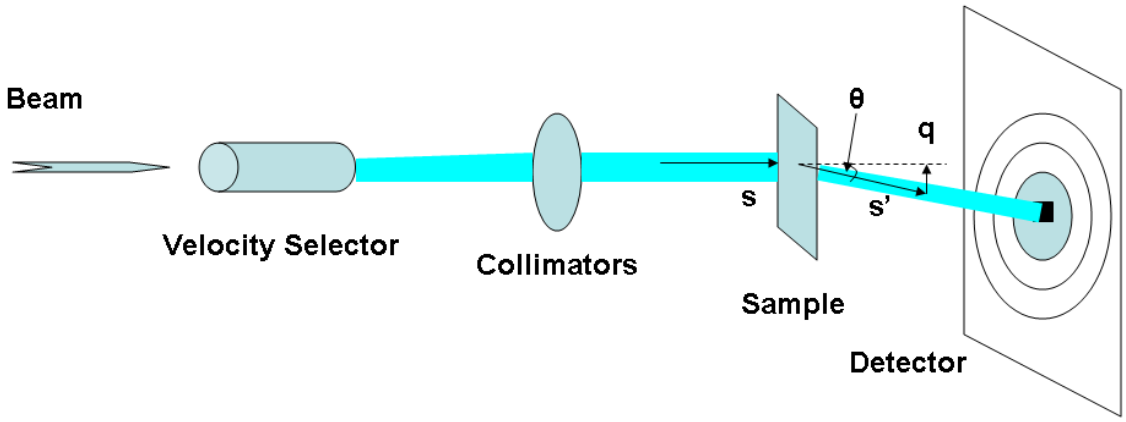

Fig. 3.2.1. Schematic diagram of a typical SANS instruments.

Scattering bodies often contain different components. The contrast in SANS is different from that in small angle x-ray scattering, where the contrast comes from the difference of electron density. Each elements interacting strongly with neutrons have different scattering length densities ρ (Table 3.2.1). Another important point is that different isotopes have different contrasts. For example, hydrogen and deuterium have very different scattering lengths, based on which the contrast matching method is designed.

Table 3.2.1 Some examples of scattering lengths of atomic nuclei

Atomic Nucleus	^{1}H	^{2}D	C	N	O	S	Ti
Scattering Length (fm)	-3.741	6.671	6.646	9.362	5.803	2.847	-3.438

An introduction to the contrast matching method. In a model three-component system, where components A and B are mixed in a solvent C, A and B have different contrasts but only the mixed SANS information from both A and B is acquired by using a deuterated C. However, the contrast between A and C disappears by using a certain ratio of the protonated and deuterated C. In this regard, information from B can be obtained separately. Similarly, information from A can be obtained when the contrast between B and C disappears. The contrast matching is a key method for understanding interactions and structural details in multi-component samples, which cannot be analyzed by other ways.

The term $P(q)$ arises from intra-particle interactions and describes how the scattering is affected by the size and shape of a scattering body. Various expressions for different shapes can be deduced from a general form of van de Hulst's equation.[50] For one scattering body, $P(q)$ has the following form:

$$P(q) = \int \rho(g) \left\langle e^{iqg} \right\rangle dg$$

where g is the vector from the scattering center to the one integrating particle within the scattering body. The form factor of one scattering body is obtained by integrating all particles within the body. Practically, the data analysis starts from fitting the experimental data with a model for possible structures of scattering bodies. If the model does not fit well, it will be replaced by another one. The above process is repeated until a model with a good fit is found out.

As for dilute systems, just considering $P(q)$ is enough. However, the $S(q)$ term must be considered in concentrated systems where the collision chance between scattering bodies is not omittable. $S(q)$ can provide information such as the ordering and position of scattering bodies. It is a function of the inter-particle interactions, and as such can be defined as:

$$S(q) = 1 + \sum_{a \neq b}^{N} \left\langle e^{-iq(g_1 - g_2)} \right\rangle$$

where g_1 and g_2 are vectors from the scattering centre to the centre of the scattering bodies **1** and **2**, respectively.

SANS requires a neutron source, either from a nuclear reactor or from an accelerator based spallation source. Therefore, SANS measurements are only feasible at large scale facilities. Furthermore, expensive deuterated solvents or chemicals are needed, which consequently elevates the cost for SANS measurements.

3.3 Ultracentrifugation

Analytical ultracentrifugation (AUC) was developed by Theodor Svedberg in 1923. Later, Edward Greydon Pickels introduced vacuum systems into ultracentrifugation to decrease the friction. Generally, ultracentrifugation can be divided into two types: AUC and preparative ultracentrifugation. The preparative technique is mainly used for separating components in colloidal or biological systems. AUC is monitored by an optical detection system for measuring the molecular weight of polymers as well as the size and morphology of colloids. Sedimentation velocity and sedimentation equilibrium experiments are two types of AUC measurements. During the course of the research presented in this thesis, sedimentation velocity measurements were performed, providing both a sedimentation and diffusion coefficient. The size and morphology of colloids as well as the interactions between colloids can also be obtained from the data analysis.

When the solute particles move at a constant velocity u, three forces are equilibrated (Fig. 3.6). The centrifugal force F_s is proportional to the particle mass m and acceleration, the latter of which is determined by its distance to the axis of rotation r and the square of the angular velocity ω_r. These parameters allow measurement of sedimentation velocity and are written as follows:

$$F_s = m\omega_r^2 r$$

The buoyant force F_b has a similar description, where replacing mass of particle m is replaced with mass of solvent with the same volume m_0:

$$F_b = m_0\omega_r^2 r$$

The relationship between m_0 and m is described as:

$$m_0 = m\bar{v}\rho_s$$

where $\bar{v}$ is the partial specific volume and ρ_s is the density of the solvent. If the density of the solvent is lower than that of the particle, F_s is larger than F_b. Consequently, the combined force brings particles in the direction far away from the rotation center and sedimentation happens. When a particle is moving, it has to overcome the frictional force F_f, which is proportional to the velocity u and the frictional coefficient f:

$$F_f = fu$$

Both F_f and F_b act on the particle towards the direction to the rotation centre. After very short time, the particles moves at constant velocities and the three forces come into balance:

$$F_s + F_b + F_f = 0 \text{ or } m(1-\bar{v}\rho_s)\omega^2 r - fu = 0$$

Rearranging the terms for the particles on one side and those from the measurement on the other side, the above equation can be rewritten as follows:

$$\frac{m(1-\bar{v}\rho_s)}{f} = \frac{u}{\omega^2 r} \equiv se$$

where se is the sedimentation coefficient and depends only on the properties of particles instead of measuring parameters. Molecules or colloids with different molecular weight, size and morphology have a different se. Experimentally, se is determined by measuring u.

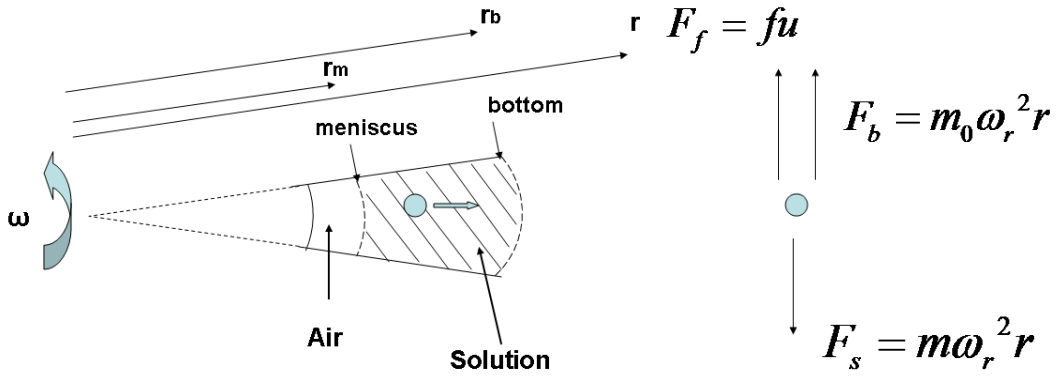

Fig. 3.6. The left figure is the schematic setup of a sedimentation measurement. The right figure shows the forces acting on the solute particle within the solution.

Because of the existence of a concentration gradient, diffusion begins to increase to counteract the sedimentation process. The diffusion coefficient D is determined by the rate of boundary spreading, which can be written as follows:

$$D = \frac{RT}{N_A f}$$

Combining the equations defined for se and D, the frictional coefficient f is eliminated as:

$$\frac{se}{D} = \frac{M_s(1-\bar{v}\rho_s)}{RT}$$

where M_s is the molar mass of solute. The above equation is also named the Svedberg equation. If the density of the particle is known, the size of the spherical particle r_p is measured by using the following rearranged Svedberg equation:

$$r_p = \sqrt{\frac{18\eta s}{\rho_p - \rho_s}}$$

4. The DL-Glutamic Acid–Polyethyleneimine–Water–EtOH Systems

Abstract

The use of polymeric additives can induce complex phenomena during crystallization or precipitation processes in many cases. Therefore, understanding the phase diagram of a model precipitation system can provide a more complete picture for the understanding of the precipitation. Herein, the development of a quaternary phase diagram for the DL-Glutamic acid (Glu)–polyethyleneimine (PEI)–water–EtOH system is introduced. The tuning of two system parameters, namely Glu/PEI (w/w; **φ**) and EtOH/water (v/v; **λ**) was investigated with the aim of understanding how the use of the PEI additive effects Glu precipitation. Precipitates, coacervates, or homogeneous mixtures were observed in sequence as a result of decreasing **φ** from 9/1 to 1/10. The phase diagram of coacervation systems are then presented by constructing three representative ternary phase diagrams by keeping **φ** or **λ** as a constant. The volume fractions of coacervates were measured by centrifugation, and their composition was determined by nuclear magnetic resonance spectroscopy (NMR). The results presented herein indicate that the formed coacervates are thermodynamically stable, distinguishable from the metastable polymer-induced liquid precursor (PILP) phase.

4.1 Phase Diagram and Composition

4.1.1 Introduction

Evidence in biomineralization and crystallization indicates the existence of precursors. Among these precursors, there are three promising ones: amorphous phase,[51, 52] clusters,[22, 23] and polymer-induced liquid precursor (PILP).[17] The concept of PILP was put forward initially by Gower *et al*.[17] PILPs are formed when $CaCO_3$ is crystallized in the presence of $\mu g \cdot ml^{-1}$ amounts of a polyacid (e.g. polyacrylic or polyaspartic acid). A special feature of crystallizations passing through a PILP route is that crystallization can occur directly within the PILP phase. PILP has also been found in other inorganic materials such as $Ca_5(PO_4)_3(OH)$,[53] $SrCO_3$,[54] and $BaCO_3$.[54, 55] Although PILP is a very promising precursor for preparing complex crystalline forms, the understanding of their formation and transformation into crystalline materials is poorly described because they crystallize upon centrifugal isolation. In addition, the phase composition and possible structure of the PILP phase remain as yet unexplored. In search of a more suitable model system, the Cölfen group has extended the PILP approach to organic systems including amino acid/polyelectrolyte[56] and pigment/copolymer.[57] As the sizes of organic molecules are larger than that their inorganic counterparts, the lattice energy of organic crystals is generally lower. Therefore, the crystallization tendency is lower, which allows for the isolation and investigation of the resulting organic PILP phase.

Interactions between polyelectrolytes and oppositely charged NPs,[58] metal ions,[59] or (macro)molecules including organic molecules,[56] surfactants,[60] proteins,[61] and polyelectrolytes[62] are known to produce coacervates, homogeneous mixtures, and precipitates. Different phenomena are proposed to depend on system stoichiometry and interaction strength between the oppositely charged items. For example, a highly hydrated homogeneous mixture is obtained in the protein-polyelectrolyte solution when the volume ratio of protein is low in the complex, whereas coacervates are obtained when the complex net charge is near to zero; precipitation happens when the volume ratio of protein is high, and the electrostatic interactions are very strong.[63] The interactions between proteins and polysaccharides have also been extensively investigated in aqueous

solutions via the control of pH, inert salt concentration, and temperature.[64] As such the formation of coacervates can be divided into two steps: a primary formation of complex structures and a secondary aggregation into a continuous phase.[65]

The work presented herein is the continuous study of organic PILP systems for the understanding of their phase diagram and composition. The construction of phase diagrams for a quaternary DL-Glutamic acid (Glu)–polyethyleneimine (PEI)–water–EtOH system by changing Glu/PEI (w/w; **φ**) and EtOH/water (v/v; **λ**) is presented and discussed. It is of special interest to see how the values of **φ** influence the existence of precipitates, coacervates, or homogeneous mixtures, and the physical properties of the coacervates. The ternary phase diagram is then investigated at constant values of **φ** or **λ** to clarify the coacervation zone in each case. The composition of coacervates is finally examined by nuclear magnetic resonance spectroscopy (NMR). The systematic study of the above quaternary system indicates that thermodynamically stable coacervate phase must be distinguished from the metastable PILP phase.

4.1.2 Phase Diagram of Glu–PEI–water–EtOH systems

The corresponding phase diagrams for the investigated systems are determined by three standard steps. First, a series of aqueous solutions with various (Glu+PEI) weight fractions were prepared at a constant **φ**. Then the titration of an aqueous solution with EtOH was performed to determine the critical value of **λ** in each solution. Finally, the phase diagram was obtained by calculating the mass ratio of each component in the quaternary mixture.

For the model Glu-PEI-water-EtOH systems, precipitation (Fig. 4.1.1B), coacervation (Fig. 4.1.1A), or the formation of a homogeneous mixture can be observed according to the altering the value of **φ** and **λ**. The relationship between the phase behavior and the value of **φ,** when **λ** = 9, indicates that coacervation occurs, when **φ** is between 2/1 and 1/5 (Fig. 4.1.2). When **φ** is higher than 2/1, the precipitation of Glu happens over a wide range of **λ** as EtOH is a non-solvent for Glu. A homogeneous mixture is observable when **φ** is equal or lower than a value of ~1/5 to 1/6. The boundary line also depends on the value of **λ** and the mass fraction of (Glu+PEI). It is proposed that the branched PEI component can form Glu-PEI complexes and provide Glu molecules

protection from precipitation in the water-EtOH mixture. Coacervation occurs when Glu can form stable complexes with PEI in the quaternary mixture. Coacervate is a phase rich in Glu-PEI complexes and is in equilibrium with a supernatant phase. Homogenous mixtures are formed by using the aqueous solution with high values of **φ**, as PEI is miscible in EtOH and water. In the quaternary mixtures by using high values of **φ**, PEI cannot provide enough protections for Glu from being precipitated out. Therefore, the precipitation of Glu happens.

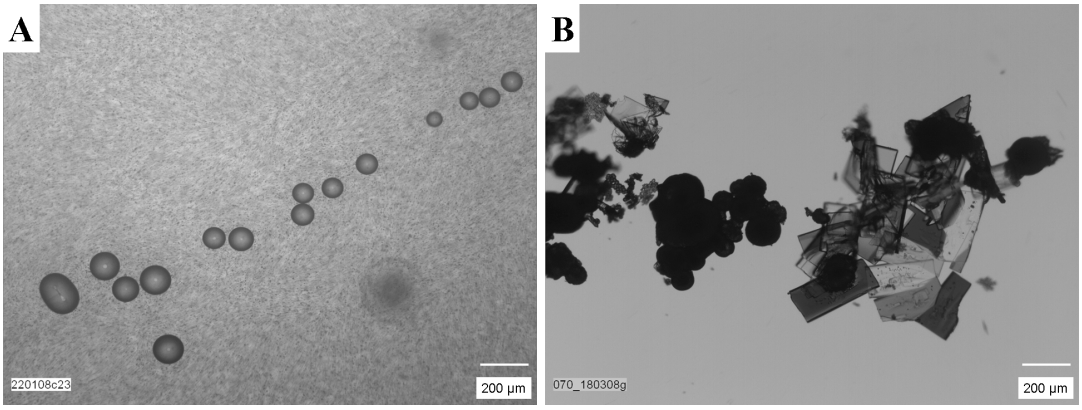

Fig. 4.1.1. Image **A** shows the existence of coacervate phase in the water-EtOH mixture. Image **B** shows a representative image of Glu precipitates.

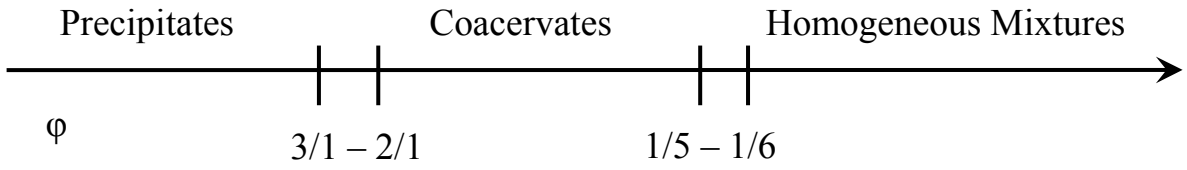

Fig. 4.1.2. The relationships between the values of **φ** and the phase behavior (**λ** = 9).

As it is not straightforward to observe quaternary phase diagrams, three ternary phase diagrams were drawn to illustrate the phase behavior of the quaternary system by keeping **φ** at 2/1, 1/2 and 1/5, respectively (Fig. 4.1.3). To obtain the coacervate as a thermodynamically stable phase, another route was applied for the preparation of samples. By mixing Glu powder and PEI directly in a water-EtOH mixture, the volume and composition of coacervates were in fact the same as those from the standard stepwise sample preparation. Since coacervate can be obtained from different routes, it is treated as a thermodynamically stable phase.

All three phase diagrams for the prepared system show the similar behavior (Fig. 4.1.3). With an increase in (Glu+PEI) weight fraction, less EtOH weight fraction is needed to induce the coacervation process in the case of the homogeneous mixture. The weight fraction of water increases first, followed by a decrease during the increase of EtOH weight fraction. The main difference among three diagrams is the various critical values of EtOH weight fraction. Interestingly, only a ~0.2–0.6 EtOH weight fraction is needed to induce coacervation (Fig. 4.1.3A). However, the value has to be increased to ~0.4–0.8 and ~0.5–0.9 when **φ** is 1/2 (Fig. 4.1.3B) and 1/5 (Fig. 4.1.3C), respectively. Compared to PEI in the quaternary mixture, using **φ** = 2/1 aqueous solutions, a relatively large amount of PEI in the quaternary mixtures by using **φ** = 1/2 or 1/5 aqueous solution can provide more protection for Glu-PEI complexes and stabilise them in the water-EtOH mixture. Therefore, EtOH weight fraction has to be increased to a higher value to cause the coacervation of Glu-PEI complexes in the latter solutions.

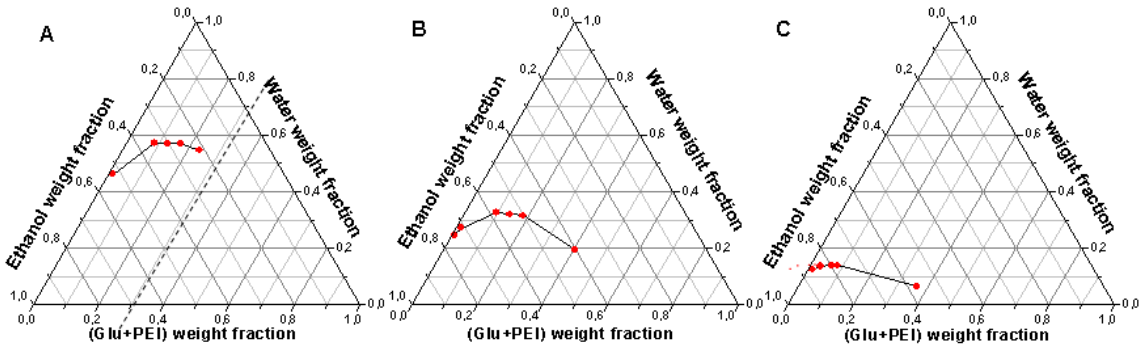

Fig. 4.1.3. Three images are ternary phase diagrams with **φ** at 2/1 (image **A**), 1/2 (image **B**) and 1/5 (image **C**). Coacervate exists below the boundary line, whilst the homogenous solution stays above. The dashed line in image **A** is the solubility line of (Glu+PEI) in aqueous solution.

Then, the physical properties of coacervates including their volume and composition are investigated. Both the volume of coacervate and quaternary mixture can be conveniently read on the vessel for the calculation of the volume fraction of coacervate, indicating a linear relationship between the volume fraction of coacervate and the weight fraction of (Glu+PEI) in each quaternary mixture by keeping constant values for both **φ** and **λ** (Fig. 4.1.4A-C). The EtOH effect was systematically investigated by diluting the same aqueous solution with various volumes of EtOH (Fig. 4.1.4D). The volume fraction

of coacervate can be as high as ~0.7 near to the critical value and decreases linearly upon the addition of EtOH.

Coacervate formation was observable by the naked eye, such that by mixing concentrated aqueous solution with EtOH at high values of **λ**, the transparent and continuous coacervate phase was formed within a matter of seconds. On the other hand, a turbid mixture was obtained by mixing the diluted aqueous solution with a large volume of EtOH. Such a turbid mixture can take from hours to days to precipitate into a small volume continuous phase. The kinetics of the coacervation process for the presented systems can then be separated into two key steps in sequence: the formation of coacervates, and their merging into a continuous phase. The occurrence of these two separate processes is a common phenomenon in coacervation processes.[65]

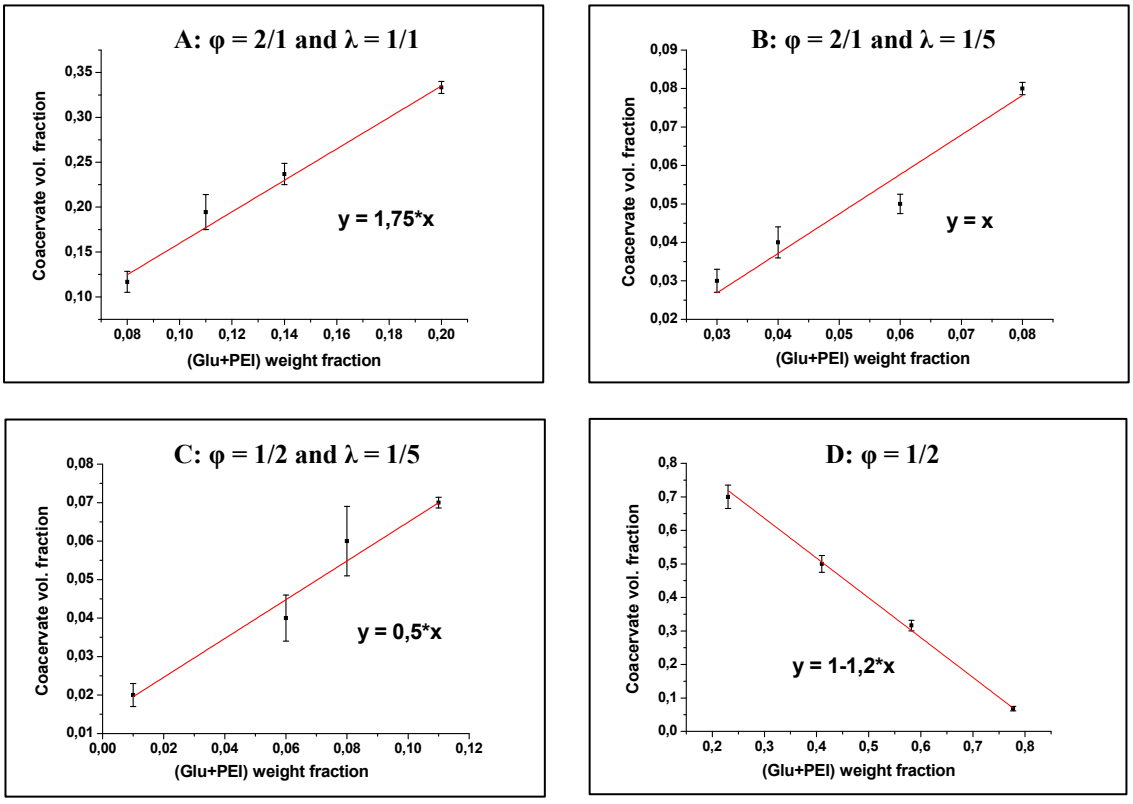

Fig. 4.1.4. Images **A-C** show the relationships between the volume fractions of coacervate and the weight fractions of (Glu+PEI) in each quaternary mixture. Image **D** indicates that the volume fraction of coacervate is decreasing with the increase of EtOH weight fraction (composition: Glu wt% = 30 and PEI wt% = 15 with water as solvent).

4.1.3 The Composition of Coacervates & Supernatants

The coacervation process not only accumulates the solute into the coacervate phase, but changes the values of **φ** in both phases from the initial one. Therefore, the compositions of coacervates and supernatants were measured by NMR to determine the values of **φ** in each phase. The NMR data analysis is based on the peak ratio of γ-CH_2 on Glu and the broad peaks of PEI (Fig. 4.1.5A). Firstly, a series of Glu-PEI aqueous solution with various **φ** values were measured to obtain a standard calibration curve, which shows the relationships between the peak ratio and **φ** (Fig. 4.1.5B). Then, the peak ratios from coacervate and supernatant were measured separately and calculated to determine the composition of both phases.

Four series of experiments were performed to understand how (Glu+PEI) mass fraction affects the composition of coacervate and supernatant by varying the values of **φ** or **λ**. The results are summarized in Fig. 4.1.6. In Fig. 4.1.6A-B, it is clear that the composition of coacervate and supernatant stays nearly constant during the change of (Glu+PEI) mass fraction. Interestingly, the values of **φ** in the supernatant are slightly higher than those found in the coacervate. The similar results were observed in Fig. 4.1.6B, where **λ** = 5.

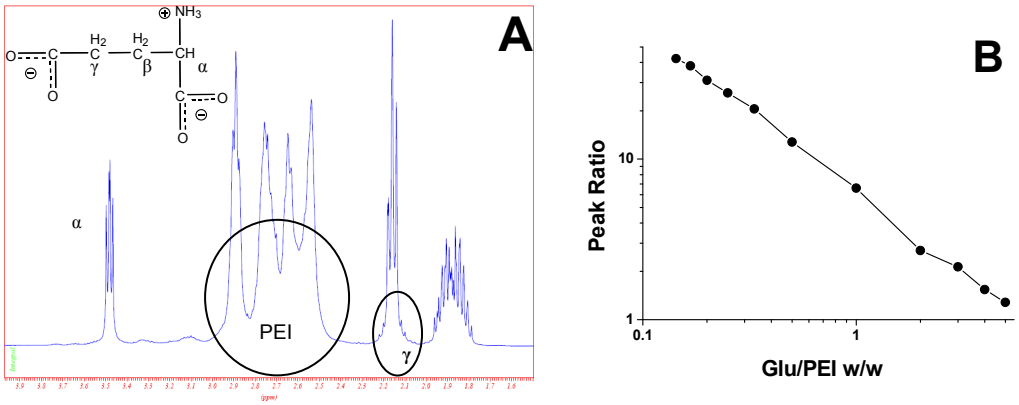

Fig. 4.1.5. Image **A** is an example of NMR result of Glu-PEI mixture in D_2O. The inserted image is the formula of Glu, where three kinds of hydrogen on the main chain of Glu are designated. Image **B** shows how relationship between **φ** and the ratio of peak areas of the broad peak on PEI and the peak belonging to γ-CH_2 on Glu.

To examine the effect of solvent composition, an aqueous solution at **φ** = 2/1 was mixed with different volumes of EtOH (Fig. 4.1.6C). The values of **φ** in both phases were

found to stay on the similar level, suggesting that for the **φ** = 2/1 sample, dilution by EtOH has no effect on the values of **φ** in the range of **λ** values investigated, and the compositions of both phases are relatively constant. Again, **φ** in the supernatant was found to be slightly higher than that in the coacervate.

The values of **φ** in coacervate and supernatant phases can be varied by changing the values of **φ** in the aqueous solutions. A series of aqueous solutions with **φ** = 1/2 were used to examine how the solute concentration affects the compositions of coacervate and supernatant (Fig. 4.1.6D). The values of **φ** in the supernatant and coacervate were observed to decrease with the increase of (Glu+PEI) weight fraction. This is different from Fig. 4.1.6A-C, where the values of **φ** in the coacervates are higher than those in the supernatants. In addition, the decrease rate of **φ** in the supernatants is higher than that in the coacervate with the increase of (Glu+PEI) mass fractions.

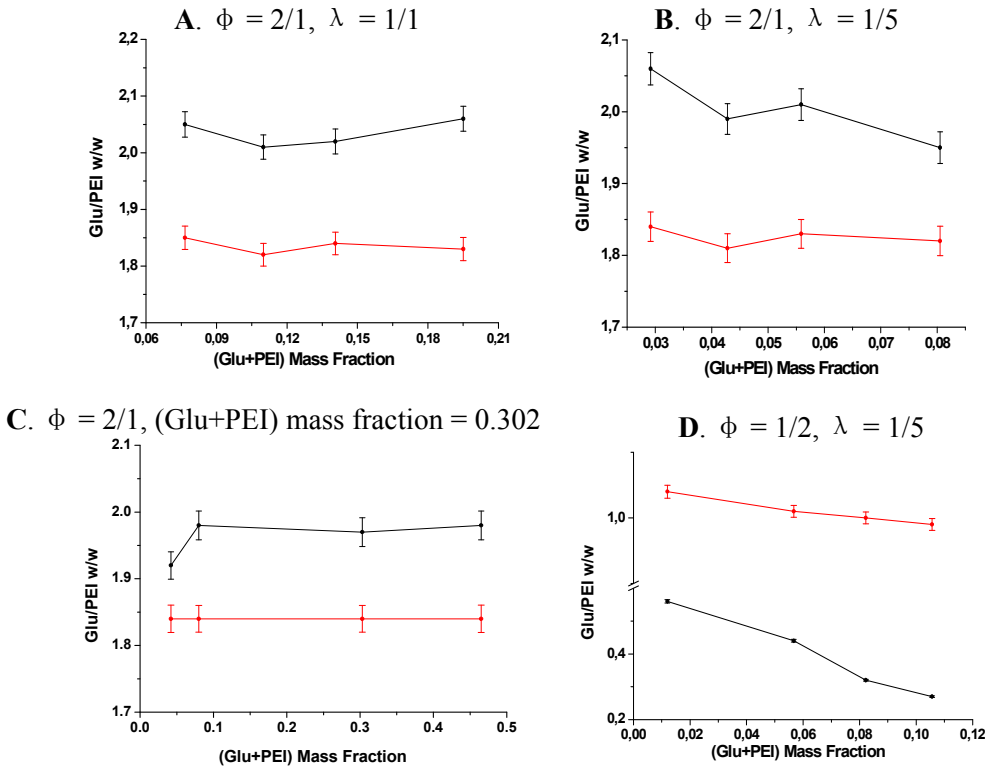

Fig. 4.1.6. Four figures show the relationships between the (Glu+PEI) mass fractions and the values of **φ** in supernatant and coacervate phases. Data in the red and black lines represent the results from coacervates and supernatants, respectively.

After knowing the values of **φ** in coacervate and supernatant, it is necessary to know the solute mass distribution in both phases. Therefore, solid masses in a coacervate and supernatant after solvent evaporation were measured. The (Glu+PEI) mass fractions in the coacervate phase were found to grow as a result of an increase in the initial (Glu+PEI) mass fraction of the aqueous solution. For example, 94 wt% of the solute goes to the coacervate phase when (Glu+PEI) mass fraction is 0.302 in the aqueous solution, whilst the value drops to 62 wt% when using an aqueous solution with (Glu+PEI) mass fraction at 0.129 (**λ** = 1 in both cases). Increasing the value of **λ** also brings slightly more solute into the coacervate phase. For example, 95.1 wt% solute goes to the coacervate phase when **λ** is 5 compared to 94.0 wt% with **λ** = 1 ((Glu+PEI) mass fraction = 0.302; **φ** = 2/1).

Coacervation is a densification process and can produce a coacervate rich in solute, such that the coacervate phase can take up to 96 wt% initial solute. Importantly, it is not necessary that the value of **φ** in the coacervate is higher than that in the supernatant. A possible explanation is that the solute-diluted supernatant can tolerate the higher **φ** than the solute-concentrated coacervate. However, this phenomenon appears in a very narrow **φ** range, and the values of **φ** in the supernatant are lower than those in the coacervates when the value of **φ** in aqueous solution is lower than 2/1. The **φ** difference in both phases again disappears when the homogenous mixture is obtained by using an aqueous solution with **φ** = 1/7. Considering that the precipitation of Glu happens in the quaternary mixture by using aqueous solutions at the values of **φ** higher than 3/1, the values of **φ** in the PILP phase can be lower than those in the supernatant.

In short, we provide the phase behavior of a quaternary Glu–PEI–water–EtOH system. The presented model system is used to aid a description of interactions between the target molecules and oppositely charged polyelectrolytes, and in turn how this interaction influences the phase behavior of such a quaternary system. It is found that these interactions can effectively be tuned by varying Glu/PEI w/w and water/EtOH v/v, resulting in precipitation, coacervation or the formation of homogeneous mixtures. Coacervation is observed to occur over a wide range of Glu/PEI with various volumes, and the composition of coacervates is characterized by NMR. Different from metastable PILPs in the precipitation of Glu, coacervate is a thermodynamically stable phase rich in solute.

4.2 DL-Glutamic Acid–Polyethyleneimine Aqueous Solution

Abstract

The complexes between ions and polyelectrolytes have been attracting extensive research interest as they play key roles in understanding crystallizations and precipitations with charged polymer as additives. This case study presented herein is aimed to understand pre-existing DL-Glutamic acid–polyethyleneimine (Glu-PEI) complexes in aqueous solution, which are then applied for Glu precipitation via mixing with a non-solvent (e.g. EtOH). Two samples with values of Glu/PEI (w/w; **φ**) at 5/1 and 9/1 were investigated by using small-angle x-ray scattering (SAXS), atomic force microscopy (AFM) and ξ-potential. SAXS analysis indicates the coexistence of Glu-PEI complexes and isolated Glu molecules as well as provides morphological and complex size information. AFM imaging indicates the coexistence of isolated and aggregated complexes. Both techniques provide consistent values for the size of such isolated complexes. Aggregated complexes observed by AFM are attributed to the low surface charges, as demonstrated by ξ-potential measurements.

4.2.1 Introduction

Complexes between polyelectrolyte and oppositely charged ions,[66] molecules,[56] macromolecules,[60, 61] and colloids[58] can provide rich phase behavior. Solid precipitates, coacervates, or homogeneous mixtures are obtained by tuning parameters including temperature, pH value, inert salt concentration, molar ratio of oppositely charged molecules.[67, 68] As such complexes are always at nano- to micro-scale, scattering,[63] cryo-transmission electron microscopy (TEM),[69] and atomic force microscopy (AFM)[70] fit the relevant scales of the systems, and can provide the information such as the size and morphology. Furthermore, to understand the structural details is the key to predict the properties of complexes. Therefore, questions such as the conformation of polyelectrolyte and how the oppositely charged items interact with each other need to be answered (e.g. do the oppositely charged items exist as being isolated, randomly or orderly aggregated?). Several techniques need to work collaboratively to answer these questions. In sodium polystyrene sulfonate–lysozyme complexes, the structural information of either item is obtained by contrast matching in small-angle neutron scattering (SANS),[63] and the conformation of proteins can be clarified from infrared spectroscopy[63] and circular dichroism spectra.[71]

Importantly, the complexes in solution play roles during the formation of precursors in biomimetic synthesis. Among polyelectrolytes, anionic ones are of particular interest because they interact with inorganic ions such as Ca^{2+} and Mg^{2+}. Similarly, proteins involved in biomineralization are rich in glutamate and aspartate residues.[72] Several plausible hypotheses have been put forward to understand the multiple roles of complexes during the biomimetic crystallization. For example, amorphous $CaCO_3$ with controllable sizes can be obtained by tuning the Ca^{2+}-poly(acrylic acid) (PAA)complexes and the introduction time of CO_2.[73] In this case, the Ca^{2+} sequestration by the Ca^{2+}-PAA complexes induces a local supersaturation of $CaCO_3$, and the nucleation of $CaCO_3$ happens by using complexes as nuclei. In addition, the Ca^{2+}-PAA complexes also stabilize $CaCO_3$ in an amorphous form. Another mechanism suggests that amorphous $CaCO_3$ comes from polymer-induced liquid precursor (PILP).[74, 75] PILP route is advantageous for producing structures with complex morphologies. The PILP concept

has been extended to amino acid and oppositely charged polyelectrolyte systems.[56] However, the phase behavior of the initial complexes between oppositely charged items during a crystallization process is seldom investigated.

This section is designed to detect the existence of DL-Glutamic acid–polyethyleneimine (Glu-PEI) complexes and to understand their structural details. The coexistence of molecules and Glu-PEI complex was proved by SAXS. In addition, the structural details of complexes were characterized by AFM, SAXS, ξ-potential, and SANS. Understanding complexes in the aqueous solution can shed light on Glu precipitation with PEI as an additive.

4.2.2 Results

First, the relationship between **φ** and the pH value is investigated. Fig. 4.2.1A shows that the pH value increases with the growth of PEI mass fraction when the Glu mass fraction is constant at 0.02. In addition, the pH value increases with the increasing (Glu+PEI) mass fractions by keeping **φ** as a constant. When **φ** ≤ 1/3, the pH value is ~10, which is close to the pK_b of PEI. For example, the pH values in a series of the **φ** = 2/1 aqueous solutions are 5.9, 6.5, and 7.5, when the Glu mass fraction is 0.02, 0.1, and 0.2, respectively. The pH value decides interaction strength between Glu and PEI.

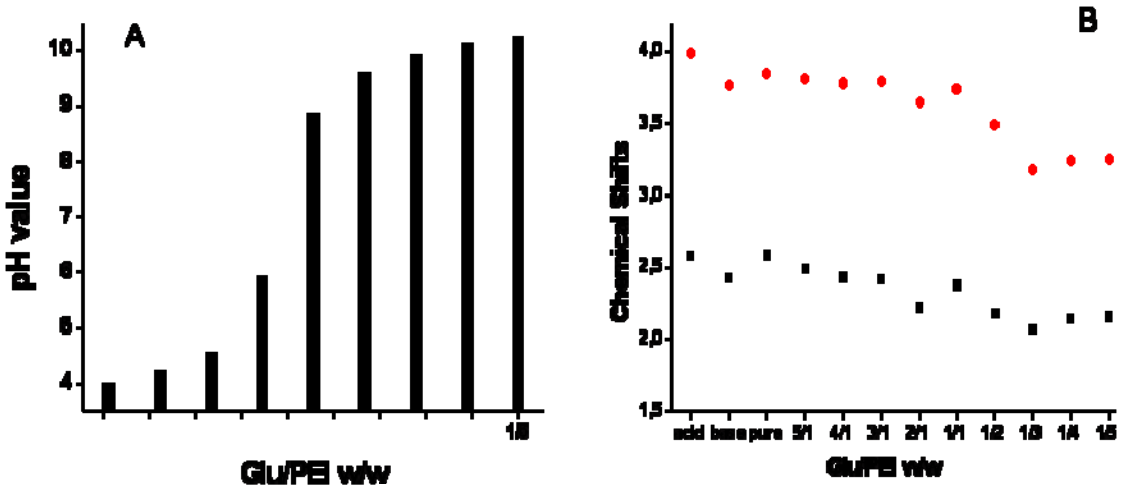

Fig. 4.2.1. Image **A** shows the relationship between the pH value of Glu-PEI aqueous solutions and the values of **φ**. Image **B** indicates the chemical shifts of α-H (black points) and γ-H (red points) on Glu in the Glu-PEI aqueous solutions as a function of **φ**.

NMR was applied to investigate the interactions between Glu and PEI at the molecular level. The chemical shifts of α-H and γ-H on Glu in the Glu-PEI aqueous solutions were recorded and compared with Glu standard (Fig. 4.2.1B). The chemical shifts of solutions with **φ** values from 5/1 to 1/2 are similar to those of pure Glu solutions (e.g. in neutral, acidic or basic conditions). However, the chemical shifts switch to the high field when **φ** ≤ 1/3. A possible explanation is that primary and secondary amine groups on PEI directly interact with α-H and γ-H on Glu, which causes the electron clouds on α-H and γ-H to be denser than those in pure Glu aqueous solution. Results in pH measurement and NMR prove that Glu and PEI interact by electrostatic interactions when pH value is lower than 10.

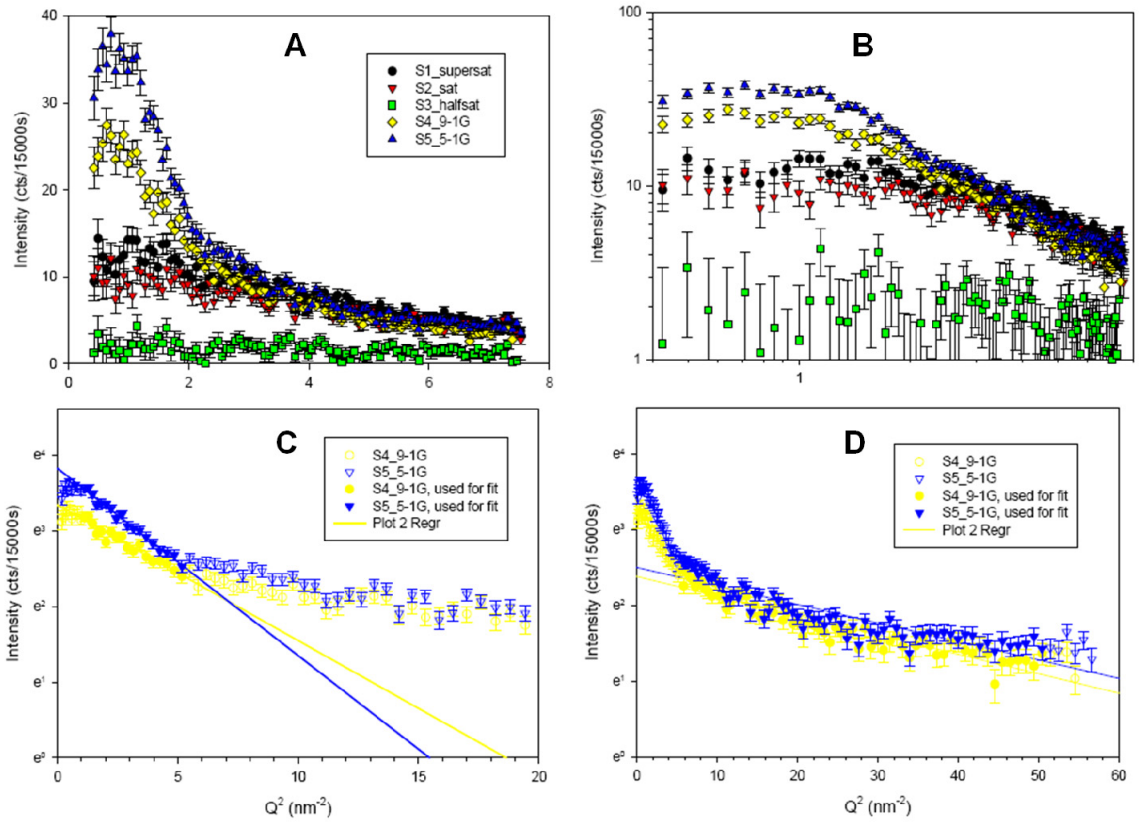

Fig. 4.2.2. The SAXS data from samples S4 (blue) and S5 (yellow). Images **A-B** shows the I(Q)–Q curves. Fig. **B** and **C** show the Guinier plots on different scales.

SAXS proved the existence of Glu-PEI complexes, and provided the information such as their size and morphology. Two samples were selected by keeping the values of **φ** at 9/1 (S4: [Glu] = 40 g·L^{-1}, [PEI] = 4.4 g·L^{-1}) and 5/1 (S5: [Glu] = 40 g·L^{-1}, [PEI] = 8

g·L^{-1}), respectively. Both samples were selected because they were good candidates for Glu precipitation (e.g. mixing with EtOH). The results are summarized in Fig. 4.2.2. There is a relationship $I \sim Q^{-4}$ at the high Q range in Fig. 4.2.2A-B, which suggest the existence of structures with sharp interfaces. The flat curve in the low Q range indicates the existence of spherical objects. Therefore, the Guinier plots show that each sample contains two structures at different scales (Fig. 4.2.2C-D). The sizes of both structures can be calculated by analyzing the Guinier plots. According to Guinier approximation:

$$\ln I = \ln I(0) \ - \frac{R_g{}^2 Q^2}{3}$$

where $I(0)$ means the beam intensity at 0°, and R_g is the radius of gyration. By drawing the $\ln I(Q) - Q^2$ curve, values of R_g can be obtained from the slope. The corresponding sizes at the higher Q range are 0.28 nm and 0.27 nm for S4 and S5, respectively. The sizes are on the molecular scale, and can also be obtained by directly measuring Glu solutions by using analytical ultracentrifugation (data not shown). The evaluated values of R_g in the low Q region are 0.73 nm and 0.86 nm for samples S4 and S5, respectively. The structure in this range is attributed to Glu-PEI complexes. The size of complexes in S4 is smaller that that in S5, which may be attributed to the higher PEI content or more hydrated structure existence in S5.

The existence of complexes in sample S4 was also proven by AFM. Sample S4 was dipped on the Si wafer, and the scanning was directly performed in the solution (Fig. 4.2.3). The height of complexes from AFM is ~1.5-2.1 nm, supposing that complexes on the surface are spherical in morphology. According to the result from SAXS, the complex diameter is 1.88 nm, according to the equation $\mathcal{A}_{sphere} = \ * R_g \sqrt{(5/3)}$. Thus, the diameter of the complexes from SAXS is 1.88 nm, which is within the range of the AFM results. In addition to isolated complexes, the necklace-like complexes assemblies and aggregates of hundreds of nanometers in size are observed. The height of the necklace-like complexes is the same as that of the isolated complexes, which means that necklace-like structures are assemblies of isolated spherical complexes. More SAXS data analyses are needed to clarify the interactions between complexes in the necklace-like structures.

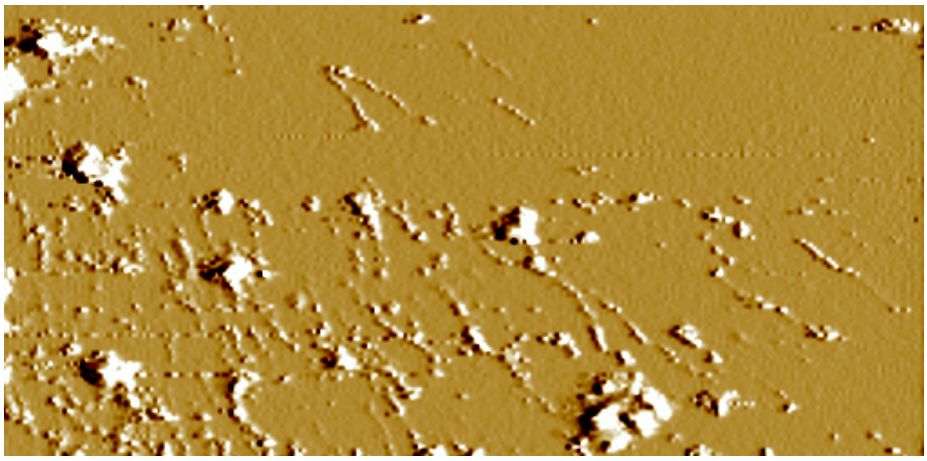

Fig. 4.2.3. AFM result from Sample S4. The length of the image is 10 μm.

ξ-potential measurements were performed to indicate the stability of complexes in solution. The ξ-potentials in S4 and S5 are +13 and +5 mv, respectively. The results indicate that the complexes in S4 are incipiently unstable, whilst those in S5 are flocculated. The aggregates and necklace-like assemblies in the AFM image in Fig. 4.2.3 may result from the incipient instability of S4. The weakly and positively charged complexes suggest that Glu may stay inner, and the positive charges are contributed from amine groups on PEI.

4.2.3 Discussion

The pH value controls the interactions between Glu and PEI. Glu is a zwitter-ion, carrying two carboxyl groups and one amine group. Its isoelectric point is at 3.2 and has three pKa values at 2.2 (α-COOH), 4.3 (γ-COOH) and 9.7 ($-NH_2$). The branched PEI is a polybase, containing primary, secondary, and tertiary amine groups with the number ratio ~1:2:1. PEI is miscible with water, and the pH value of PEI aqueous solution is ~10. Therefore, Glu and PEI are oppositely charged, and they can interact with each other by electrostatic interactions between the primary and secondary amine groups on PEI and carboxyl acid groups on Glu in a wide pH range between ~3 and ~10. Hydrogen bonding and hydrophobic interactions are becoming more important when the pH value is below ~3, where Glu carries weakly positive charges. In short, the titration results suggest that, when the values of **φ** is between 5/1 and 3/1, interactions between Glu and PEI are

partially electrostatic in nature, including hydrogen bonding and repulsive hydrophobic interactions.

By combining results from AFM, SAXS, and ξ-potential, the existence and interactions between Glu and PEI in solution are elucidated, generating important quantitative information regarding the stability of Glu-PEI complexes. The existence of Glu-PEI complexes are independently investigated by SAXS and AFM, separately. In addition, the size of complexes is determined by both methods, which corresponds to each other very well. AFM provides more information of the state of complexes. They can stay as isolated or as necklace-like structures or aggregate into structures hundreds of nanometers in size. The ξ-potential results show that ξ-potential is ~+10 mv, which indicates that Glu-PEI complexes are floc in nature, and can reversibly aggregate and dissociate. Therefore, ξ-potential explains well the existence of necklace-like structures and aggregates in AFM. Furthermore, interactions between Glu-PEI complexes within a necklace-like structure can be distinguished by carefully analyzing SAXS data and measuring a series of samples with different concentrations.

More structural and compositional details of Glu-PEI complexes are still needed for the understanding of Glu-PEI complexes. For example, the chemical environments of Glu and PEI in Glu-PEI complexes need to be solved. The state of Glu molecules in complexes needs to be clarified. One possibility is applying contrast matching in SANS measurements. A series of contrast matching measurements have been performed to match Glu or PEI, respectively. The data analysis is still underway. In addition, Glu-PEI complexes in $\boldsymbol{\varphi}$ at 1/1, 5/1, and 9/1 can be compared to indicate the Glu distribution between as being isolated and as complexes. The complex structures can be related to the phase separation, i.e. precipitation or coacervation after the solution is mixed with EtOH.

5. Amino Acids Precipitations

Abstract

The work presented herein is designed to understand DL-Glutamic acid (Glu) precipitation with polyethyleneimine (PEI) as an additive as a sequential process: 1) the formation, growth, and coalescence of polymer-induced liquid precursor (PILP); 2) the nucleation of nanostructures within PILP droplets; 3) nanostructure self-organization into hierarchical structures. Precipitation occurs as a result of mixing the Glu-PEI aqueous solution with a non-solvent – EtOH. Considering the rapid formation and transformation of potentially small precursor phases during the precipitation process, small-angle x-ray scattering (SAXS) and stopped flow techniques are combined for monitoring the very early stage of phase separation, and the phase behavior of PILP is investigated by using SAXS and small-angle neutron scattering. Microscopic techniques aid clarification of the final microspheres, which presents Maltese-cross extinction patterns between the crossed polarizers as a result of the highly ordered radial nanoplatelet arrangement. The impact of other experimental parameters such as temperature, pH, and amino acid/polyelectrolyte ratio is also investigated for the Glu morphogenesis process. This model system for understanding molecular crystallization from PILP precursors as a multi-step process is then extended to the precipitation of other amino acids, bearing an opposite charge to the polyelectrolyte additives.

* The SANS measurements were performed with Dr. Vitaliy Pipich at Outstation at FRM II, Garching, Munich. The SAXS measurements were performed by Dr. Peter Cernoch from MPIKG at Grenoble, France. In addition, he helped to get the data by extracting the raw data from SANS & SAXS.

5.1 The Mechanism of Organic PILP Multi-step Transformation

5.1.1 Introduction

Generally, bioinspired crystallizations are multi-step processes. The precursor phases start to form and transform into nanostructures, followed by nanostructure self-assembly and self-organization at various scales thereafter.[11, 12] To detect the mechanism of bioinspired crystallizations is helpful for understanding biomineralization and for designing functional materials with unique properties. Polymer-controlled crystallization can be treated as a biomimetic process, where charged polymers mimic the roles of soluble biomacromolecules in biomineralization. The amorphous phase has been proved as a precursor in biomineralization[76] and biomimetic crystallization.[77] The concept of "polymer-induced liquid precursor" (PILP) was put forward by Gower *et al*,[17] and later on was suggested to be a possible precursor phase for the amorphous phase.[78] Therefore, it is interesting to understand the PILP details, including its structure, composition, and its role during a multi-step phase transformation following the Ostwald rules of stages. The main difficulties in detecting possible precursors in crystallization are their fast transformation rate and low concentration of precursors.

Small angle scattering can conveniently provide fruitful static and dynamic phase information on the nanometer and submicrometer scale. In the crystallization field, it has been used for precursor detection, and has been providing strong supports for non-classical crystallization. For example, Schwahn *et al.* reported the existence of a mesocrystalline phase during the formation of single crystalline alanine by using small angle neutron scattering (SANS).[79] In another case, the crystallization of $CaCO_3$ with egg-white protein ovalbumin was detected to pass through a sequence of an amorphous phase and polymorphs before obtaining the thermodynamically stable polymorph – calcite.[80] Small angle scattering is a good candidate to provide the information of PILP phase transformation on the proper time and length scale.

Wohlrab *et al.* extended the PILP route to organic systems.[56] The relatively large size and low lattice energy of organic molecules may slow down the timescale of the PILP phase formation and transformation for time-resolved scanning, compared to that of inorganic counterparts. However, the existence of the metastable organic PILP and its

transformation into final products are insufficiently known. Herein, the PILP transformation via a multi-step growth and coalescence is investigated with small angle scatterings. Stopped flow is combined with small-angle neutron scattering (SANS) & small angle x-ray scattering (SAXS) to guarantee the immediate formation of a homogeneous mixture. This research provides fruitful information of the mechanism of precipitations via PILP routes. The PILP formation is too fast to detect in the system presented here.

5.1.2 Results

The result section can be divided into two parts. The first part is focused on SANS results. The data was collected in every second, and the growth & coalescence of PILP droplets was observed during 260 sec. The second part introduces SAXS results, which provides the information of PILP fast transformation during the first 2 sec.

SANS in Glu-PEI-D_2O-CD_3OD System

A series of preparative experiments were performed by using common chemicals instead of deuterated ones to find the optimized parameters for SANS measurements. The Glu-PEI-water-EtOH mixture was turbid by mixing a Glu-PEI aqueous solution with EtOH. The turbidity continued to get weaker by increasing the temperature, which suggests that the system has an upper critical solution temperature. However, the temperature of phase separation is higher than the boiling point of the quaternary mixture by using saturated Glu-PEI aqueous solution. The first plan by decreasing the solute concentration in the Glu-PEI aqueous solution only resulted in very weak signals in SANS. The phase separation temperature can also be decreased by replacing EtOH with MeOH, because the polarity of MeOH is closer to water than that of EtOH. Therefore, by keeping Glu/PEI (w/w; **φ**) at 5/1 and the volume ratio of MeOH and aqueous solution (**λ'**) at 8.6, the phase separation temperature of a quaternary mixture by using sample x0.5 ([Glu] = 12.5 $g \cdot L^{-1}$, [PEI] = 2.5 $g \cdot L^{-1}$, water) was determined to be 40°C. Another two mixtures of sample x0.5 and MeOH with **λ'** values at 6 and 15, respectively, were used as a comparison. In SANS measurements, the solvents were replaced with deuterated ones. However, temperature drop methods were discarded because phase separation occurred

faster than the temperature drop velocity by using the thermostat. Therefore, the measurements were switched to fast mixing.

The fast mixing measurements were performed by mixing the deuterated Glu-PEI aqueous solution with CD_3OD by a stopped flow equipment. The relationship between the concentration of Glu-PEI aqueous solution and the count rate was examined. Sample x2.0 ([Glu] = 50 $g \cdot L^{-1}$ and [PEI] = 10 $g \cdot L^{-1}$, D_2O) was chosen because the scattering intensity was three times increased compared to that in sample x1.0 ([Glu] = 25 $g \cdot L^{-1}$ and [PEI] = 5 $g \cdot L^{-1}$, D_2O) (Fig. 5.1.1A). Mixtures were prepared at various temperatures at 35, 20, 10, and 5°C to check the signal strength. The signal strength was growing by decreasing the temperature, as summarized in Fig. 5.1.1B. However, crystallization had happened within sample x2.0 at 5°C before it was mixed with CD_3OD. Therefore, 10°C was chosen for the following experiments.

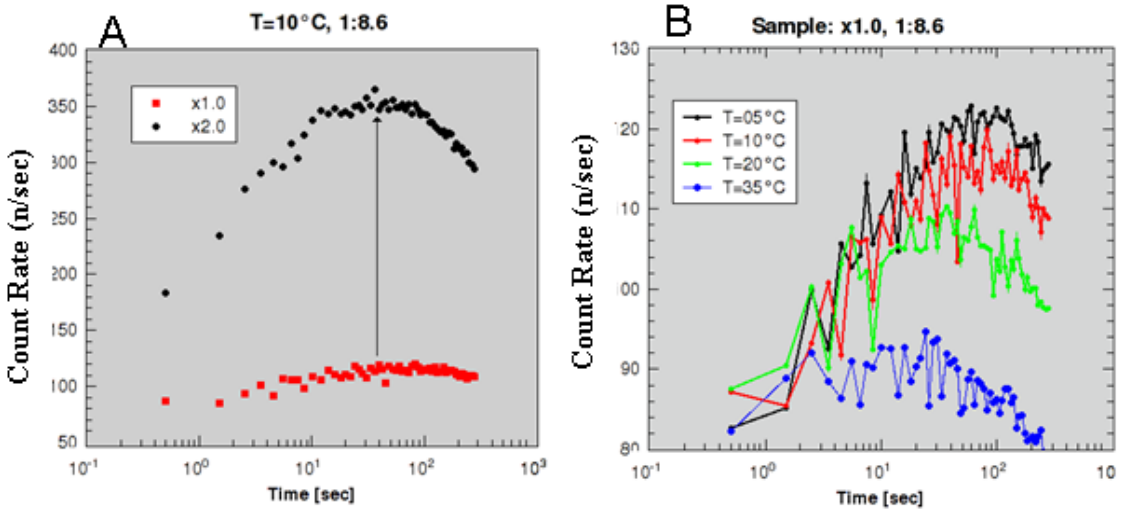

Fig. 5.1.1. Image **A** shows how the count rates rises by increasing the concentration of aqueous solution in SANS measurements (the concentration in the mixture was doubled in the black curve compared to that in the red line); image **B** shows the relationship between the count rates and the mixing temperature, where different temperature is shown in different colors.

Frame beaning was used to improve the statistics because the count rate in the diluted mixture was too low to get good signals. Firstly, the measurements were repeated for five times. For example, the black curve in Fig. 5.1.2 A is the sum of five curves. Next, the statistics was achieved by beaning frames with progressive steps and the number of frames was reduced from 300 to 56 thereafter. The fluctuation in the blue curve was much lower than that in the black curve, as shown in Fig. 5.1.2 A.

Finally, the Q range was optimized by applying neutron beams with three wavelengths at 5, 12, and 19 Å (Fig. 5.1.2B). By using 5Å neutrons, the count rate began to decrease only at ~35 sec, which means that the scanning time is too limited for data analysis. As a comparison, the count rate only began to decrease after 260 sec with 12 Å neutrons. As to the 19 Å neutrons, the count rate increased until ~1000 sec. However, a longer wavelength brings simultaneously a lower count rate. Therefore, 12Å neutron was chosen as the optimal wavelength for standard SANS measurements.

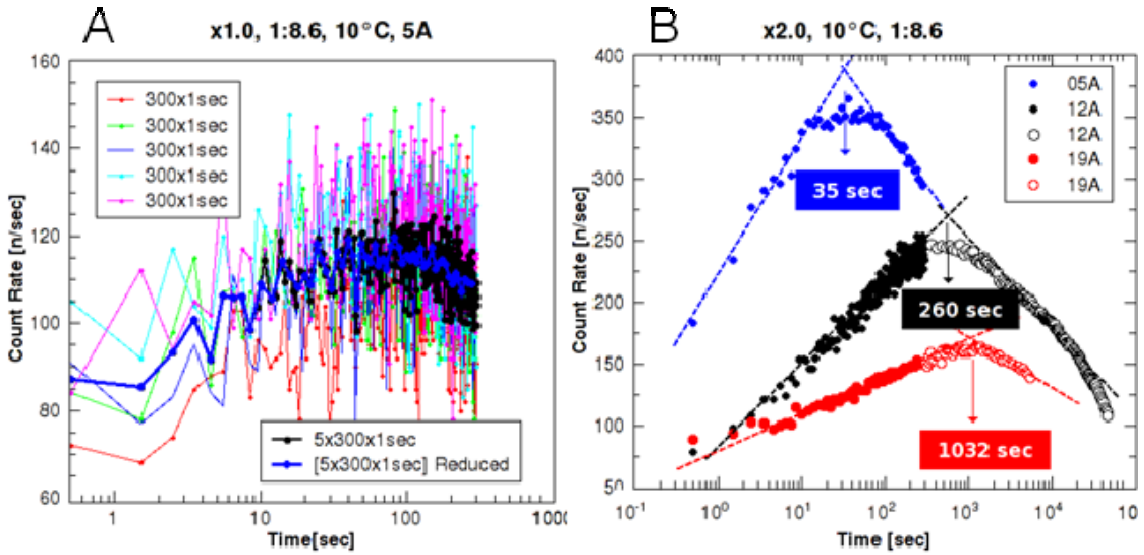

Fig. 5.1.2. Image **A** shows the relationships between the statistics and frame beaning in the SANS measurements. The bold black curve (partially hidden under the blue curve) is the sum of five colorful curves, and the bold blue curve is the beaned frame. The data were collected per second. Image **B** shows how the count rates change with neutron wavelengths.

With the above optimized parameters, sample x2.0 was mixed with CD_3OD by using three **λ'** values at 6, 8.6, and 15, respectively. By analyzing the curve I(Q) – Q (not shown), there is a relationship $I(Q) \sim Q^{-4}$, indicating the existence of objects with a sharp surface. Then, results were found to fit the spherical objects by using a 3D Beaucage model, and the equation is written as follows:

$$I(q) = I(0)\exp(-R_g^2 q^2/3) + P_\alpha \{ \mathrm{erf}[(R_g q)/\sqrt{6}]^3 / q \}^\alpha$$

Three parameters, including the radius of gyration R_g, the forward scattering intensity I(0), and the Porod constant P_4 can be derived from the above equation. Their relations with time are summarized in Fig. 5.1.3. Fig. 5.1.3A indicates that the size of

PILP droplets grows from ~30 nm to ~100 nm during the first ~260 sec. In addition, three curves share the same growth mode of R_g with time: $R_g \sim t^{0.24}$. Furthermore, the values of R_g in three mixtures are different with the order $R_{g,6} > R_{g,8.6} > R_{g,15}$ at the same moment. The differences in size can be attributed to the polarity of the mixture. The **λ'** = 6 mixture with a lower polarity can induce fewer PILP droplets with larger sizes compared with the other two mixtures. The value of I(0) also increases following the equation $I(0) \sim t^{0.76}$ (Fig. 5.1.3B) in each sample. According to its definition, I(0) is proportional to the volume fraction of the PILP phase and the scattering contrast between PILP and supernatant. Supposing that the scattering contrast is constant during the measuring time, the increase of I(0) can be treated as the growth of each PILP droplet.

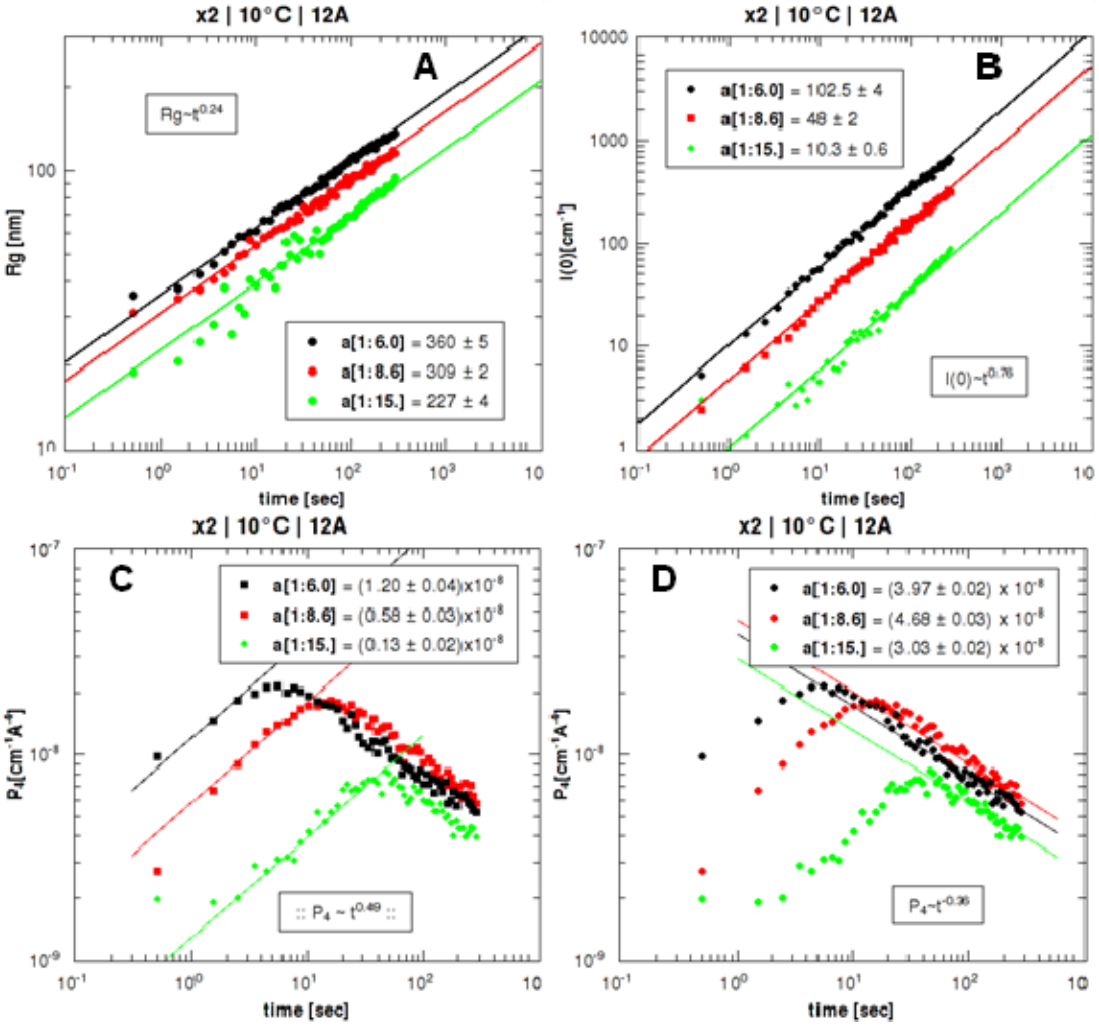

Fig. 5.1.3. The changes of R_g, I(0), and P_4 with time in ~260 sec in the SANS measurements. The values of **a** in each figure are the prefactors in the 3D Beaucage equations.

P_4 shows a different tendency from the exponential growth of R_g and I(0). It starts with an exponential growth, before shrinking exponentially in three curves. The increase and decrease with time can be summarized as $P_4 \sim t^{0.49}$ and $P_4 \sim t^{-0.36}$ (Fig. 5.1.3C-D), respectively. The transition time is different for each sample. The transition time is ~8 sec for the mixture at **λ'** = 6, whilst it takes ~50 sec for the P_4 value in the mixture at **λ'** = 15 to decrease. As P_4 is proportional to the volume fraction, the ratio of surface area to volume, and the scattering contrast of the particle, the growth of P_4 can be attributed to the growth of each PILP droplet, whilst its decrease results from the coalescence among PILP droplets.

Small Angle X-ray Scattering Experiments in Glu–PEI–Water–Alcohol Systems

SAXS was applied to provide the fast kinetics information of possible PILP formation and transformation during the first 2 sec. The quaternary systems are Glu-PEI-water-MeOH/EtOH. The results by mixing sample x1.0 with MeOH with **λ'** at 6, 8.6, or 15 are summarized in Fig. 5.1.4. Data in **λ'** = 15 mixture show some difference from the other two series of data and are left for further data analysis.

There exists a relationship I (Q) ~Q^{-4}, which suggests the existence of objects with a sharp surface from the first data collection. The changes of R_g, I(0), and P_4 with time are analyzed by using the **λ'** = 8.6 mixture as an example thereafter. The general trend is that PILP droplets grow during the measuring period (0–2 sec) (Fig. 5.1.4A). They continue to grow until ~0.4 sec before the size leaps from ~35 nm to ~40 nm. After the jump, the growth rate of PILP droplets slows down, which is judged from the slope of the curve (Fig. 5.1.4A). The gap is also observable in the **λ'** = 6 mixture at the same moment. However, the size value in the **λ'** = 8.6 is smaller than that in the **λ'** = 6 mixture. The reason has been explained in the SANS section. The polarity of the **λ'** = 8.6 mixture is higher than that in the **λ'** = 6 mixture. The higher polarity results in PILP droplets smaller in size but larger in number density. The size of PILP droplets in SAXS measurements is larger than that in SANS measurements. For example, the PILP size in SAXS measurement is ~40–45 nm by using **λ'** = 8.6 mixture at 1 sec. However, the size at the same moment in SANS measurement is ~30–40 nm. The reason is that the concentration

in SANS measurements is doubled compared to that in SAXS measurements. The more concentrated solution can cause PILP droplets larger in number but smaller in size.

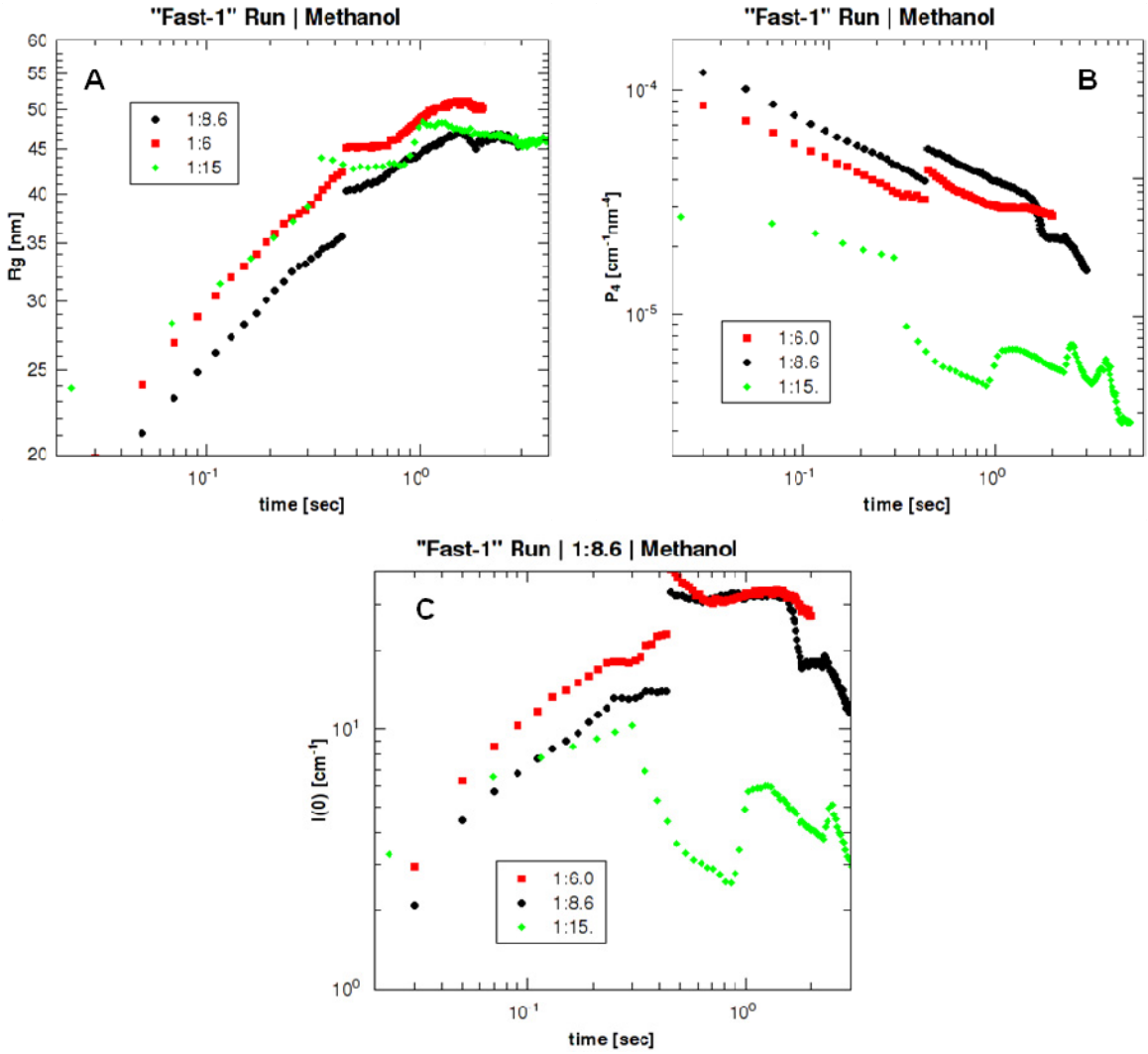

Fig. 5.1.4. The changes of R_g, I(0), and P_4 with time in SAXS measurements. Sample x1.0 is used, and the values of **λ'** are 6, 8.6, and 15, respectively.

The values of I(0) by using **λ'** = 8.6 and **λ'** = 6 mixtures increase till 0.4 sec. Then, they leap to a higher value and keep constant until 2 sec (Fig. 5.1.4B). As to the P_4 values, they decrease during the first 2 sec, which is contradictory to the P_4 increase in SANS measurements (Fig 5.1.3C–D). The decrease of P_4 by using sample x1.0 suggests the coalescence of PILP droplets. PILP droplets formed are polydisperse in size distribution (Image not shown).

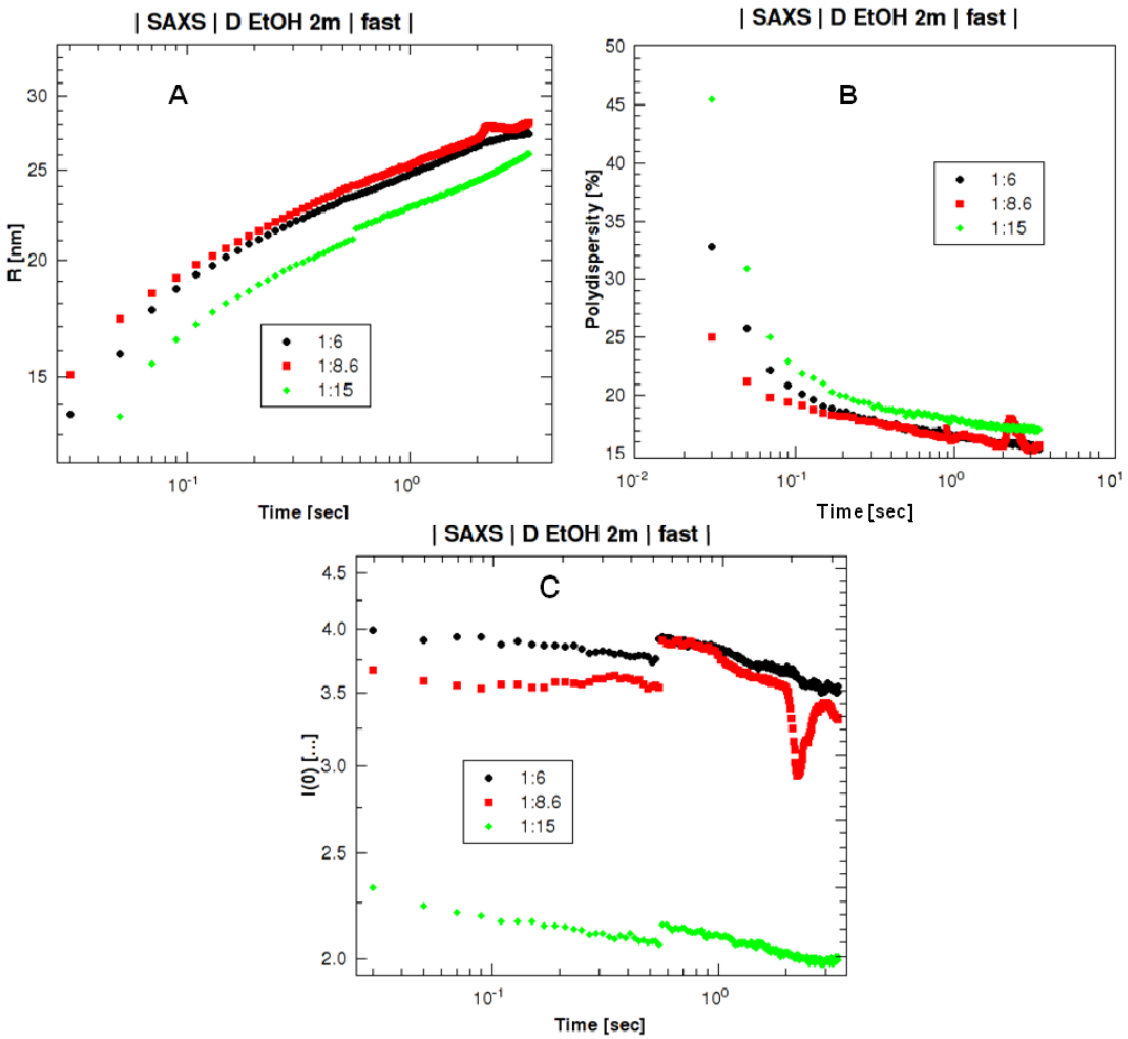

Fig. 5.1.5. The changes of R_g, I(0), and polydispersity with time in SAXS measurements. Sample y1.0 is used, and the values of **λ''** are 6, 8.6 and 15, respectively.

MeOH was replaced by EtOH for the fast kinetic research by using sample y1.0 ([Glu] = 25 g·L^{-1} and [PEI] = 2.5 g·L^{-1}, H_2O). Three values of **λ''** (defined as EtOH/aqueous solution v/v) are constant at 6, 8.6 and 15. The results are summarized in Fig. 5.1.5. The values of R_g increase during the measuring period for three mixtures from Fig. 5.1.5A. The values of R_g in both mixtures are close to each other. I(0) values in the **λ''** = 8.6 and **λ''** = 6 mixtures are constant before the values leap between ~0.5-0.6 sec (Fig. 5.1.5C). The polydispersity in each mixture decreases with time, suggesting that PILP droplets are getting monodisperse in size distribution.

Comments

Some preliminary data herein need further explanation. For example, the result by using **λ' or λ''** = 15 mixture shows different trends (Fig. 5.1.4 and Fig. 5.1.5C) or values (Fig. 5.1.5A-B) from that by using the **λ' or λ''** = 8.6 and **λ' or λ''** = 6 mixtures. In addition, the gaps in SAXS data need further analysis to exclude the possibility that they might be induced by the machine instead of phase behavior. Furthermore, the contradiction between the decrease of P_4 in SAXS measurements and the increase of P_4 in SANS measurements during the first 2 sec needs to be clarified. Considering the long application time for SANS and synchrotron SAXS, the measurements are still incomplete, but it was not possible to complete them within this thesis.

5.1.3 Discussion

The quenching of Glu-PEI aqueous solution with alcohol can result in Glu precipitation via a metastable L-L phase separation. The formation of the PILP phase is a fast process, and it happens before the first data collection at ~0.02 sec. Therefore, whether the phase separation is passing through a spinodal or binodal decomposition, it is too fast to capture in the current system. The results herein are mainly focused on the multi-step PILP transformation. During the first ~260 sec, the initially formed PILP droplets pass through multi-step coalescent and grow processes before the size reaches ~100 nm. PILP droplets can grow further and those formed thereafter can act as matrices for the nucleation and growth of nanoplatelets later on.

PILP droplets are comparable to the initially formed liquid-like $CaCO_3$-PAA precipitates.[15] Such liquid-like $CaCO_3$-PAA precipitates (collected after reacting for ~100 ms) are observable with cryo-TEM technique, which can grow and coalescent into spherical amorphous-like nanostructures. Both pieces of research support the notion that crystallizations with additives are multi-step processes, and PILP droplets can grow by Ostwald ripening and coalescence processes before the crystalline structure is formed within the PILP droplets.

5.2 Hierarchical Glutamic Acid Microspheres

5.2.1 Introduction

Biominerals are hierarchical structures with nanostructures as building blocks.[27] A variety of inorganic materials have been applied as model systems to understand the mechanism of biomineralization and bioinspired crystallizations.[11, 12] Crystallization of organics can also be suitable model systems. Organic crystals have lower lattice energy, and exhibit a larger variety of possibilities for molecular recognition, because the building blocks for organics are large molecules instead of small ions in inorganic counterparts. Therefore, organics can be better influenced by additives, resulting in a variety of polymorphs. The ultimate goal of crystallization of organics is similar to their inorganic counterparts, which is to control the nanoparticle (NP) size, morphology, orientation, polymorph, and importantly, the NP self-assembly, self-organization or recrystallization into bulk crystals.

The Nakanishi group pioneered the reprecipitation method for the preparation of organic NP dispersions.[81] The organic NPs precipitate by adding a miscible non-solvent into the mother liquor. However, as-prepared NPs are colloidally stable only for a short period. Without a stabilizer, NPs grow up into microscale by an Ostwald ripening process. On the other hand, organic NPs can aggregate into hierarchical micro to macro-structures with the existence of stabilizers, including surfactants,[82] polyelectrolytes,[56] dendrimers,[83] double hydrophilic block copolymers,[57, 84, 85] and surfactant-polyelectrolyte mixtures.[86] NPs can aggregate into mesoscopically structured single crystals with crystallographic orientations, namely “mesocrystal”. The aggregation of NPs can also pass through a fast self-organization process without showing mutual crystallographic orientations.[25]

In this section, the preparation of DL-Glu (Glu) macroporous microspheres with polyethyleneimine (PEI) as an additive is systematically investigated by tuning a variety of parameters such as Glu/PEI (w/w; **φ**) , non-solvent, the volume ratio of a non-solvent–EtOH and aqueous solution (**λ’’**), the molecular weight of PEI, temperature, and pH value. Then, the method is extended to L- and D-Glu microsphere preparation. This is a model system to understand how macroporous organic microspheres are prepared from nanostructure self-organization via a bioinspired precipitation route.

5.2.2 Results

It is known that Glu crystallizes directly into sheet-like precipitates by mixing the mother liquor with EtOH (Fig. 1.1A). However, adding a small amount of PEI into Glu aqueous solution can result in the mixture of two morphologies after the precipitation, namely reference crystals and microspheres (Fig. 5.2.1A). Since microspheres are the only product attributed from the existence of PEI, various parameters were tested to optimize the procedure of their preparation. The standard system investigated is a quaternary Glu-PEI-water-EtOH one (**λ''** = 9). The influence of important parameters such as **φ**, [Glu], pH value, and temperature will be discussed in the following paragraphs.

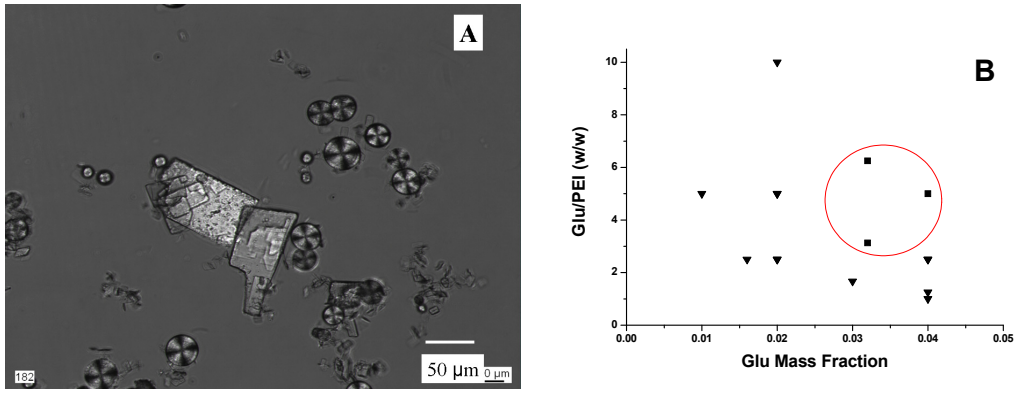

Fig. 5.2.1. Fig. **A** is a representative image, showing the mixture of reference crystals and microspheres; Fig. **B** is a binary phase diagram, indicating how the value of **φ** and Glu mass fraction in Glu-PEI solution affect the purity of microspheres. The compositions for the preparation of pure microspheres (■) are wrapped with the red circle; other compositions correspond to the mixture of reference crystals and microspheres (▼).

A series of experiments were performed by mixing a Glu-PEI aqueous solution (water as solvent) with EtOH at 60°C, and the results are summarized in Fig. 5.2.1B. Pure microspheres were prepared when the values of **φ** are between 10/1 and 20/1; otherwise, a mixture of microspheres and reference crystals were obtained. Pure microspheres were preferentially prepared by using nearly saturated or supersaturated Glu-PEI aqueous solution (Fig. 5.2.1B), which is also advantageous for obtaining a large quantity of microspheres. The mixing temperature was chosen at 60ºC instead of at R.T. to increase the solubility of Glu.

Compared to temperature rise, altering the pH value from the isoelectric point of Glu at 3.2 is a more effective way to increase Glu solubility. A series of experiments were

performed by using 0.5 M H_2SO_4 aqueous solution (pH value is ~0.5) as a solvent at 60°C. The results are summarized in Table 5.2.1. Pure microspheres can be prepared in a wide Glu mass fraction range (i.e. up to 0.2) and in a relatively high **φ** range (i.e. up to 70/1). By using acidic aqueous solutions, pure microspheres were also prepared at R.T, as summarized in Table 5.2.2.

The polarity of solvent is a key parameter to control the driving force of precipitation. It can be tuned by changing the alkaline groups of the alcohol or the value of **λ''**. Firstly, *i*-propanol and *n*-propanol were used for microsphere preparation, only obtaining reference single crystals. MeOH can produce pure microspheres but only in a small quantity. The reason is that the driving force of Glu precipitation with MeOH is not as strong as that by using EtOH, since the polarity of MeOH is closer to that of water compared to EtOH. Then, various **λ''** values at 5, 7, 9, and 11 were tested for the preparation of microspheres. Pure microspheres were obtainable when the **λ''** value was at 11 and 9; otherwise, a mixture of microspheres and reference crystals were obtained. Thus, **λ''** was kept at 9 in the following experiments.

Table 5.2.1 Recipes for the preparation of microspheres under acidic conditions at 60°C

	Glu wt%	**PEI wt%**
6-1	3,2	0,16
6-2	10	0,6
6-3	10	1
6-4[a]	14	0,2
6-5	14	0,6
6-6	14	1
6-7[a]	18	1
6-8[a]	20	1

[a] some insoluble crystals in the aqueous solution

In addition, the molecular weight (Mw) of PEI was found to have no affect on the microsphere preparation by using PEI with various Mw at 800, 1300, 2,000, and 750,000, respectively. The result implies that the charge density of the polyelectrolyte is important for the preparation of microspheres instead of chain length. Furthermore, quiescent condition was preferred for the preparation of microspheres instead of using stirring.

Otherwise, glue-like structures were formed adhering to the vessel. Also, the complex formation between Glu and PEI in aqueous solution is the prerequisite for the formation of microspheres. A control experiment was performed by mixing a Glu solution with a mixture of PEI and EtOH, only obtaining reference crystals.

Table 5.2.2 Recipes for the preparation of microspheres under acidic conditions at R.T.

	Glu wt%	PEI wt%
7-1[a]	14	0.2
7-2[a]	14	0.6
7-3[a]	14	1
7-4[a]	18	1

[a] some insoluble crystals in the aqueous solution

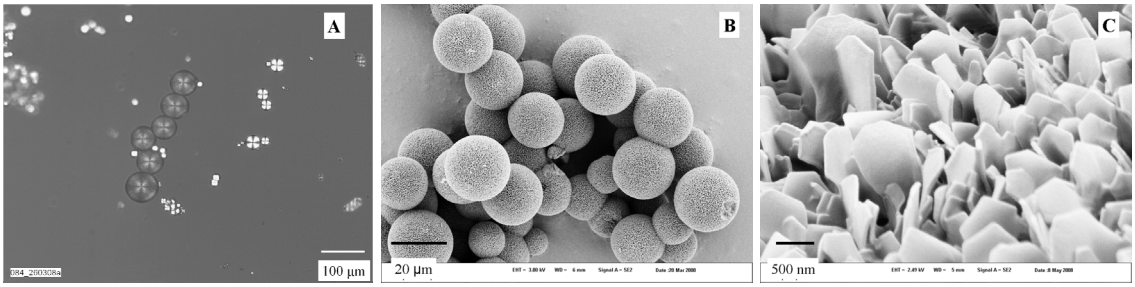

Fig. 5.2.2. Images **A** and **B** are POM and SEM images of Glu microspheres, respectively. Image **C** is a SEM image of the surface of a microsphere.

Fig. 5.2.2 provides structural details of microspheres. The as-prepared microspheres show a clear Maltese-cross extinction pattern between the crossed polarizers (Fig. 5.2.2A), which suggests the existence of lamellar nanostructure assembly in a radial orientation. However, when samples were air-dried or redispersed in EtOH, only weakly birefringent patches could be observed (image is not shown). This phenomenon indicates that the dehydration of microspheres causes a permanent disruption of the ordered structure. The size of microspheres is polydisperse from several micrometers to ~100 μm. Fig. 5.2.2B-C are representative SEM images. Fig. 5.2.2B is an overview image of the microspheres, which are 7-20 μm in size (Glu wt% = 3.2, PEI wt% = 0.16, **λ''** = 9, 60°C, water). Fig. 5.2.2C shows that the surface of microspheres is porous, and the porosity comes from the gaps between nanoplatelets (Glu wt% = 4, PEI wt% = 0.2, **λ** = 9, 60°C, water). Nanoplatelets are ~200-1000 nm in width, and are radially oriented.Glu microspheres prepared by using acidic Glu-PEI solutions show a different morphology

from those by using neutral Glu-PEI solutions. Microspheres under acidic conditions are from ~2-10 μm in diameter. Fig. 5.2.3A shows that a microsphere is composed of twisted nanoplatelets as large as 1 μm. In addition, microspheres prepared under acidic conditions show porosity as high as 17 $m^2 \cdot g^{-1}$ compared to the value at 2.5 $m^2 \cdot g^{-1}$ from those under neutral conditions in BET measurements. On the other hand, increasing the pH value to a basic range is harmful for the preparation of microspheres, only obtaining reference crystals (Fig. 5.2.3B).

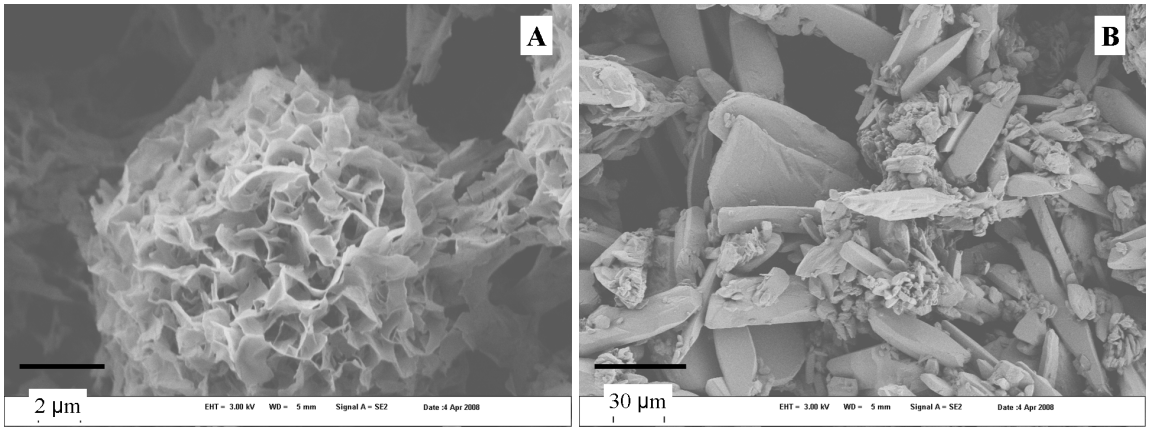

Fig. 5.2.3. Image **A** is a SEM image of sample **6-3**. Image **B** shows the crystals obtained using basic aqueous solution (Glu wt% = 10, PEI wt% = 1, **λ''** = 9, R.T, 0.1M NaOH).

Two methods were applied to clarify the inner structure of microspheres. In the first route, the microspheres were grinded into small pieces. Fig. 5.2.4A-B show that microspheres are solid with nanoplatelets being arranged in a radial way, corresponding well with the results in Fig. 5.2.2C. Microspheres were also embedded into epoxy to obtain microtome sections. The cross-sectional image from Fig. 5.2.4C shows that nanoplatelets are vertical to the cut area, which again suggests that all nanoplatelets are radially oriented. A closer scan reveals that the thickness of the nanoplatelets is ~40-50 nm (Fig. 5.2.4D).

In addition to the isolated microspheres, superstructures of microspheres were formed. The SEM image shows that the sheet-like superstructures are microsphere monolayers, where microspheres are densely packed within the monolayer (Fig. 5.2.5A; Glu wt% = 3.2, PEI wt% = 0.32, **λ''** = 9, 60°C, water). The sheet-like superstructures are formed along the wall of vessel. Microspheres prepared by using an acidic Glu-PEI solution form superstructures in another way. A microsphere superstructure ~50 μm in

diameter is composed of small microspheres ~5μm in size as building blocks (Fig. 5.2.5B; sample **6-4**).

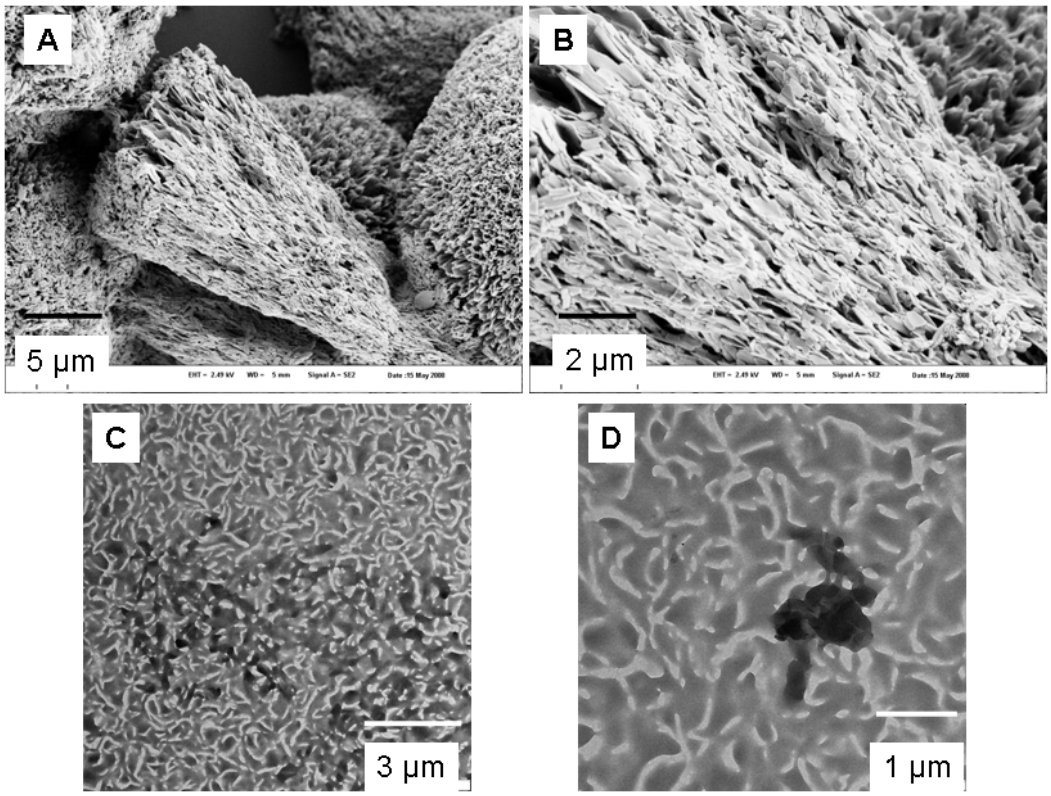

Fig. 5.2.4. Images **A**-**B** are SEM images, showing the inner structure of a broken microsphere (Glu wt% = 4, PEI wt% = 0.2, **λ''** = 9, 60°C, water). Images **C**-**D** are TEM images of the same sample**,** indicating the microtome sections of a microsphere.

WAXS results indicate that microspheres show the same crystallographic structure (Fig. 5.2.6A) as reference crystals (Fig. 5.2.6B). Both show a conglomerate structure, and all peaks attribute to a thermodynamically stable polymorph β-L-Glu. However, the intensities of some peaks in microspheres are different from those in the reference crystals. For example, the intensities of both (040) and (020) peaks are suppressed in the microspheres, compared to those in the reference crystals. The reason for the intensity suppression is that both directions exist only on the nanoscale. In addition, microspheres prepared by using acidic or neutral Glu-PEI solution show the same WAXS pattern (image not shown).

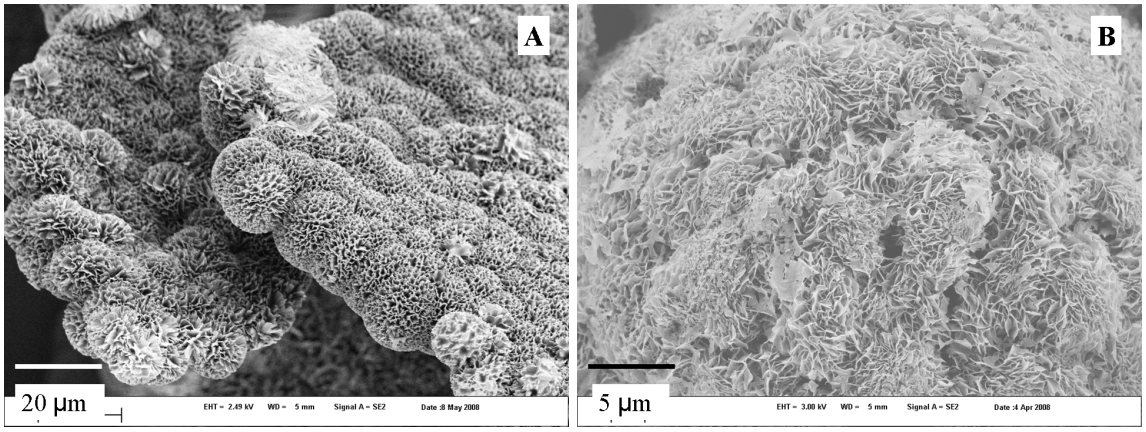

Fig. 5.2.5 shows SEM images of superstructures with microspheres as building blocks by using neutral (**A**) and acidic (**B**) solutions.

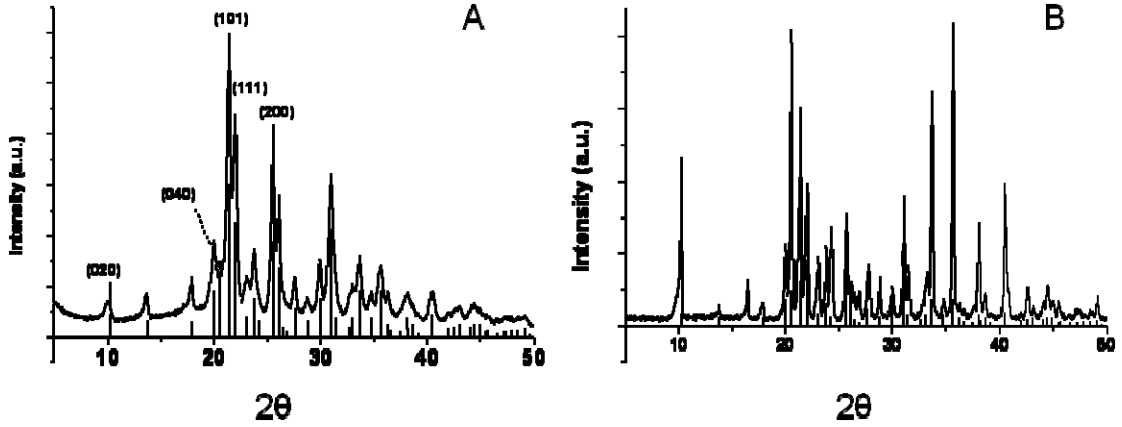

Fig. 5.2.6. Image **A** is WAXS patterns of microspheres (Glu wt% = 3.2, PEI wt% = 0.16, **λ''** = 9, 60°C, water). Image **B** is the WAXS data of reference crystals.

Since Glu shows a conglomerate structure, a similar recipe was extended for the preparation of L- or D-Glu microspheres. Fig. 5.2.7A-B show L- and D-Glu microspheres prepared by using neutral Glu-PEI solution and EtOH. The microspheres are between 10 and 20 μm in size, and all nanoplatelets show the same radial orientation as that shown in DL-Glu microspheres.

L-Glu microspheres were used as the column fillers in a HPLC system for chiral separation uses. Several achiral mixtures, DL-Binaphthol, DL-Phenylethanol, and DL-Propranolol were tried as the fluid phases. However, there was no chiral separation effect observed at all because of several possible reasons. First, the microspheres used are tens of micrometers in diameter and are polydisperse in their size distribution, which can cause the big gaps between microspheres. The solution can then flow freely without interacting with L-Glu thoroughly. Second, chiral separation always follows "the four

point interactions", which means that a chiral tetrahedral receptor needs at least four functional groups to interact effectively with a chiral tetrahedral solute of similar dimensions on the molecular level.[87] Current microspheres are not qualified to this standard yet. For future application in chiral separation, microspheres have to be prepared micrometer or submicrometer in size. More interacting points on chiral microspheres then need to be introduced. Both improvements can increase the interactions between the column and fluid phase, and can possibly induce chiral separation.

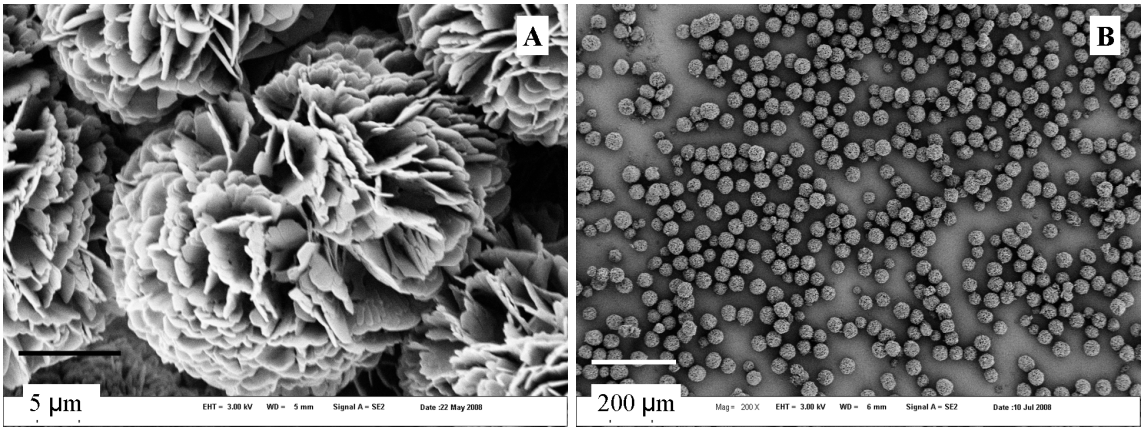

Fig. 5.2.7. Images **A** and **B** are SEM images of L- and D-Glu microspheres, respectively. (L- or D-Glu wt% = 3.2, PEI wt% = 0.16, **λ''** = 9, 60°C, water).

5.2.3 Discussion

Amino acids are zwitterions, and altering the pH value of their aqueous solution is an important way to produce amino acids into various polymorphs and morphologies.[84, 88] In addition, the pH value is also a key parameter for controlling the interactions between Glu and PEI in a Glu-PEI aqueous solution. The pH values of the saturated Glu-PEI aqueous solution (**φ** = 10/1) with water and 0.5M H_2SO_4 as a solvent are 3.6 and 0.5, respectively. In both cases, carboxylic acid groups on Glu are at least partially protonated, and Glu and PEI interact with each other via electrostatic interactions, intermolecular hydrogen bonds, and hydrophobic interactions.

Pure microspheres can be prepared in a range of **φ** values. When **φ** is lower than 10/1, the driving force for Glu precipitation is not strong because a certain amount of Glu molecules can be trapped in the thermodynamically stable Glu-PEI complexes. Therefore, the precipitation is incomplete. On the other hand, only a small amount of Glu molecules

forms Glu-PEI complexes in Glu-PEI aqueous solutions. When the above solution is mixed with EtOH, nucleation happens within the PILP droplets as well as in the bulk phase. Those particles nucleated from the bulk phase grow up into reference crystals. Therefore, **φ** value has to be controlled precisely to assure that all nucleation happens within PILP droplets.

The PILP route changes the kinetics of Glu precipitation. The mixture of Glu-PEI aqueous solution and EtOH immediately turns turbid. As a comparison, there is no turbidity in the precipitation of Glu reference crystals. Passing through metastable PILP droplets, the nucleation barrier is highly decreased, which results in the acceleration of the nucleation rate. The acceleration of nucleation via a metastable L-L phase separation process is suggested to play a key role in protein and colloid crystallizations.[3, 4, 33, 89] The example herein indicates that the acceleration of precipitation kinetics also exists in the precipitation of organics with polyelectrolyte as additives.

The nucleation of nanoplatelets happens within each PILP droplet. PILP droplets, instead of staying as being isolated, form a PILP superstructure to lower their interfacial energy. Then, as formed nanoplatelets within the PILP superstructure can locally reorient themselves into a radial orientation. Therefore, the as-prepared microspheres show a Maltese-cross extinction pattern between the crossed polarizers (Fig. 5.2.2A). It was demonstrated that the assembly of lamellar nanostructures in a radial orientation is the key for the formation of such patterns in many macromolecular systems such as polymers,[90] DNA,[91] polysaccharides,[92] and proteins.[93] The existence of the Maltese-cross extinction pattern can be extended to Glu precipitation with PEI as an additive, where nanoplatelets are equivalent to the lamellar structure in macromolecular systems. The Maltese-cross extinction pattern is weakened or disappeared when microspheres are air-dried. This phenomenon is similar to the weakening of the Maltese-cross extinction patterns in bovine insulin after being dried, and rehydration is not helpful to regain the pattern.[93] The dehydration of microspheres indicates a permanent disruption of the fine structures between nanoplatelets by capillary forces. The mechanism of the formation of Glu microspheres from a multi-step route from section 5.1 and 5.2 are summarized in Fig. 5.5.1.

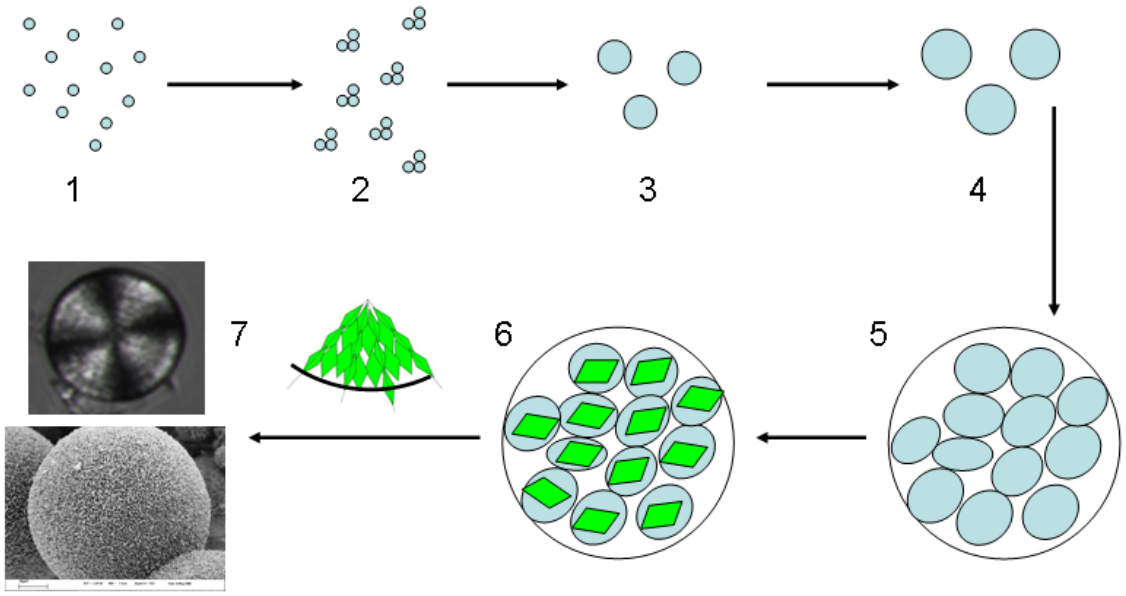

Fig. 5.5.1. The scenario of a multi-step Glu precipitation with PEI as an additive. Step 1→2 takes ~2 sec, and the size of PILP droplets is ~30 nm (SAXS); Step 2→5 takes ~260 sec. Each PILP droplet is ~100 nm, and the PILP superstructure is at least micrometers in size; Step 5→7 takes hours to days, and the microspheres are ~50 μm in size.

5.3 L-His Precipitation with PAA as Additives

The precipitation of L-Histidine (His) with poly (acrylic acid) (PAA) as an additive was investigated herein, varying the His/PAA mass ratio (w/w; **φ'**), [His], the volume ratio of EtOH and His-PAA aqueous solution (λ_1). The experiments were similar to the preparation of Glu microspheres. First, a His-PAA aqueous solution was prepared. The aqueous solution was mixed with EtOH at R.T. thereafter. Finally, the precipitates were collected by centrifugation for characterization. POM was applied to distinguish the bulk crystals from the goal products, as bulk crystals show contrasts in POM while goal products do not (the reason will be discussed later in this section). The samples with pure goal products were sent to SEM to scan the structural details.

First, various parameters were tested to prepare pure goal products. Three aqueous solutions with **φ'** at 9/1, 7/1, and 5/1 were used, and their compositions are summarized in Table 5.3.1. In aqueous solutions with **φ'** higher than 9/1, precipitation can happen within PILP as well as in the bulk phase, resulting in a mixture of bulk crystals and goal products. On the other hand, the driving force for His precipitation is weakened by using aqueous solutions with **φ'** lower than 5/1, only obtaining a mixture of precipitates and coacervates. Then, the effects of [His] and λ_1 for the preparation of goal products are considered together. As to the values of λ_1, pure goal products are can only be obtained when the values are between 5 and 9.

Table 5.3.1 The composition of the His-PAA aqueous solutions

His/PAA (w/w; **φ'**)	[His] ($g \cdot L^{-1}$)	[PAA] ($g \cdot L^{-1}$)
9	80	8.9
7	80	11
5	80	16

Table 5.3.2 summarizes the results from a series of experiments. Firstly, the [His] effect needs to be discussed. [His] = 40 $g \cdot L^{-1}$ is a preferred concentration for the preparation of goal products in eight combinations of **φ** and λ_1 out of nine. In addition, pure goal products were obtained in seven cases out of nine by using an aqueous solution with [His] = 27 $g \cdot L^{-1}$. The driving force for the His precipitation is low by using an aqueous solution with [His] = 20 $g \cdot L^{-1}$, resulting in a mixture of bulk crystals and goal

products in small quantities. On the other hand, high [His] = 80 $g \cdot L^{-1}$ is also harmful for the preparation of the goal products. The reason is that a large amount of His molecules are not included in the metastable PILP phase, and the precipitation can happen directly within the bulk phase. Compared to the [His] effect, the effect from the values of λ_1 is sample dependent.

Table 5.3.2 Crystallization results from aqueous solutions with various values of **φ'**

[His] ($g \cdot L^{-1}$)	EtOH/aqueous solution (v/v ; λ_1)		
φ' = 5	5	7	9
80	**s**	**s**	mixture
40	mixture	**s**	**s**
27	mixture	**s**	**s**
20	/	**s**	mixture
φ' = 7	5	7	9
80	mixture	mixture	mixture
40	**s**	**s**	**s**
27	**s**	**s**	**s**
20	**s**	mixture	mixture
φ' = 9	5	7	9
80	mixture	mixture	mixture
40	**s**	**s**	**s**
27	**s**	mixture	**s**
20	mixture	mixture	mixture

s means goal products
mixture means the existence of bulk crystals with microspheres and nanostructures

The morphology and structural details of goal products are summarized in Fig. 5.3.1. Fig. 5.3.1A is a POM image, which shows that the goal products are microspheres. They are polydisperse in size distribution with the size range from tens of micrometers to ~100 μm. The lacking of shining colors from this image suggests that the products are amorphous or are superstructures of nanocrystals. Fig. 5.3.1B is an overview SEM image of microspheres, which indicates that the microspheres are porous on the surface. A magnified SEM image in Fig. 5.3.1C indicates that the porosity comes from the gaps between of nanoplatelets, and nanoplatelets are the building blocks of the microspheres.

Nanoplatelets are tens of nanometers in thickness and micrometers in size. In addition to microspheres which are the superstructure of nanoplatelets, isolated nanoplatelets are also observable in some samples, as shown in Fig. 5.3.1D.

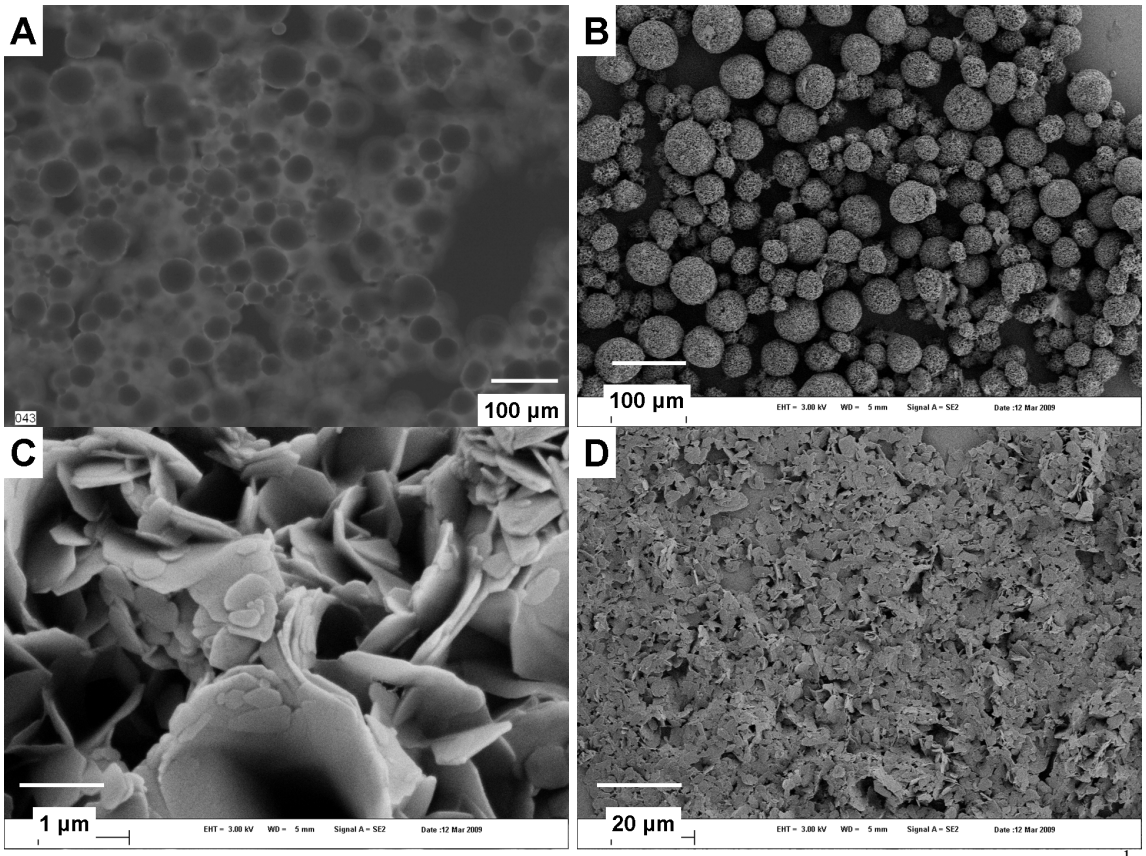

Fig. 5.3.1. Image **A** is a POM image of microspheres (**φ'** = 5/1, λ_1 = 7, and [His] = 80 g·L^{-1}). Images **B** and **C** are SEM images, indicating an overview of microspheres and the surface details of microspheres, respectively (**φ'** = 7/1, λ_1 = 5, and [His] = 40 g·L^{-1}). Image **D** shows the existence of isolated nanoplatelets (**φ'** = 9/1, λ_1 = 5, and [His] = 27 g·L^{-1}).

5.4 L-Pro Precipitation with Oppositely Charged Polymers as Additives

L-proline (Pro) and its derivatives are successful catalysts for many asymmetric reactions.94 Because most organic reactions happen in organic solvents which are non-soluble solvents to Pro, Pro is always modified with hydrophobic functional groups to make the derivatives soluble in organic solvents. Another possible route is to prepare Pro into colloidal dispersions, which should be effective to increase the catalytically active surface areas on Pro. Therefore, the plan is to design Pro nanostructures or Pro

superstructures with nanostructures as building blocks by using charged polymers as additives.

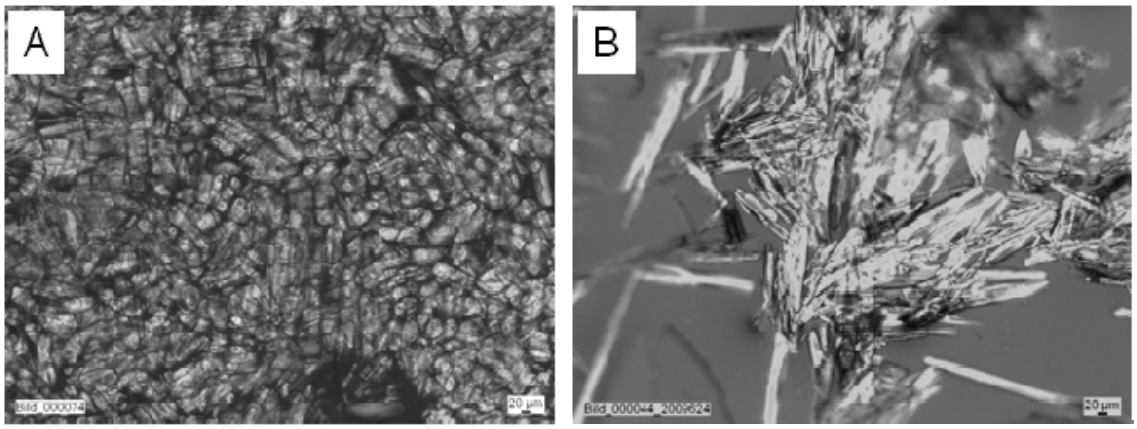

Fig. 5.4.1 Both are POM images. Image **A** was obtained by mixing 0.1 mL Pro aqueous solution with a mixture of 0.03 mL methylpyrrolidone and 0.87 mL acetone. Image **B** was obtained by mixing 0.1mL Pro aqueous solution containing 30 mg polyacrylic acid with a mixture of 0.89 mL acetone and 0.01 mL tetrahydrofuran.

The experiments were performed as follows. Firstly, a series of Pro aqueous solution with various amounts of polymeric additives were prepared. Then, one aqueous solution was mixed with an organic solvent, such as N-Methylpyrrolidone, acetone, or their mixture. Various polymers and block copolymers such as poly(1-vinylpyrrolidine-co-acrylic acid), poly(4-styrenesulfonic acid-co-maleic acid), poly(styrene-alt-maleic acid), poly(sodium 4-styrenesulfonate), and poly(acrylic acid) were applied as additives for the formation of Pro nanostructures (Fig. 5.4.1). However, only bulk crystals were immediately obtained by mixing a Pro-polymer aqueous solution with a non-solvent. The driving force for bulk crystallizations is still strong by using nearly saturated Pro solution. In addition, the interactions between Pro and polymers are not strong enough to form a metastable PILP phase. Parameters such as the pH value,[95] temperature, non-solvency, *etc.* are needed to be investigated in follow up experiments.

6. Preparation of Patterned Hybrid Thin Films

Abstract

The preparation of bioinspired thin films meets difficulty in constructing orders crossing nano-, micro-, and macro-scale. In this chapter, the design of patterned thin films within a quaternary DL-Lys·HCl (Lys)–polyacrylic acid (PAA)–water–EtOH system is presented combining the polymer-induced liquid precursor (PILP) route with an evaporation process. By dip-coating quaternary dispersions onto hydrophilic glass slides, the following multi-step process happens, which includes solvent evaporation, continuous spherulitic mesocrystallization, and a spherulitic recrystallization to a mesocrystalline thin film. Annealing is applied to optimize the processing of the mesocrystalline thin film. Instead of using dip-coating, hierarchical thin films with at least four orders of hierarchy as well as a self-organized pattern structure can also be prepared, starting from the redissolution and recrystallization of the microsphere dispersion. As a comparison, spherulitic thin films are obtained by replacing Lys with L-Lys·HCl, suggesting that the lattice energy can dictate the nanoscale organization. Starting from the same composition, various processing routes terminate at different thin film patterns, suggesting that biomimetic routes are far away from equilibrium processes, and self-organization is important in designing functional thin films with unique properties.

* The LC-PolScope images were taken in Prof. Dr. Dirk Volkmer's lab in University of Ulm with the help from Dr. Haofei Gong.

6.1 Preparation of Mesocrystalline Patterned Thin Films

6.1.1 Introduction

The production of continuous thin films across nano- and macro-scale is of the utmost importance for their industrial applications. Compared with vapor processing routes, which can prepare thin films in a large area with a precisely controlled thickness, solution routes are advantageous for processing nearly all kinds of solid materials at relatively low temperatures, on various substrates, and into complex structures.[96] In principle, thin films are only obtained when the solute-substrate interaction is stronger than substrate-solvent and solute-solvent ones.[97] Otherwise, directly depositing chemicals from their mother liquor always results in isolated single crystal items on the substrate. Adding polymeric additives and changing the substrate property are practical ways to increase the solute-substrate interaction. Processing is also indispensible in controllable thin film synthesis. Two suitable ways, namely spin-coating and dip-coating, have been employed to prepare homogeneous liquid thin layers at macroscale. Spin coating is characterized for the fast evaporation rate, resulting in isolated patterns.[98] Dip coating is specific for the slow evaporation rate, and is preferential for continuous thin film syntheses.[99, 100] For example, dip coating is used for the preparation of continuously ceramic thin film, namely evaporation-induced self-assembly.[100] To position and to orient structures at micro- or even macro-scale are key requisites in the preparation of continuous thin films.

Nature is an expert in processing various materials into well defined hierarchical thin films.[27] Two organic compounds are independent ingredients in biomineralization: highly charged biomacromolecules and insoluble organic matrices. Soluble biomacromolecules play a key role in controlling the nucleation of biominerals and the final morphology; the matrices are suggested to induce the nucleation position at the surface, and to confine the crystallization to proceed within a compartment.[11] Various biomimetic investigations have been performed to prepare continuous thin films. Supramolecular assemblies such as self-assembled monolayers,[101] Langmuir films,[102, 103] and composite membranes[104] have been used as model insoluble matrices to control the growth of thin films with

polyelectrolytes as soluble additives. Isolated thin films with polygonal morphologies are always obtained because of lacking long distance interactions.[104, 105] Therefore, it is interesting to prepare continuous thin films across large areas on various substrates, and to mimic the exact roles of two biomacromolecules in controlling the nucleation and growth of a thin film.

PILP route process is suggested to play a fundamental role in the morphogenesis of biominerals.[17, 106] The micromolar quantities of short-chained polyanionic polyelectrolytes such as poly(aspartic acid) were added to the mineralizing system to interact with mineral cations. The interactions between mineral cations and polyelectrolytes can induce a metastable liquid-liquid phase separation followed by the coalescence of liquid-like colloids on the substrate. Solidification and crystallization then happen in sequence to form a mesocrystalline thin film, since the building blocks of a grain are crystallographically ordered NPs.[106] To follow a PILP route is significant because it can retain the morphology of precursors and produce a variety of morphologies from a non-equilibrium process. PILP route herein is combined with dip coating for the preparation of mesocrystalline DL-Lys·HCl–poly(acrylic acid) (Lys-PAA) thin films on the glass slides. Solvent evaporation plays a key role in the mesocrystallization of a continuously spherulitic thin film on the slide. Then, a mesocrystalline thin film is obtained from the spherulitic phase following an Ostwald's rule of stages. The morphology and crystal structure of the final mesocrystalline thin films were investigated by tuning parameters such as temperature, Lys/PAA (w/w; φ''), [Lys], and EtOH/Lys-PAA aqueous solution (v/v; λ_2). High quality thin films can be prepared through an annealing route.

6.1.2 Results

The multi-step process starts from an evaporation process. When a Lys-PAA aqueous solution was mixed with EtOH, metastable liquid droplets were immediately formed by an L-L phase separation, because EtOH is a non-solvent to Lys and PAA. The metastable droplets several micrometers in size are clearly observable from a series of optical microscopy (OM) images in Fig. 6.1.1. Then, droplets began to collapse within 1 min, and a homogeneous liquid layer was formed within 2 min. The reason is that the

evaporation rate of EtOH is much faster than that of water. Therefore, Lys becomes soluble, which causes the collapse of PILP phase. Finally, spherulite nucleation starts within 6 min.

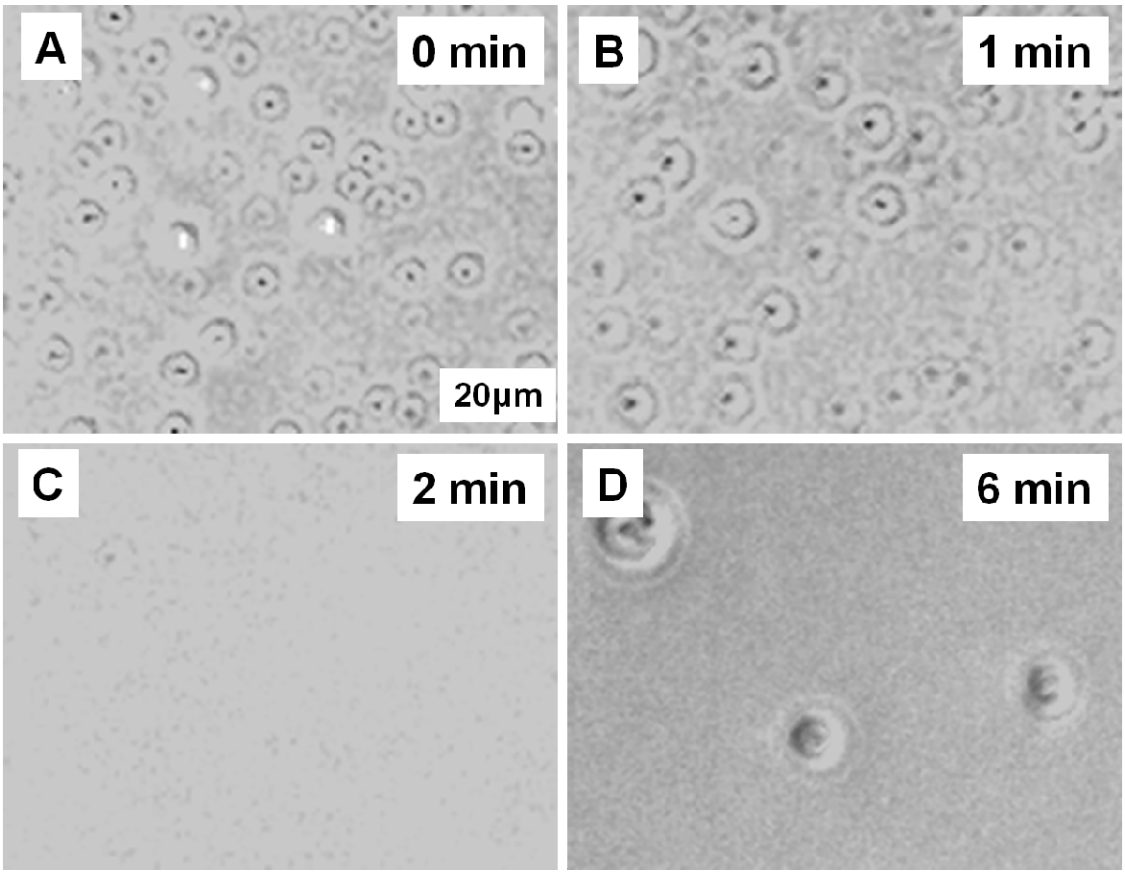

Fig. 6.1.1. The POM images show the disappearance of PILP droplets followed by the formation of spherulites on the hydrophilic glass slide.

The following process is the growth of spherulites (Fig. 6.1.2). It takes 8 min for the spherulites to fill in the whole area, after which they stop growing as they meet with each other. Spherulites in Fig. 6.1.2 are ~100-200 μm in diameter with a wide size distribution. The air humidity is very important for the size control of spherulites. When the humidity is high, fiber-like spherulites several millimeters in size are obtained (image not shown). Contrarily, spherulites less than 100 μm in diameter are formed when the humidity is low (image not shown). The reason is that the humidity controls the evaporation rate of water. EtOH evaporates much faster than water because the vapor pressure of EtOH is much higher than that of water in the PILP dispersion. This difference causes the increasing water percentage in the dispersion. Therefore, the humidity becomes an influential factor

when water becomes the main solvent component. For example, water evaporates slowly when the humidity is high. Then, the first formed spherulites have enough time to grow up to a very large size, suppressing the nucleation of other spherulites. Finally, there may be as few as one to several spherulites covering the slide.

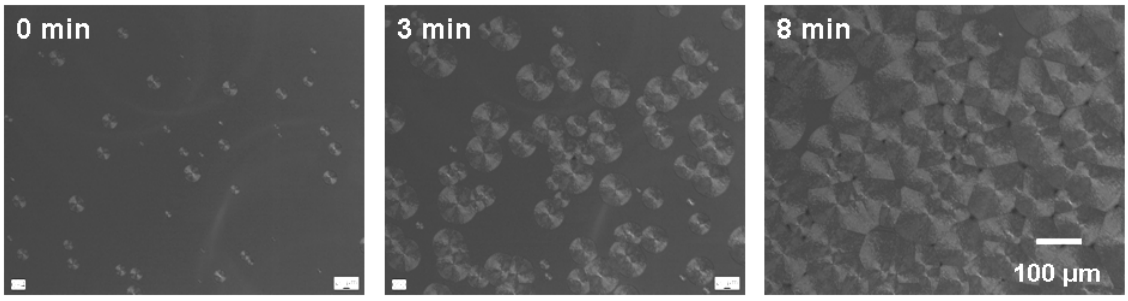

Fig. 6.1.2 The growth kinetics of spherulites on the glass slide.

A comparison experiment was performed by dipping the Lys-PAA aqueous solution on the slide and only isolated white particles were obtained. This result suggests that the existence of EtOH is essential for the formation of continuous thin films. First, the surface tension of EtOH is low, which is helpful for spreading the liquid layer homogeneously on the slide. Second, fast homogeneous nucleation of NPs spanning continuously on the slide can be attributed to the existence of EtOH, which is a non-solvent to Lys and helps to form metastable PILP droplets.

Parameters such as [Lys], [PAA], **φ''**, and λ_2 affect the quality of as-prepared thin films. The composition of aqueous solutions is summarized in Table 6.1.1. These aqueous solution was mixed with EtOH (λ_2 = 9) for the preparation of thin films. Polycrystalline thin films are reliable using samples B and C. As to sample A, thin films only show weak polycrystalline signals under polarized optical microscope (POM), which suggests that the driving force of crystallization is weak under such conditions. On the other hand, the coexistence of microspheres and a polycrystalline thin film is observed in sample D, which is caused by the fast nucleation and growth of microspheres directly in the solution.

The **φ''** effect was investigated by keeping the value at 5, 10, and 20, as summarized in Table 6.1.2. Polycrystalline thin films were obtained when the **φ''** values are between 10 and 20. However, spherulitic thin films were stable when **φ''** is kept at 5 (Fig. 6.1.3D).

Table 6.1.1. The composition of aqueous solutions, where **φ''** is constant at 10/1

	[Lys] ($g \cdot L^{-1}$)	[PAA] ($g \cdot L^{-1}$)
A	30	3
B	50	5
C	70	7
D	100	10

Table 6.1.2. The composition of aqueous solutions, where [Lys] is constant

	[Lys] ($g \cdot L^{-1}$)	[PAA] ($g \cdot L^{-1}$)
C	70	7
G	70	3.5
M	70	14

Table 6.1.3. Morphologies of thin films by mixing sample **C** with EtOH at various values of λ_2

λ_2	**>9**	**7**	**5**	**3**	**2**	**1/1**
Morphology	Amorphous		Polycrystalline		Polycrystal with cracks	

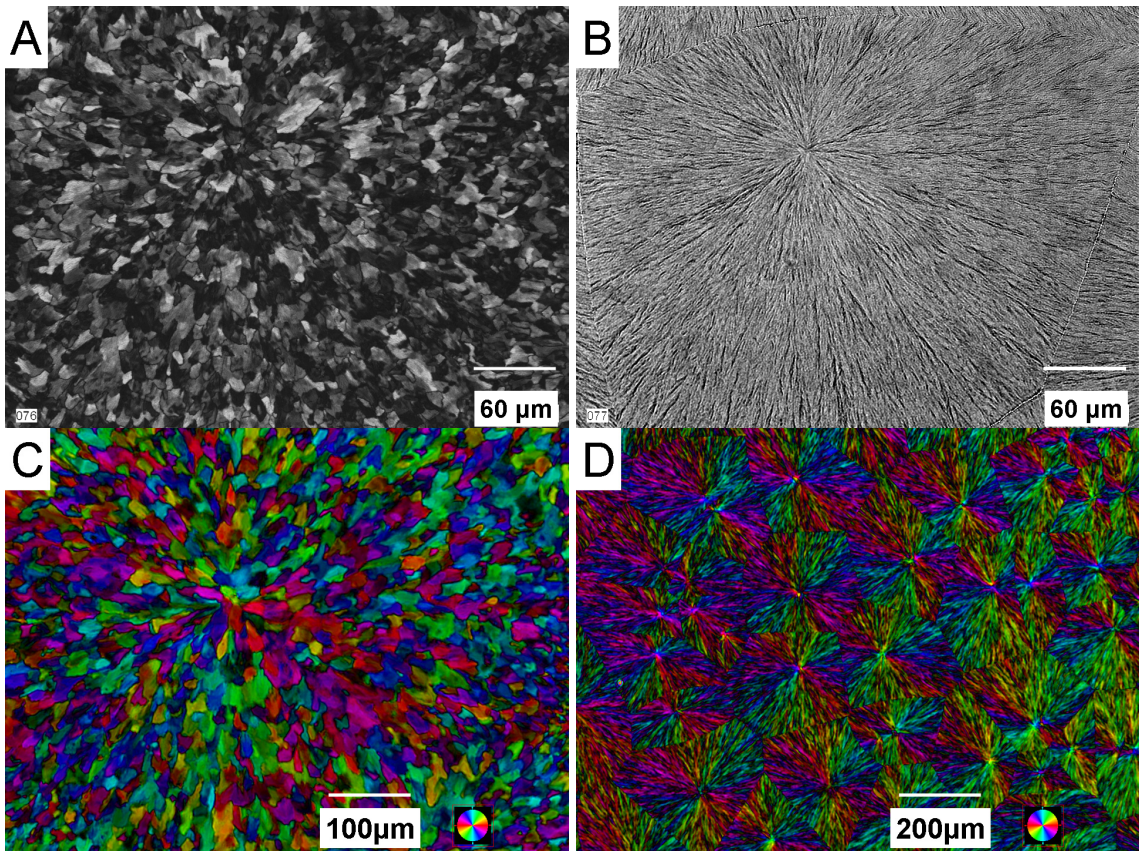

Fig. 6.1.3. Images **A** and **B** are POM and OM images of a domain at the same area (sample G; λ = 5), respectively. Images **C** and **D** are LC-PolScope images of sample G, λ_2 = 5 and sample M, λ = 3, respectively.

The value of λ is also an important parameter to determine the quality of the polycrystal thin film (Table 6.1.3). The morphologies of thin films by mixing sample C with EtOH at various values of λ_2 were examined. When $\lambda_2 \geq 9$, there is a weak contrast in POM, suggesting that polycrystalline thin films are poorly crystallized. High quality polycrystalline thin films are obtained when λ_2 is between 3 and 7. However cracks are observable when λ_2 is between 1 and 2.

The birefringence microscopy technique (LC-PolScope) was used to find the inner relationship between the polycrystalline thin film and the spherulitic morphology. LC-PolScope measures the retardance magnitude at every pixel of a charge-coupled device (CCD) image. It can therefore provide quantitative information of the orientation of each polycrystal. An LC-PolScope image in Fig. 6.1.3C shows the dominance of warm color in the horizontal direction and paramount cold color in the vertical direction. Such orientation is reminiscent of iso-oriented spherulites.

AFM helps to understand the structural information on the surface. AFM images show that the surface morphology of a polycrystalline domain is similar to that of a spherulite. Each domain is composed of radially oriented fibrous structures (Fig. 6.1.4A). Fibers are highly branched, which is typical for spherulitic structures (Fig. 6.1.4B).[107] Each branch is a nanoparticle (NP) array and each NP is ~30–40 nm in size, as shown in Fig. 6.1.4C. As the building blocks are NPs and those within one polycrystalline grain are oriented, polycrystalline thin films are mesocrystalline in nature with the surface morphology as a reminiscence of spherulitic mesocrystallization.

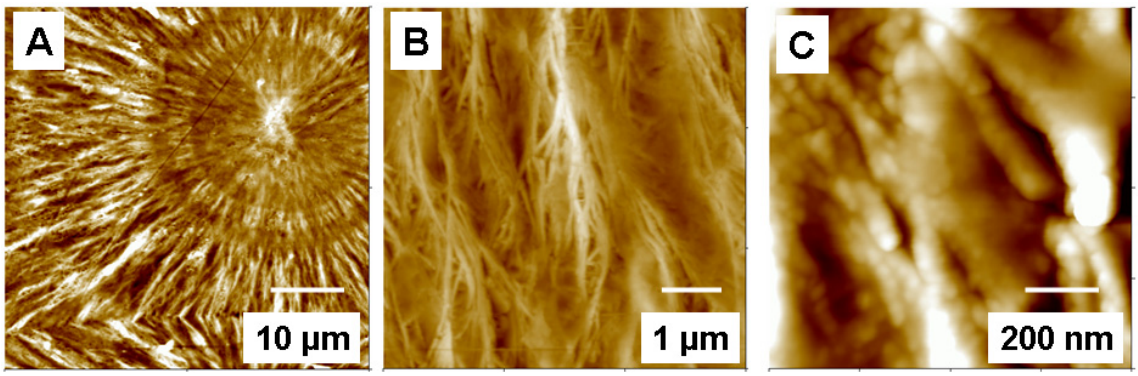

Fig. 6.1.4. Image **A** is an overview of a spherulitic domain; image **B** shows the fiber-like structures on the surface of polycrystalline film; image **C** indicates that the fiber-like structure is an NP assembly. (sample G; $\lambda_2 = 5$)

Mesocrystalline thin films, spherulitic thin films, and Lys precipitates show different crystallographic structures to each other, as demonstrated in Fig. 6.1.5. There are two possible explanations. The first one is that the component in spherulitic or mesocrystalline thin films has a formula different from DL-Lys·HCl. Another possibility is that there are two new Lys polymorphs in spherulitic and mesocrystalline thin films, separately. Further work on clarifying the crystal structures is needed.

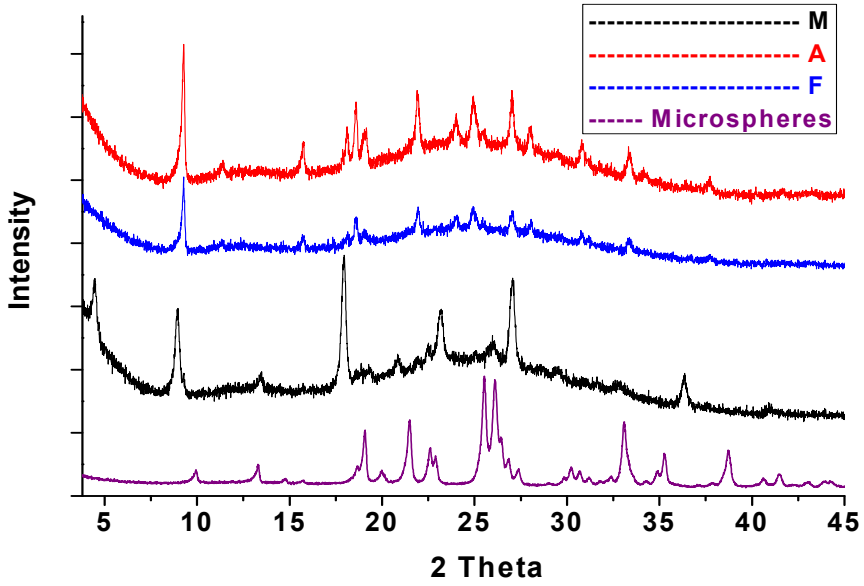

Fig. 6.1.5. Crystallographic patterns of thin films by mixing sample M, A, and F (λ_2 = 3). The bottom pattern is from Lys precipitates collected in solution.

AFM, time-resolved WAXS, and LC-PolScope were used independently to detect the structural transformation from spherulitic to mesocrystalline thin films. AFM result shows clearly NPs ~40 nm in diameter are immediately formed within the spherulitic matrix (Fig. 6.1.6A). Therefore, the formation of spherulite thin films is a spherulitic mesocrystallization. There was no visible size change for NPs thereafter by comparing results in Fig. 6.1.6A and C, suggesting that the transformation from a spherulitic to mesocrystalline thin film happens following an Ostwald rule of stages.

WAXS data show that there is no crystalline structure within a newly formed spherulitic thin film (Fig. 6.1.6B; the blue pattern). Some peaks show up in ~5 hours, suggesting the crystallization of NPs with time (Fig. 6.1.6B; the red pattern). The peaks

belonging to the above spherulitic thin film correspond well to the pattern from sample M (Fig. 6.1.5; the black pattern). The mesocrystalline thin film, which is formed from an Ostwald's rule of stages, shows a pattern (Fig. 6.1.6B; the black pattern) different from the spherulitic thin film.

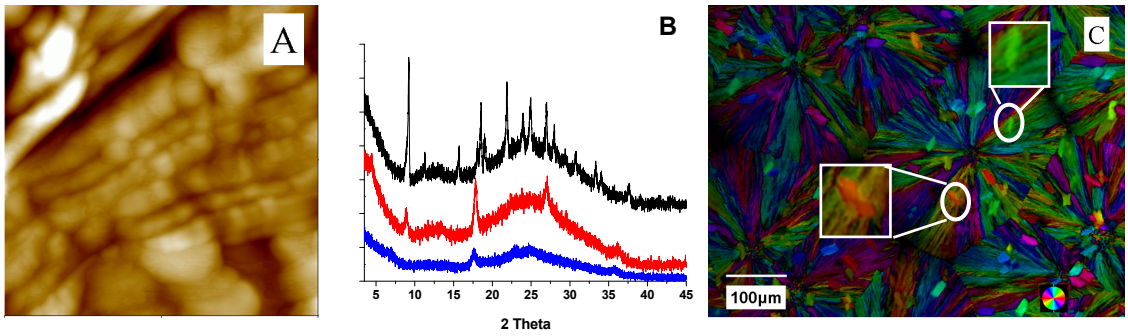

Fig. 6.1.6. Image **A** is an AFM image, showing a spherulitic thin film after being formed in one hour. The image is 500 nm in size. Image **B** indicates a series of time-resolved WAXS patterns. The pattern collected in 1 hour (blue) and 5 hours (red) has been compared with that from the final product (black). Image **C** is a LC-PolScope image during the transformation from spherulitic to mesocrystalline thin films (in one hour). (sample G; $\lambda_2 = 5$)

LC-PolScope technique helps to understand the orientation transformation between the spherulitic and mesocrystalline thin films. Fig. 6.1.3C already shows that the nearly iso-oriented mesocrystalline thin films are reminiscent of spherulitic thin films. The question is whether the same area shows the same orientation before and after the recrystallization from spherulitic to mesocrystalline thin films. Fig. 6.1.6C shows that grains start to grow sporadically within the spherulitic matrix. Most mesocrystalline seeds follow the same orientation as the spherulitic matrix. However, some mesocrystalline seeds show close orientations to their matrices because of the existence of thermal fluctuation.

Temperature drop is a key technique in material processing. It is herein used to tune the properties of mesocrystalline thin film such as the size and orientation of mesocrystalline grains. The evaporation process was performed at 40ºC and the spherulitic thin film formed was subjected to a temperature drop in two ways: quenching or annealing. The experiments were performed by using sample G and the value of $\lambda_2 = 5$.

If the temperature was dropped immediately from 40ºC to R. T., the structural change also happened immediately and finished within 5 min. Fig. 6.1.7 is a POM image,

indicating the existence of closely packed worm-like structures. Each worm-like structure is several hundreds of nanometers in width and several micrometers in length. The inserted image is an OM image from the same area, where rough structures spread homogeneously on the slide. Fig. 6.1.7 reminds us of its similarity to spinodal thin films. The kinetics of a quenching process is summarized in Fig. 6.1.8. Three POM images in sequence show that the structural change is homogeneous and simultaneous within the spherulitic matrix. The whole process finishes within 5 min. AFM and WAXS will be helpful in determining the morphology at the nanoscale and the crystallography of the above thin film.

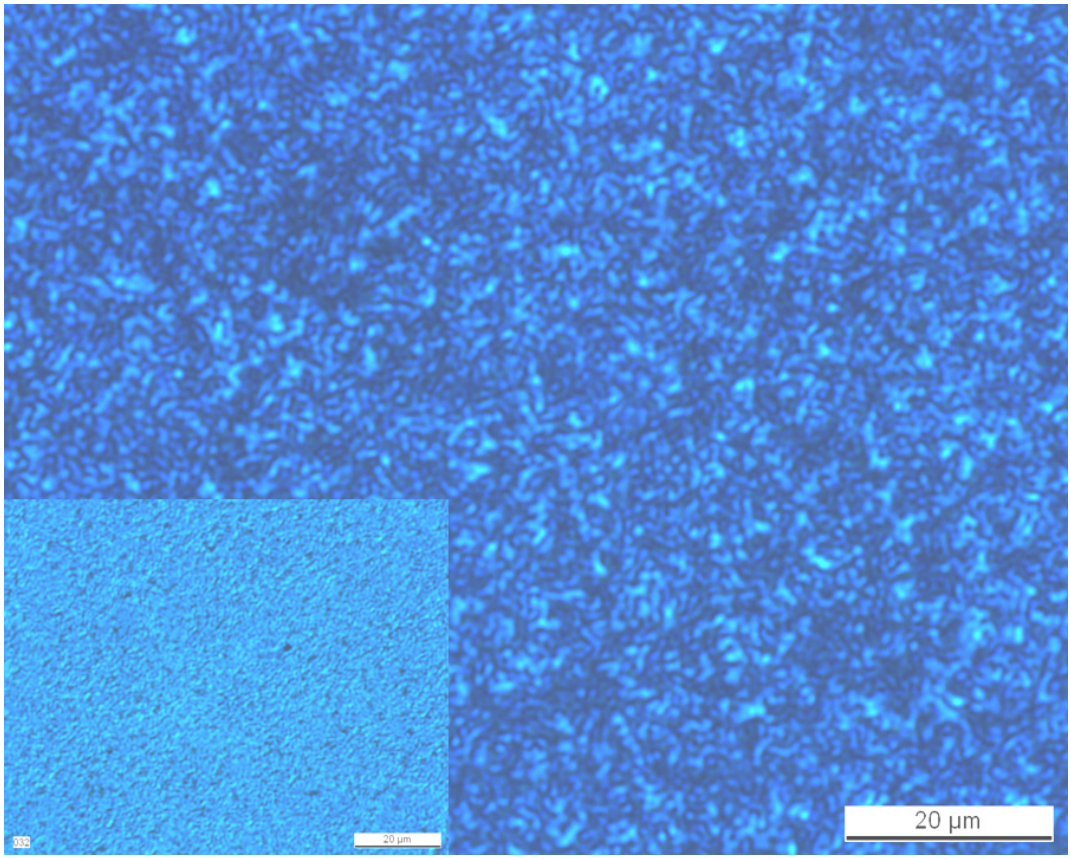

Fig. 6.1.7 is a POM image, showing the morphology of a thin film by quenching the temperature from 40ºC to R. T. The inserted image is an OM image from the same area. (sample G; $\lambda_2 = 5$)

In another route, a spherulitic thin film was annealed from 40ºC to R. T. slowly, obtaining a mesocrystalline thin film. Fig. 6.1.9A is a typical POM image, showing that each mesocrystalline grain is tens of micrometers in size. Different from nearly iso-oriented mesocrystalline grains prepared at R.T. directly (Fig. 6.1.3C), an LC-PolScope

image shows that the orientation of mesocrystalline grains by an annealing process is randomly distributed (Fig. 6.1.9B).

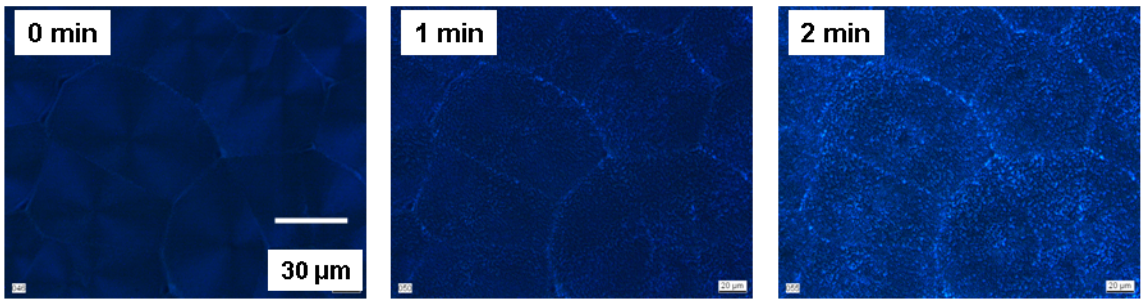

Fig. 6.1.8 are POM images, showing the kinetic change from spherulitic to spinodal-like thin film by quenching the temperature from 40ºC to R.T. They were taken at the same position. (sample G; $\lambda_2 = 5$)

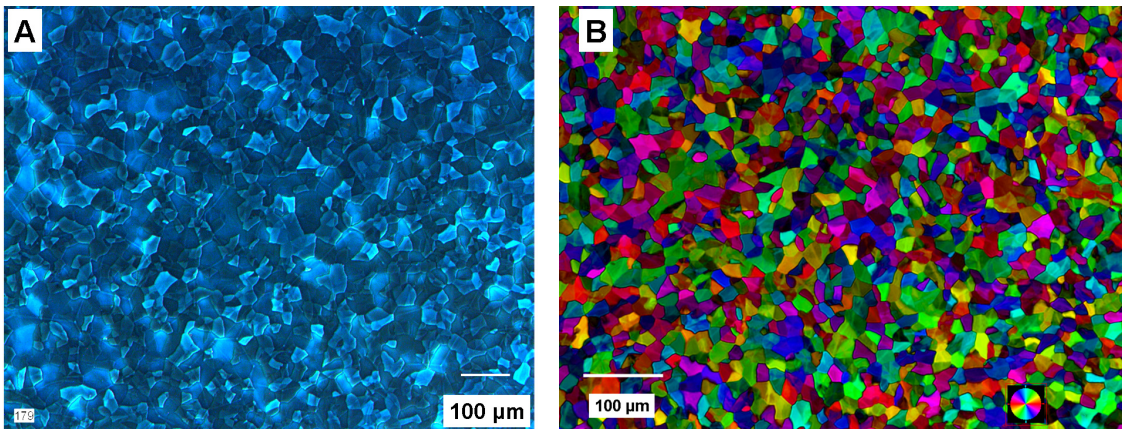

Fig. 6.1.9. Fig. **A** is a POM image, showing a mesocrystalline thin film by annealing the sample from 40ºC to R. T. in 24 hours. Fig. **B** is a LC-PolScope picture of the same sample. (sample G; $\lambda_2 = 5$)

AFM was used to check the structural details of mesocrystalline thin films on micro- and nano-scale. Three domains in Fig. 6.1.10A are the reminiscences of spherulitic domains. Each domain is tens of micrometers in size. Each white spot is the nucleation position of a spherulitic domain. The whole domain is flat on the nanoscale (within ±5 nm from AFM image analysis; not shown), except for the boundary (~ –40 nm) and the nucleation spot (~ +40 nm). Each domain breaks into many single crystalline grains ~5–20 µm in size, as observed from Fig. 6.1.10B. Although grains show polygonal morphology from both POM and LC-PolScope images in Fig. 6.1.9, a detailed scan in Fig. 6.1.10B shows that the boundaries between grains are curved lines. Fig. 6.1.10C shows that the building blocks of grains are tightly packed NPs ~40–50 nm in size. NPs

are the only phase, suggesting that PAA is dispersed homogeneously with Lys in NPs. Compared with the mesocrystalline thin films obtained directly at R.T., those from an annealing process are advantageous for the flat surface on the nanoscale and the random orientation distribution of grains.

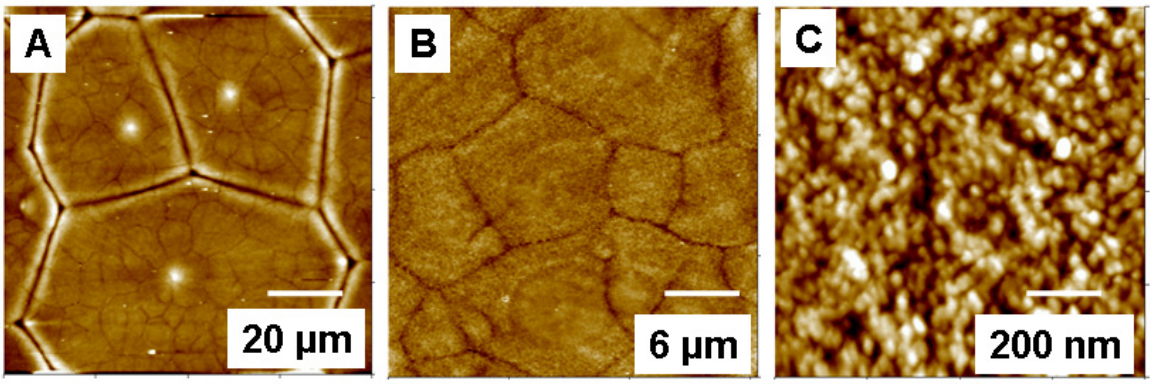

Fig. 6.1.10. Three AFM images at different scales, showing structures from domain, grain, to NPs. (sample G; $\lambda_2 = 5$)

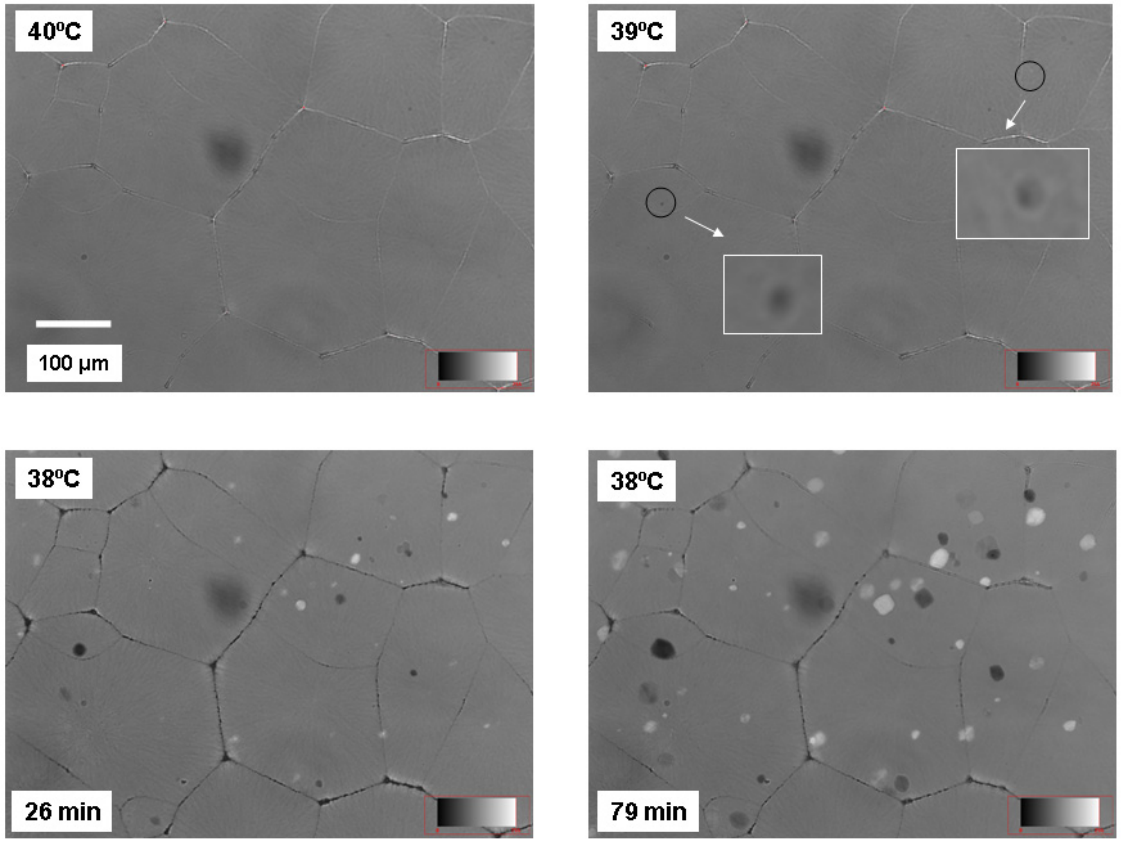

Fig. 6.1.11. The nucleation and growth of a mesocrystalline thin film from a spherulitic matrix in an annealing process. Two grains in the black rectangles are magnified newly formed grains from the black circles. (sample G; $\lambda_2 = 5$)

The nucleation and growth process of the mesocrystalline thin film was also examined by combining a heating platform with the LC-PolScope technique (Fig. 6.1.11). Spherulitic thin film was stable between 50ºC and 40ºC. At 39ºC, the appearance of several nuclei was observed, two of which are highlighted by black circles (see the magnified images in the white cubes) in Fig. 6.1.11. The growth of grains was then scanned at 38ºC. After the calculation, the average growth rate of a mesocrystalline grain is ~ 360 $nm \cdot min^{-1}$ at 38ºC. It is difficult to determine the precise rate since the growth on each direction is not equal and the formed mesocrystalline grains do not grow spherically.

To examine the stability of mesocrystalline thin films, samples were heated at 170ºC, which is close to the melting point of Lys. However, there was no change in the mesocrystalline thin film thereafter.

6.1.3 Discussion

This work is inspired by the patterned thin films in biominerals, where morphologies far from equilibrium are produced from a biological control of grains such as orientation, size, shape, and arrangement. Different from biomimetic thin films with isolated single crystalline patches by using a LB membrane or self-assembly monolayer as a template, continuously mesocrystalline thin films were obtained. A metastable Lys-PAA-water-EtOH mixture was dropped on a hydrophilic glass slide via a dip-coating approach. The following evaporation process fused the immediately nucleated PILP NPs onto the glass slide to form spherulitic domains, resulting in continuous thin film. The following crystallization and recrystallization of NPs caused the formation of mesocrystalline grains several micrometers in size within each domain whilst the morphology of NPs was maintained. An annealing process was found to be advantageous for optimizing the synthesis of thin films, which are flat on the nanoscale.

Thin films herein are unique for their mesocrystalline property. Normally, single crystalline thin films start to grow from a surface-induced heterogeneous nucleation, where the grains larger than the critical value continue growing by moving the grain boundary forward. Grains after a surface-induced heterogeneous nucleation show single-crystal morphologies. In mesocrystalline thin films, however, the building blocks are crystallographically oriented NPs, which interact with each other by dipole-dipole

interactions. Mesocrystalline thin films have also been reported elsewhere. For example, mesocrystalline $CaCO_3$–poly(aspartic acid) thin films were selectively grown on the patterned hydrophilic thin films from PILP deposition.[106] Similarly, the PILP route can be used to explain the multi-step formation of the mesocrystalline thin films in this section.

The continuous thin films are formed from a spherulitic mesocrystallization process during the evaporation process. After the formation of a homogeneous liquid layer on the slide, further evaporation causes an L-L phase separation after the solute concentration surpasses the threshold value. The metastable PILP nanodroplets, which are rich in solutes, fall on the slide and form a continuous NP thin layer. Thereafter, the final evaporation process ruptures the continuous NP layer into many domains tens of micrometers in size. Simultaneously, NPs are weakly connected on the receding direction of the liquid layer. Therefore, they are radially oriented and coalesce into spherulitic thin films within each domain. The formation of the spherulitic domains is a far from equilibrium process.[25]

The recrystallization into mesocrystalline thin films from the spherulitic phase is induced by the thermal fluctuation. Interestingly, there is no observably morphological change for the NPs during the recrystallization process, and only the radial interactions between NPs in a spherulitic domain are replaced by the dipole-dipole interactions between NPs. Therefore, the transformation from spherulitic to mesocrystalline thin films corresponds well with the Ostwald's rule of stages. However, it is possible for NPs in the spherulitic phase to move locally during the recrystallization process. The driving force for NP reorientation is weak at R.T. Thus, nearly iso-oriented mesocrystalline thin films were obtained, which is the reminiscence of the iso-oriented spherulitic thin films.

The annealing process is advantageous for obtaining high quality mesocrystalline thin films for two reasons. Firstly, it provides NPs more thermal energy to move locally; therefore, thin films with a flat surface on the nanoscale are obtained. Secondly and importantly, it provides energy for NPs to reorient themselves and to interact with the neighboring NPs. There are reversible structural fluctuations between NPs within spherulitic thin films when the temperature is above the recrystallization value. However, the interactions between NPs become irreversible when the temperature stays below the recrystallization value. Then, neighboring NPs can reorient themselves by dipole-dipole

interactions within spherulitic domains. Consequently, NP clustering seeds are formed. When the seed size is larger than a critical value, mesocrystalline grains grow irreversibly. They stop growing when two growing grains meet each other. The orientation of grains is randomly distributed because of the existence of relatively large thermal fluctuations. The whole process is summarized in Fig. 6.1.12.

Mesocrystalline thin films show several key differences from classical thin films using atoms or ions as building blocks. First, both the size and orientation of grains are unchangeable by heating the as-prepared mesocrystalline thin films near to the melting point of Lys. In classical thin films, however, recrystallization indeed happens by heating the sample to a temperature near to the melting point. Then, thin films with large grains are obtained from an recrystallization process. However, the recrystallization process is not observable in the mesocrystalline thin films. Therefore, it is more difficult to break the dipole-dipole interactions between crystalline NPs in the mesocrystalline thin films, compared to break the ionic or covalent bonds in classical thin films. Secondly, mesocrystalline thin films are free from cracks. The NPs in mesocrystalline grains are reminiscence of PILP nanodroplets and their existence helps to release the stress from neighbouring domains during the evaporating and recrystallization process, the latter of which is the main reason that the thin films are crack free. Cracks are otherwise extremely hard to remove from crystalline thin films from a solution route by a surface-induced heterogeneous nucleation.

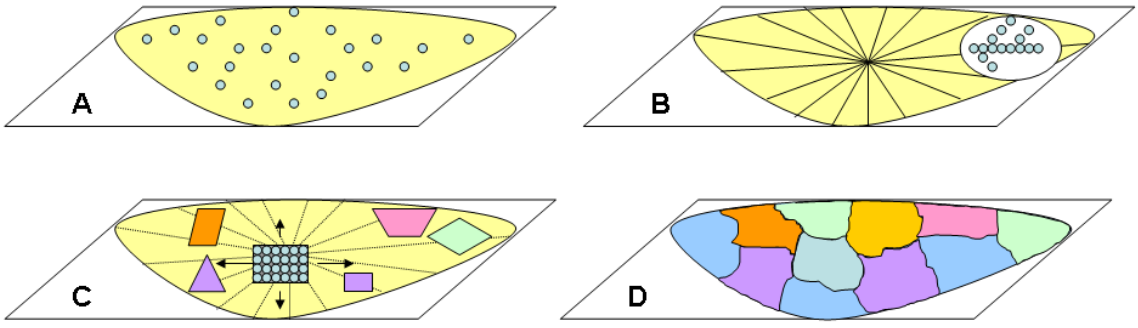

Fig. 6.1.12. The mechanism of mesocrystalline thin film formation

Results herein support the notion that the combination between PILP route and evaporation can be a possible route for the formation of bioinspired hybrid thin films.

Evaporation force, as well as other physical forces, can be used to bring order on the micro- to macro-scale. Mesocrystalline thin films with preferred orientations can be obtained by using templates with preexisting orders. In addition, specific nucleation points can be introduced to precisely control the nucleation position. Therefore, patterning and lithography can be combined to the current PILP system for the preparation of patterned biomimetic thin films with a preferred orientation and at designed positions.

6.2 Hierarchical Mesocrystalline Thin Films

6.2.1 Introduction

Hierarchy is a universal principle in biominerals such as bones and woods.[27] For example, bone has up to seven hierarchical levels of organization.[108] Various biominerals have been analyzed with microscopes to understand their structural details. On the other hand, a general biomimetic method for hierarchical material synthesis is still lacking. The main reason is that biominerals are constructed far from equilibrium processes, which are characterized as being porous and show curved morphologies.[11] Current synthetic methods for hierarchical materials are always performed within the preexisting templates, which are introduced from lithography or patterning.[109] Only few free standing hierarchical materials have been prepared successfully till now.[99, 110]

Solvent evaporation is indeed effective in the formation of various patterned thin films, though it is not a driving force in biomineralization. Solvent evaporation is far from equilibrium process, which can position supramolecules, macromolecules, and NPs into various complex patterns.[111, 112] The uniformity of the solvent evaporation on the substrate and the fluctuation of the solute boundaries are suggested among the key parameters to understand the morphology of patterned structure.[112] Thin films are obtained only if the substrate-solute interactions are stronger than the solvent-substrate and solvent–solute interactions.[97]

Here, the preparation of hierarchical thin films with four hierarchy levels is introduced. The reaction starts from DL-Lys·HCl–poly(acrylic acid) (Lys-PAA) microsphere redissolution and recrystallization on a hydrophilic slide. An evaporation-induced self-organization of PILP nanodroplets is responsible for the formation of hierarchical mesocrystalline thin films. To the best of our knowledge, this is the first proof for the direct transformation of PILPs into a hierarchical mesocrystalline thin film with four hierarchy levels in a single preparation step.

6.2.2 Results

Fig. 6.2.1 A is an OM image, providing an overview of the patterned thin films on the slide. Patterns show a fan-shaped morphology and are hundreds of micrometers in

size. Each pattern starts from the same nucleation position where structures begin to grow. Patterns stop growing when they meet each other. The growing direction of the boundary is abruptly changed at the boundary, as clear seen in Fig. 6.2.1A. Fig. 6.2.1 B focuses on one pattern. The pattern contains many pin-leaf structures, all growing radially from the same nucleation center. Each pin-leaf structure is tens of micrometers in width, and the structure is growing wider along the growing direction. Each fan-shaped pattern is an assembly of pin-leaf structures.

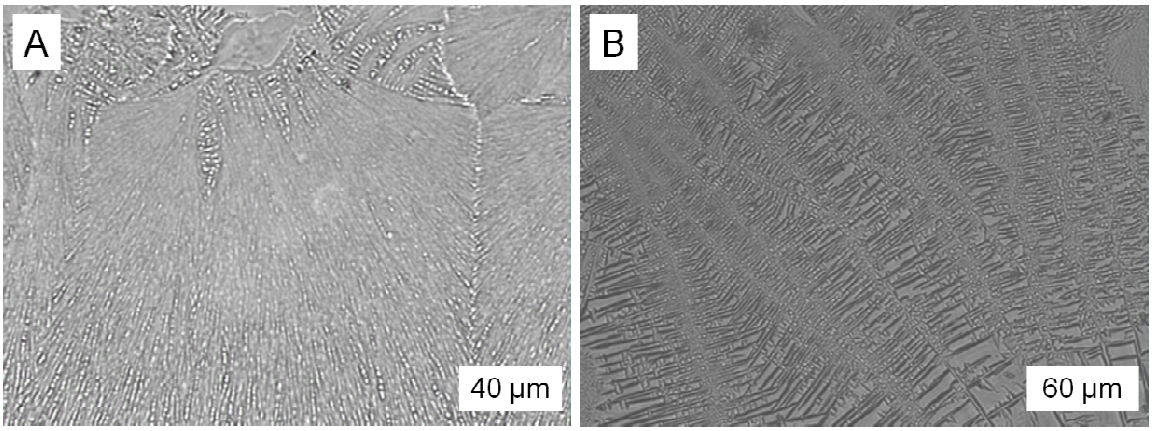

Fig. 6.2.1. Both are OM images. Image A shows an overview of two patterns and the boundary in between. Image B focuses on one pattern, giving the structural details on the microscale.

AFM was used to provide structural details of the thin film on the micro- and nano-scale. Fig. 6.2.2A shows the structural details of one pin-leaf structure. There are two kinds of structures within a pin-leaf: axis and wings. Each axis structure is ~1 μm in width, growing along the growth direction of the pattern. Wings are rod-shaped structures, hundreds of nanometers in width and several micrometers in length. Wings grow vertically to the axis. In Fig. 6.2.2B, it is clear seen that both axis and wings contain lamellar structures. Four lamellar structures grow in parallel along the axis direction. As to the wings, several lamellar structures which are ~50 nm in width pack in parallel to form rod-like structures along the direction of wings. A closer scan of several lamellar structures indicates that each lamellar structure is a 1D NP assembly (Fig. 6.2.2C). The size of NPs is ~50 nm. Hierarchical thin films are mesocrystalline in nature.

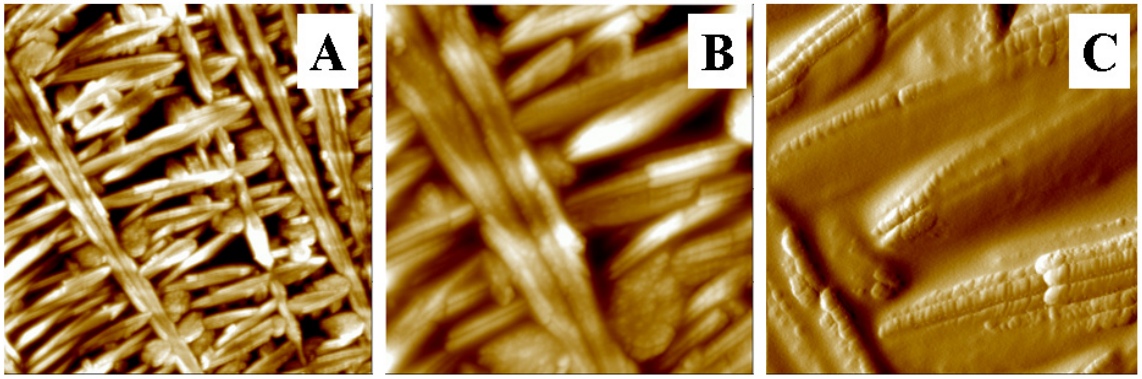

Fig. 6.2.2. Three AFM images indicate the hierarchy from micro- to nano-scales. The scale of images **A**, **B**, and **C** is 10, 4, and 2 μm, respectively.

WAXS data indicate that the hierarchical thin film shares the same crystalline structure with microspheres precipitated directly from the solution (Fig. 6.2.3). However, the intensities of some peaks are different in two patterns, which can explain the size and orientation of NPs within mesocrystalline thin films.

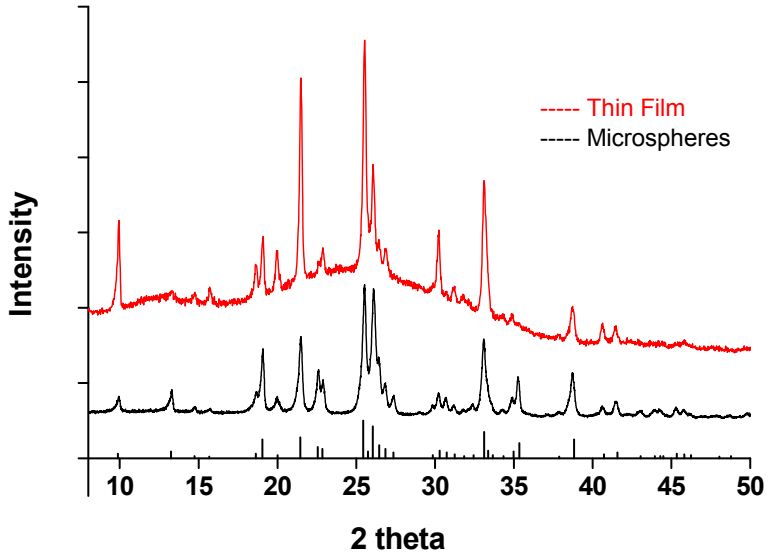

Fig. 6.2.3 shows the WAXS patterns from microsphere and hierarchical thin film. The standard pattern is shown at the bottom as columns.

The formation of hierarchical thin films is as follows. When the microsphere dispersion is dropped on the glass surface, the solvent begins to evaporate. As the vapor pressure of EtOH is higher than that of water, EtOH evaporates faster than water. At a certain composition, the solution becomes unsaturated, and the microspheres begin to dissolve (Fig. 6.2.4). Then, further evaporation makes the solution saturated again. The

newly formed PILP NPs self-assemble into the seeds, which act as nucleation points for the growth of hierarchical domains by adsorbing NPs from the solution.

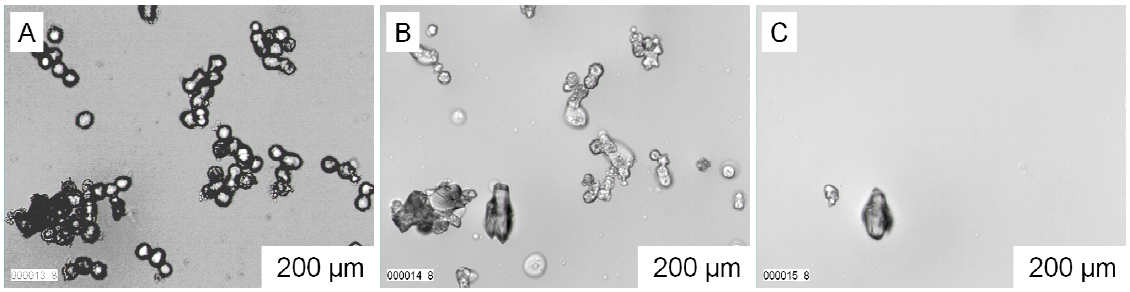

Fig. 6.2.4. Three OM images show how the precursor liquid thin film is formed from microsphere redissolution. Pictures were taken in 0, 5, and 10 min.

6.2.3 Discussion

The existence of EtOH is essential for the formation of hierarchical thin films. EtOH helps to spread the precursor phase on the surface and to form a continuous liquid layer. In addition, EtOH is a non-solvent for Lys. With the evaporation of the solvent, L-L phase separation happens and PILP nanodroplets nucleate. PILP droplets fall on the slide and aggregate into a hierarchical thin film. K_2SO_4/PAA hierarchical crystals are obtained by evaporating the K_2SO_4/PAA aqueous solution, where a slow evaporation is responsible for the oscillation growth modes between 2D and 3D.[110]

PAA has multiple effects from its interaction with Lys, to the NP nucleation and NP self-organization. Firstly, PAA forms complexes with Lys in aqueous solutions. In addition, PAA can stabilize PILP NPs at the nanoscale from an Ostwald ripening process. Furthermore, PAA molecules near to the NP surface might be responsible for assembling NPs into the lamellar structure, wings, and axis during the solvent evaporation. PAA is reported elsewhere to have two chemical environments; it can be strongly incorporated, or loosely attached to the crystal surface in K_2SO_4/PAA hierarchical crystals.[110] However, it is difficult to distinguish how PAA distributes within the hierarchical thin film in this section, because the decomposition temperature of Lys and PAA is too close to distinguish by using a thermogravimetric analysis.

The structural analysis is summarized in Fig. 6.2.5. The formation of complex structures between Lys and PAA and their precipitation by an evaporation process is believed to be responsible for the formation of free-standing hierarchical thin films

without the introduction of pre-existing hierarchy by lithography. These results are among the few in preparation of hierarchical thin films by using bottom-up approaches. The presented thin films show many similarities to natural systems, though on different size scales. To understand the mechanism of hierarchical or self-organized thin films, it is useful to understand complex structure formation in the biosphere and in turn rationally design synthetic thin films with complex structures.

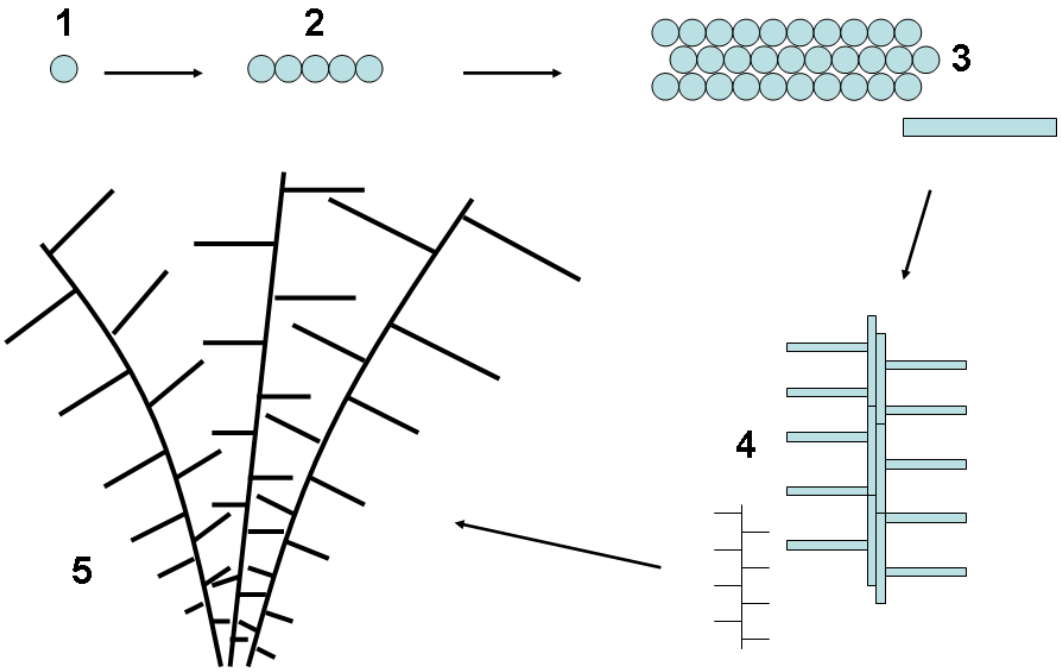

Fig. 6.2.5 shows every hierarchy in the mesocrystalline thin film. Five structures are 1. NPs, 2. lamellar structure, 3. wings and axis, 4. the pin-leaf structure and 5. the fan-shaped pattern.

6.3 Self-organized Hybrid Thin Films

6.3.1 Introduction

Periodically patterned superstructures are common in the biosphere. For example, nacre shows spiral or target patterned structures with the periodicity at the microscale.[113, 114] They also exist in self-oscillating chemical reactions,[115] semi-crystalline polymer crystallization from melt,[116] and biomimetic crystallization processes.[117-120] Kato's group systematically investigated the formation of periodic patterned $CaCO_3$/PAA hybrid thin films on a chemically cross-linked hydrogel matrix.[119-121] A two-step mechanism is suggested as follows: the formation of $CaCO_3$ flat thin film with c-axes periodically switching between perpendicular and parallel to the growth direction, followed by the 3D growth using the flat thin film as a template. Wang *et al.* observed the existence of periodic patterns in $BaCO_3$ precipitation with double hydrophilic block copolymers as additives on the glass slide by tuning the pH value and concentration of the block copolymer.[118] The coupled reaction-diffusion process where the formation of Ba^{2+}-polymer complex as the key step is responsible for the formation of periodic patterns. The equal distanced patterns suggest that a process with mathematics very similar to the Belousov-Zhabotinsky reaction in nature. In both cases, the periodicity of patterns is several micrometers in size.

In this section, the formation of periodic pattern from DL-Lys·HCl (Lys) precipitation with poly(acrylic acid) (PAA) as an additive is introduced. The thin films were formed directly on the glass surface with solvent evaporation. Evaporation and interactions between Lys and PAA are collaborative for the formation of periodic patterns.

6.3.2 Results

Fig. 6.3.1 A is a POM image, showing an overview of a ring-like superstructure about one millimetre in size scale. The periodicity on different directions is slightly different. For example, the periodicity on the right direction is ~27 μm; whilst that on the left side is only ~24 μm. Therefore, a ring-like superstructure is an assembly of several fan-shaped patterns. Several mismatch gaps between fan-shaped patterns are observed

and highlighted within the white circles in Fig. 6.3.1 A. The periodicity within each fan-shaped pattern is equally distanced. Several periodic superstructures grow simultaneously on the slide, and they stop growing when they collide with each other (Fig. 6.3.1 B). The periodicity near to the boundary is not regular any more.

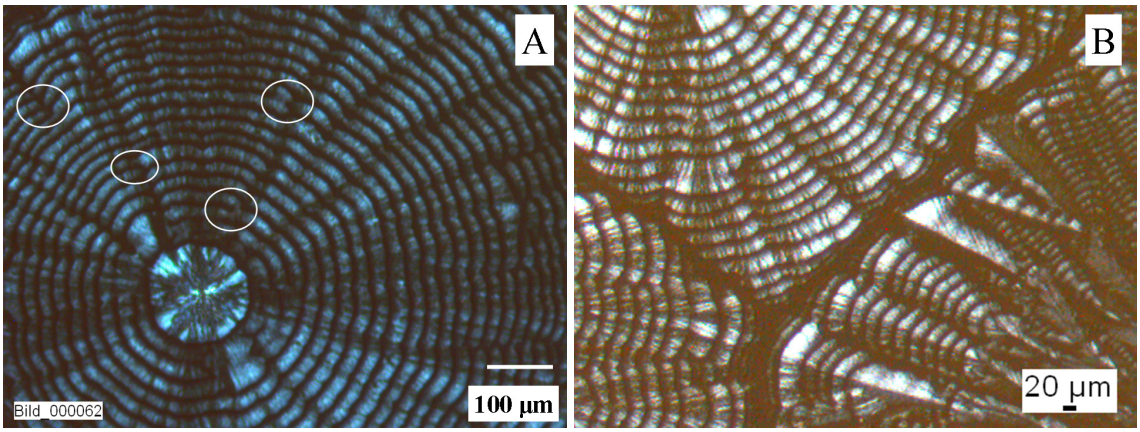

Fig. 6.3.1. Image **A** is an overview of a ring-like structure, where the mismatches are highlighted by white circles. Image **B** shows the boundaries among ring-like structures.

SEM helps to understand the structural details of a fan-shaped pattern on the micro- and nano-scale. Fig. 6.3.2A is an overview SEM image of a fan-shaped pattern (on the right side of the ring-like superstructure in Fig. 6.3.1), proving again the equal periodicy in length within the fan-shaped pattern. Fig. 6.3.2B shows that the bright colour in Fig. 6.3.1 A comes from nanosheet assembly. All nanoplatelets are oriented parallel to the glass surface and along the radial growth direction of a fan-shaped pattern. Each ring structure is ~20 µm in width, and the gap in between is ~7 um in length in Fig. 6.3.2B. A SEM image at high magnification tells that nanoplatelets are ~100 nm in width and ~1 µm in length, as shown in Fig. 6.3.2C.

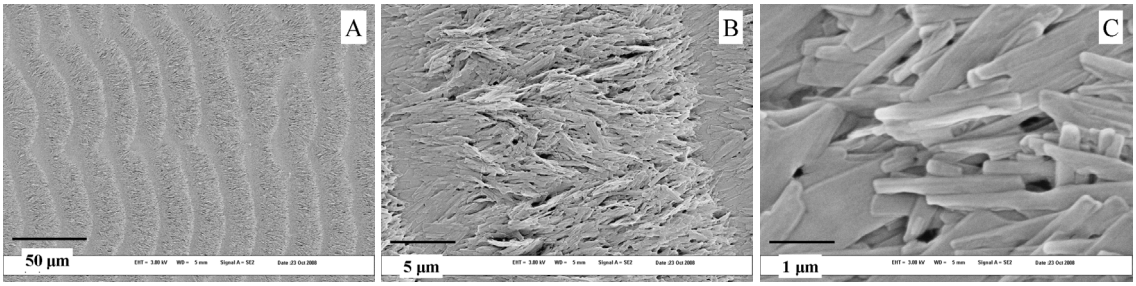

Fig. 6.3.2. Three SEM images of the self-organized structures at different scales.

6.3.3 Discussion

The formation of Lys/PAA periodic structure is governed by the combination of precipitation and solvent evaporation. Lys/PAA complexes exist in the water-EtOH mixture. During the evaporation process, the solution becomes supersaturated for Lys, which causes the precipitation of nanoplatelets. The precipitates are organized into the direction along the receding line of the liquid layer during the evaporation process, and an arc layer is obtained thereafter. This is the initial step for the generation of an oscillation reaction. Simultaneously, the liquid layer is unsaturated because of the precipitation. Then, a gap is formed because of no precipitation whilst the liquid is receding. The two-step process is one circle of an oscillation reaction. In short, the oscillation reaction produces nanoplatelets periodically, and continuous evaporation helps position the nanoplatelets into a fan-shaped periodic pattern with equal distance. The periodicity in this section is ~27 μm and larger than those from $CaCO_3$-PAA system[104, 117] and $BaSO_4$-block copolymer patterned thin films.[118] The reason is that the periodicity depends not only on the oscillation reaction but on the kinetics of the evaporation process.

The autocatalytic precipitation coupled with the diffusion of nanoplatelets with an evaporation process establishes a reaction-diffusion system that leads to fan-shaped patterns. The equal distanced fan-shaped patterns remind us of their similarity to the structure from the Belousov-Zhabotinsky type. However, modelling work is needed to be carried out. Some more experiments are still needed to investigate how the parameters, such as the solute concentration and the humidity affect the periodicity of self-organizing patterned thin films. In addition, WAXS measurement can be helpful to understand the orientation of the nanoplatelets within the thin film.

6.4 Preparation of L-Lys·HCl/PAA Thin Films

6.4.1 Spherulitic Thin Films

This section is designed to understand how the chemical structure affects the self-organization of the nanostructures and the final morphologies. The interactions between L-Lys·HCl (L-Lys) or DL-Lys·HCl and PAA should be similar. However, they result in thin films with differnt morphologies.

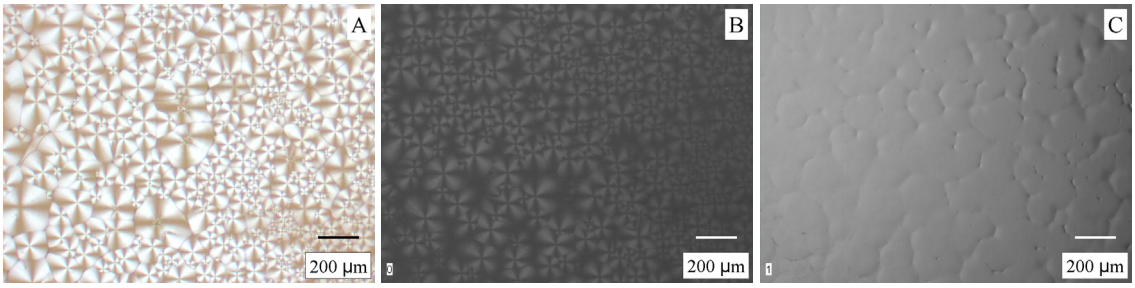

Fig. 6.4.1.1. Image **A** is a POM image, displaying the thin film during solvent evaporation (s**ample S**). Image **B** and **C** are OM and POM images of the as-prepared sample, respectively (**sample S**). Image **B** and **C** were taken at the same position.

The composition of L-Lys–PAA aqeuous solution is summarized in Table 6.4.1. For example, the newly formed spherulites show bright contrast in POM and each spherulite is from tens to hundreds of micrometers in size (Fig. 6.4.1.1A). The boundaries between spherulites are clear to see. However, the contrast begins to fade in several hours, as shown in Fig. 6.4.1.1B. Each spherulitic domain corresponds to a pattern in Fig. 6.4.1.1C. The solute concentration in L-Lys–PAA aquous solution is a key parameter for the preparation of thin films. If the solute concentration is lower than sample T, an incomplete thin film is obtained. Polycrystalline thin film forms when the solute concentration in the aqeuous solution is higher than in sample R (see section 6.4.2).

Table 6.4.1. The composition of aqueous solutions

	[L-Lys] ($g \cdot L^{-1}$)	[PAA] ($g \cdot L^{-1}$)
R	50	5
S	40	4
T	30	3

SEM images indicate the existence of sheet-like structures, covering the whole surface (Fig. 6.4.1.2A). A close scan of one spherulite shows that each spherulite is a nanosheet assembly in a radial arrangement (Fig. 6.4.1.2B). Nanosheets are more than 1 μm in length, and the thickness is less than 100 nm (Fig. 6.4.1.2C). Each nanosheet composes several 1D nanofibers arranging themselves in parallel.

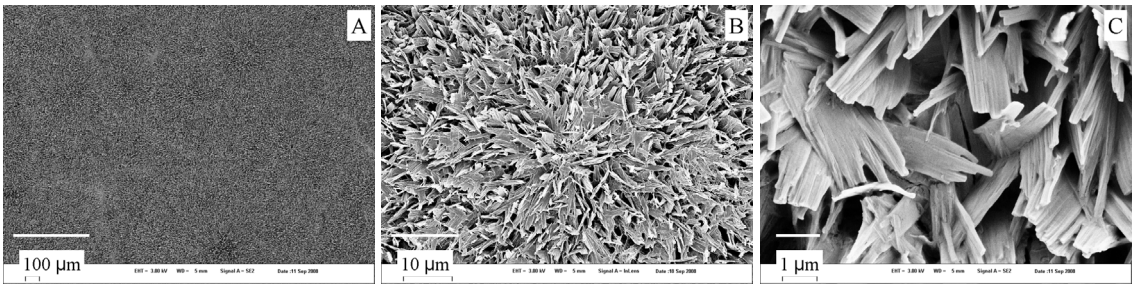

Fig. 6.4.1.2. SEM images of the structural details of sample S on different scales.

Compared to mesocrystalline thin films obtained from DL-Lys·HCl/PAA system (**Section 6.1**), L-Lys·HCl/PAA precipitates as spherulites with nanoplatelets as building blocks. In addition, both the composition and the interactions between the two systems are similar on molecular level. However, different crystallographic properties between L-Lys·HCl and DL-Lys·HCl decide the different morphologies of nanostructures and how nanostructures self-organize themselves, both of which cause the morphological difference between the two systems.

6.4.2 Hierarchical Thin Films

L-Lys·HCl/PAA thin films can also show hierarchical structures. A hierarchical thin film was scanned by SEM. Each domain is millimeters in size, as shown in Fig. 6.4.2.1A. The domain contains many slender structures, and each slender structure is about several micrometers in width and hundreds of micrometers in length (Fig. 6.4.2.1B). From Fig. 6.4.2.1C, each slender structure contains brick-like sub-structures, which lie in parallel along the growth direction of the slender structure. Each brick-like structure is assembled from NPs, which could only be observed by the fracture of the thin film (Fig. 6.4.2.1D).

Compared to four hierarchy levels observed in the DL-Lys·HCl/PAA thin film, only three hierarchies are obtained in the L-Lys·HCl/PAA thin film. One possibility is that the lamellar structures merge together to form brick-like structures. In **Section 6.2**, the wing or axis structure, which is comparable to a brick-like structure, remains as lamellar

assembly. We plan to use chiral thin films for chiral separation or chiral adsorptions. BET measurements are needed to clarify the porosity of thin films.

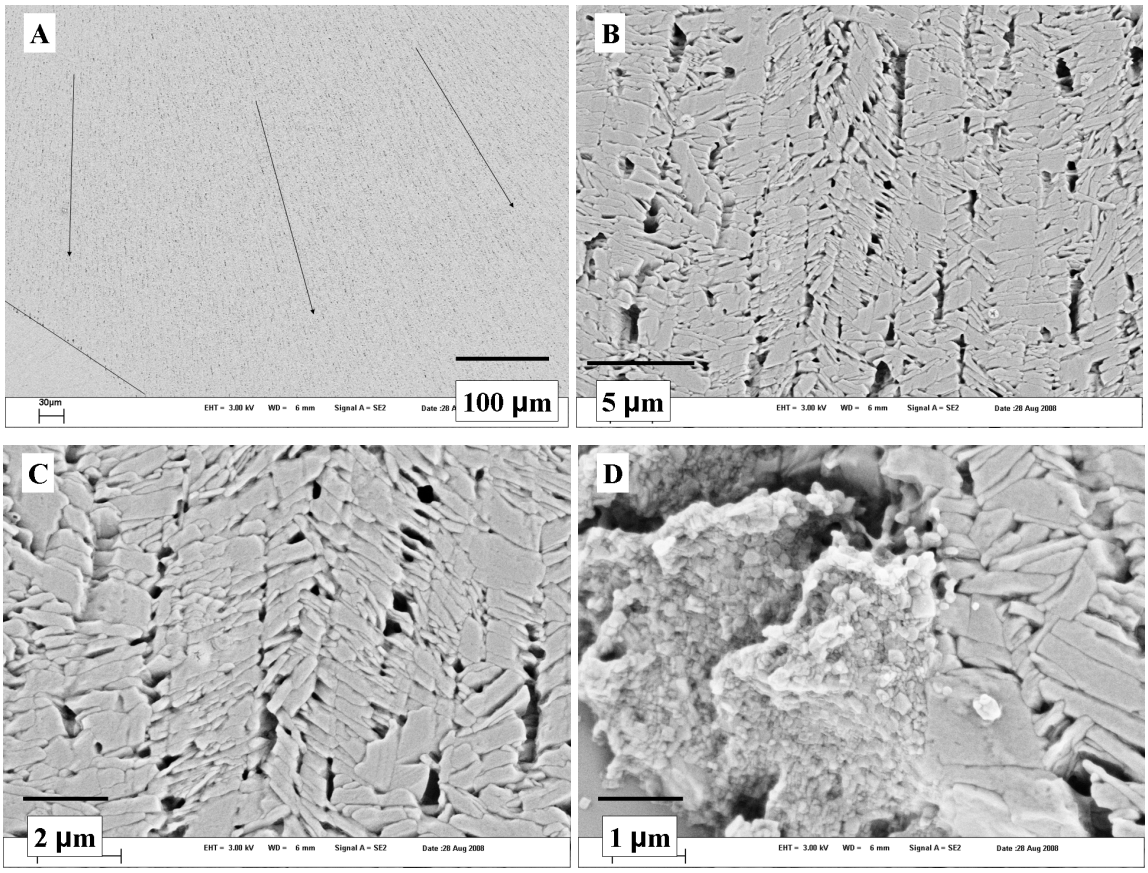

Fig. 6.4.2.1. SEM images of hierarchical thin films on different scales.

6.4.3 Discussion

As a comparison, L-Lys·HCl/PAA thin films were prepared as a comparison to DL-Lys·HCl/PAA thin films in **section 6.1** and **6.2**. Although continuous thin films were also obtained for the L-Lys·HCl/PAA system, they show spherulitic morphology with nanoplatelets as building blocks. Such results suggest that lattice energy and molecular structure plays key roles in determining the morphology of the building blocks and subsequently their self-organization, since interactions between L-Lys·HCl or DL-Lys·HCl and PAA at the molecular level are supposed to be the same whilst the lattice energies of L-Lys·HCl and DL-Lys·HCl are different. The preparation of such chiral hybrid thin films has numerous applications in chiral adsorption and separation science.

7. DL-Glu·H_2O 2D Nucleation and Growth from Nanoparticles Attachment and Relaxation

Abstract

Non-classical crystallization has become increasingly evident from studies in colloidal and protein systems and investigations in bio-inspired crystallizations and biomineral analysis experimentally or theoretically. This section presents the nucleation and growth of a molecular layer by nanoparticle (NP) attachments and relaxation as observed using in-situ atomic force microscopy (AFM). Liquid- or amorphous-like NPs attach to a preexisting molecular layer from the very beginning, followed by their shrinkage both in height and size to form crystalline seeds, which grow further to form a crystalline molecular layer by using the preexisting molecular layer as a template. Analytic ultracentrifugation (AUC) demonstrates the existence of clustering structures in the DL-Glu·H_2O solution system, which may be equal to or aggregate into NPs in the supersaturated solution. The nucleation of single crystal crystalline layers by liquid- or amorphous-like NP attachment and relaxation rather than the attachment of single molecules provides a strong proof for non-classical crystallization routes in molecular systems microscopically.

7.1 Introduction

Evidence from biomineral analysis,[76] bioinspired crystallization,[17, 22] protein crystallization,[4] and colloidal assembling[3, 6, 8] suggests that nucleation in crystallization is a multi-step process, namely non-classical crystallization. The simulation work by ten Wolde *et al.* pioneers the non-classical crystallization route by predicting the existence of a dense liquid precursor.[3] By passing through the critical point, proteins aggregate into a dense liquid phase by density fluctuation, instead of crystallizing by structural fluctuation in the classical pictures. Then, the highly reduced nucleation energy barrier results in the increase of the nucleation rate. Experimental studies of protein crystallization both in bulk solution and microscopically reach a similar conclusion, and provide strong evidence for the existence of liquid precursors before crystallization happens within the dense liquid phase. Most recently, a multi-step transition during an S layer protein assembly process passing through isolated molecules, amorphous clusters, and crystalline clusters was reported by using an in-situ atomic force microscope (AFM).[6] In the above study, however, the interferences from the conformation transformation of proteins and lipidic substrate effect cannot be excluded, both of which effects the generalization of the underling mechanism. Along with few successful cases in protein systems, proteins are very flexible and complex when used to mimic nucleation in molecular systems.

Colloidal assembly is always used as a supporting system for better understanding of nucleation in molecular crystallizations. The colloidal system is advantageous for the visibility to "see" each colloid from scattering under microscope, and its relatively slow transformation time which is usually from minutes to hours. The theory work shows nicely that hard-sphere colloidal clusters demonstrate a metastable structure, and they must transform into the same polymorph as bulk crystals before being used as nuclei.[8, 9] The above two-step route corresponds well with the Ostwald rule of stages. However, an experimental study provides another picture. Gasser *et al.* observed that initially formed clusters already show the thermodynamically stable hexagonal close-packed structures before they grow into 3D colloidal crystals by colloidal attachments, which follows classical nucleation theory exactly (CNT).[10] Besides the discordances between theoretic and experimental results, colloidal systems are not comparable to molecular ones for

several reasons. Monodisperse colloids are spherical with a homogeneous charge distribution. In addition, the hydration layer is thin compared to the size of colloids. On the contrary, molecules are asymmetric in morphology. Their charge distribution is inhomogeneous, and is affected heavily by solvent adsorption. Therefore, more complex colloids with anisotropic and various charging properties have been used for the nucleation study.

Precursors are also detected in (bio) mineralization systems. Clusters (~1 nm) during the nucleation of $CaCO_3$ by using a relatively slow diffusion method, gas diffusion, was detected by analytic ultracentrifugation (AUC)[22] and cryo-transmission electron microscopy (TEM),[23] separately. By directly mixing salts containing Ca^{2+} and CO_3^{2-}, however, a liquid-like phase was captured 100 ms after mixing.[15] In both cases, amorphous and crystalline $CaCO_3$ can be obtained thereafter in sequence. But, due to experimental limitations associated with viewing nucleation in 3D with a resolution on a molecular level, a multi-step nucleation picture in molecular systems is still lacking. Here, a 2D AFM observation of DL-Glu·H_2O nucleation and growth via nanoparticle (NP) attachments and relaxation is presented. The shrinkage of NP size to a minimum value accompanies the disappearance of NPs smaller than the critical value. Simultaneously, the size decrease of NP is followed by the nucleation of crystalline seeds, which serve as nuclei for the growth of new crystalline molecular layers. This section provides the experimental observation of multi-step nucleation in molecular systems microscopically.

7.2 Results

A small DL-Glu·H_2O crystal was immersed into a supersaturated DL-Glu aqueous solution, and the changes on the crystal surface were detected by an AFM tip. Fig. 7.1A presents a series of representative AFM images collected with time. Since AFM can only provide the height information of NPs, Fig. 7.1B records the height change NPs with time.

The first 15 min sees the height increase in NPs. The height of the black, blue, and green NPs increases during the first 9 min and it keeps almost constant during the next 6 min. However, the height of other circled NPs fluctuates during the first 9 min, and reaches their peak value at 15 min. The height increase of NPs in the supersaturated

mother liquor can be attributed to the NP reorientation or growth due to molecule or cluster attachment.

The height shrinkage of NPs was observed in the next 11 min. The height of NPs (blue, black, yellow, and red NPs) shrinks from ~3-7 nm to ~1-3 nm, whilst small NPs (green, orange, purple, and other small NPs) disappear. This result suggests the existence of the critical height of NPs. Considering there is a shrinkage process, the critical height is not a constant, but varies with time. For example, the red NP height at ~3.5 nm is suggested as the critical height at the 15th min. At this moment, only NPs higher than this value can stay as nuclei. In addition, the height order is changing before and after the shrinkage period. For example, the black NP has the largest height at the 15th min. However, its height is smaller than the other six NPs at the 26th min.

As to the purple and red NPs, which are close in height, the purple NP disappears whilst the red one shrinks to ~2 nm. One possible explanation is that the purple NP is very close to the blue one. During the NP shrinkage, there might be a direct mass transfer between the purple and blue NPs, which is an Ostwald Ripening process on the nanoscale. As to the red NP, it may even obtain masses from the surrounding NPs.

The shrinkage can be attributed to a relaxation process with mass transfers between NP and NP as well as between NP and the mother liquor. The height of NPs before the shrinkage is much larger than that of a molecular layer (~0.4 nm). In addition, the NP surface is smooth from a 3D analysis without any discontinuous height gradient (image not shown). Therefore, NPs before the shrinkage are liquid- or amorphous- like, and may contain water and DL-Glu·H_2O molecules. Kuznetsov *et al.* also mentioned that the liquid droplets rich in proteins can adsorb on the crystal surface, and crystallize into multilayer layers.[122] NPs after the shrinkage begin to grow in parallel with the preexisting molecular layer. The relaxation process may combine with the expelling of water and DL-Glu·H_2O molecules, which is entropically beneficial to the ordering of the remaining DL-Glu·H_2O molecules.[123]

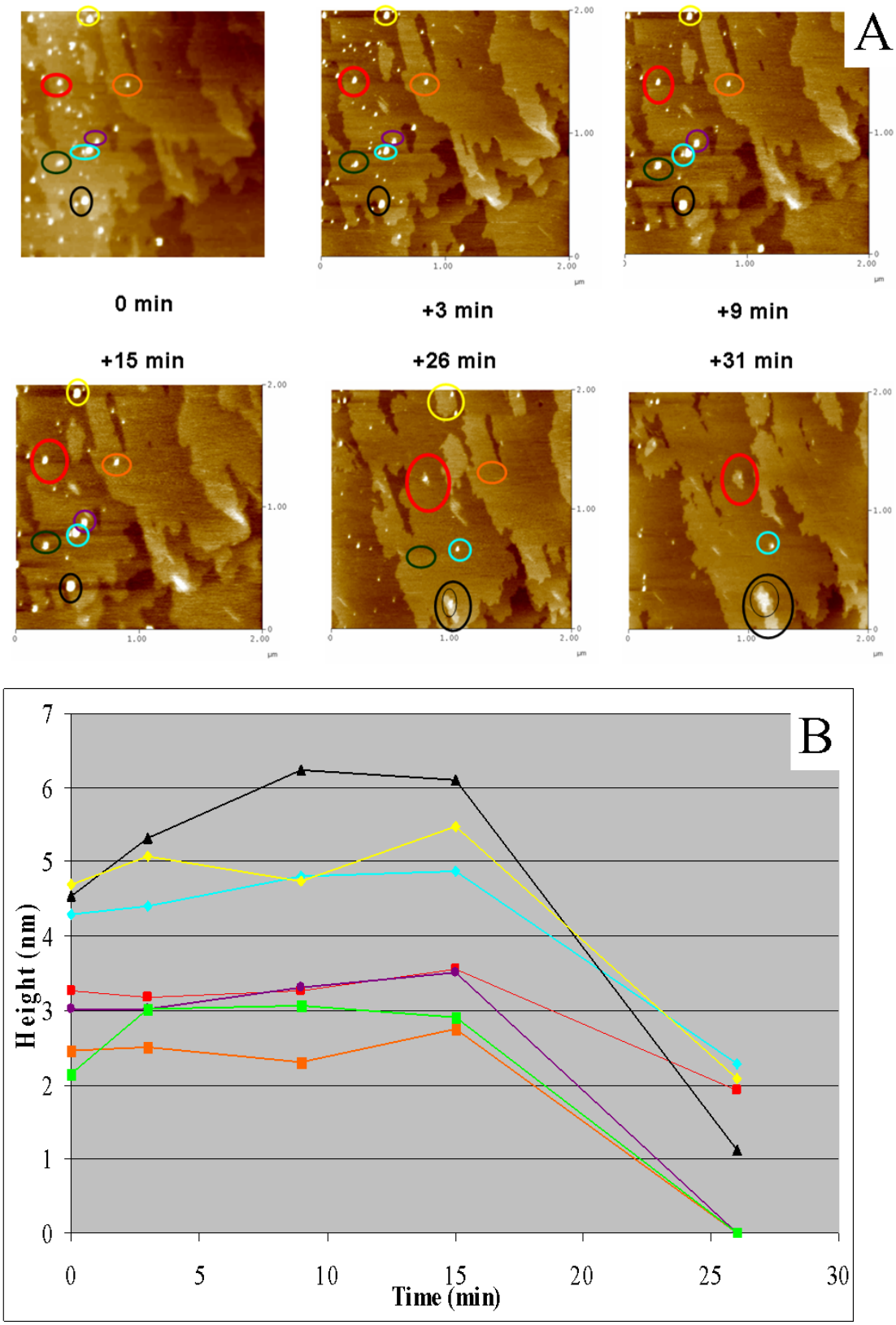

Fig. 7.1. Image **A** is a series of AFM images with time. Each AFM image is 2 μm in size. Seven NPs were picked out to track the height change of NPs, which is summarized in image **B**.

The next step is the growth of molecular layers, as summarized in Fig. 7.2. To begin with, Fig. 7.1 must be returned to. As to the red NP, its transformation into a crystalline layer begins to be visible in the +26 image in Fig. 7.1A. In the +31 image in Fig. 7.1A, the new layer is already 100 nm in size with a flat surface. However, the single layer growth mode is not the only mode, as shown in Fig. 7.2. For example, the black NP grows into a double crystalline layer. The growth of a double layer is observed until the 37th min. Then, the layer on top disappears within the next 10 min. The disappearance of the top layer of the double layer for the NP within the black circle suggests that crystals grow by completing discrete unit cells rather than filling cells here and there on the layers.[124]

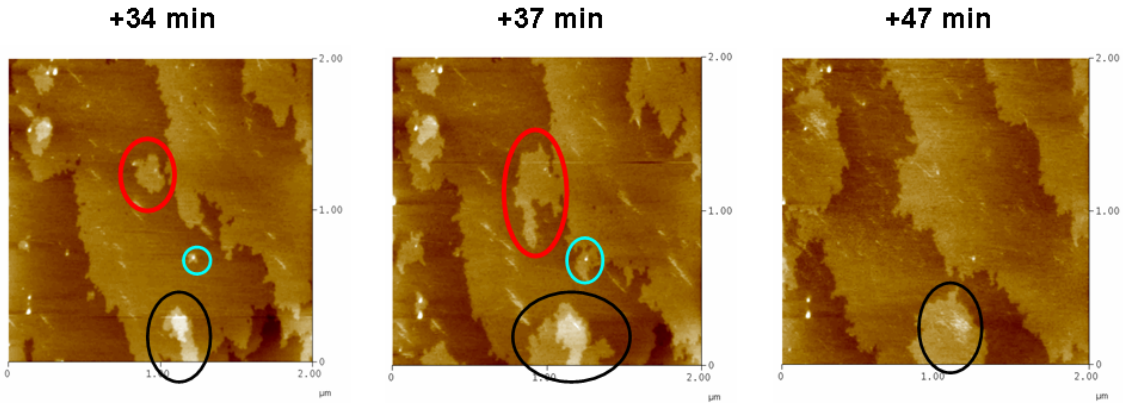

Fig. 7.2. Three AFM images in sequence show the growth of new layers.

A simple control experiment proves that NPs originate from the solution. The existence of NPs was observed to deposit on a Si wafer within a DL-Glu supersaturated solution. However, there is no NP on a dry Si wafer or the wafer immersed into water, as shown in Fig. 7.3. Therefore, NPs must come from Glu supaersaturated solution. However, these small NPs are transient, and can disappear in the next scan (each scan takes 3 min).

Large NPs, however, can stay at the same position for a continuous scanning. In Fig. 7.4, the height change of a NP is illustrated. The first 10 min is the NP fluctuation period. Then, the next 20 min sees a continuous height decrease from 12 to 2 nm, which is a relaxation process. The final NP height drops to 1 nm, and the value keeps constant thereafter. The growth of a new molecular layer is not observable, which may be

attributed to the unit cell mismatch between DL-Glu·H_2O and Si. However, the structural details of the attached NPs are impossible to scan because of the limit of size resolution in AFM.

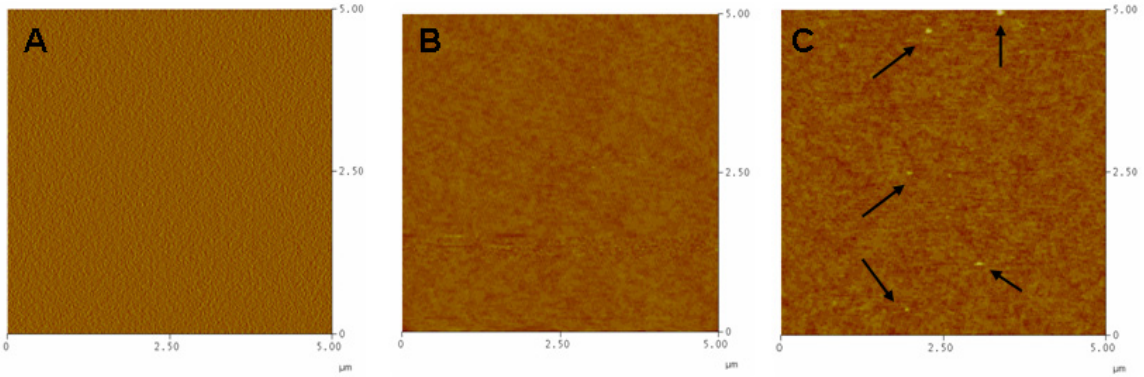

Fig. 7.3 AFM images **A**, **B** and **C** was taken at the same area in air, in double distilled water, and in a DL-Glu supersaturated aqueous solution, respectively. Each image is 5 µm in size.

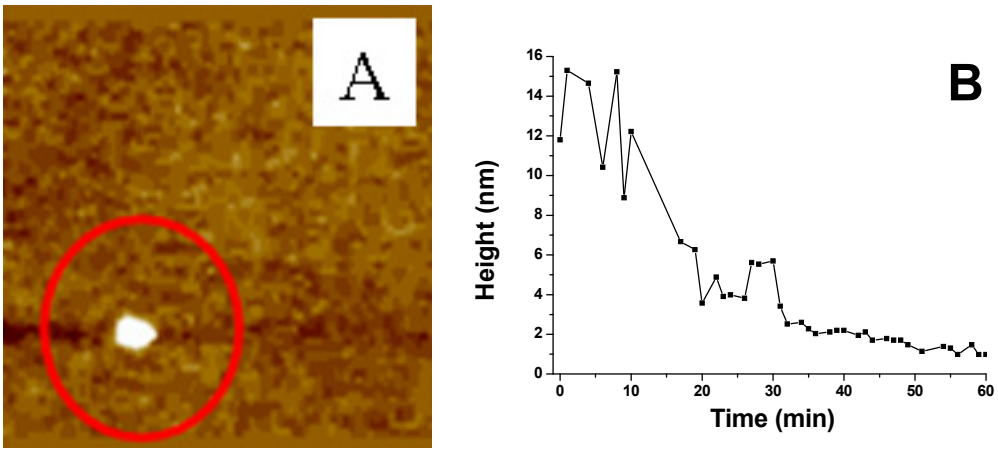

Fig. 7.4. Image **A** is an AFM image taken at 60 min. The image is 2.5 µm in size. The height change of the NP is summarized in image **B**.

The existence of DL-Glu·H_2O clusters in a 2g·L^{-1} aqueous solution was proven by AUC. By calculating the sedimentation coefficient, the diameter of the clusters is estimated to be 2.1±0.1 nm based on the density of DL-Glu·H_2O. The AUC result shows that pre-nucleation clusters can exist even in the unsaturated solution, which suggests that the threshold value for the appearance of clusters does not depend on the saturation value of monomers. The existence of a strong convection blocked the possibility to measure clusters in more concentrated samples. However, it is expected that cluster number density increases with the increase of monomer concentration, supposing that the size of

NPs is constant with the monomer concentration. The actual cluster size may be larger than 2.1±0.1 nm, because the possible existence of solvent can loosen the structure. Therefore NPs observed in AFM should be clusters or cluster aggregates.

Measurements in mass spectroscopy, cryo-TEM, SANS, SAXS, and light scattering are still unsuccessful in scanning the existence of clusters in DL-Glu·H_2O supersaturated solution so far. Therefore, it is still difficult to conclusively back up the described mechanism by a second analytical technique.

7.3 Discussion

The 2D nucleation and growth of a molecular layer can be divided into three steps: NP formation & attachment, NP relaxation, and the growth of newly formed molecular layers, which will be discussed in sequence. The whole process is summarized in Fig. 7.5.

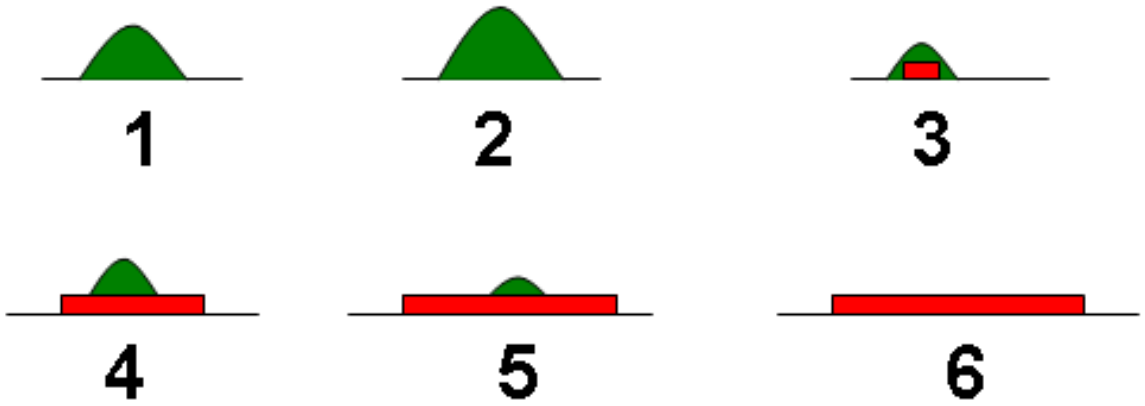

Fig. 7.5. A series of cartoons show the relaxation of a NP in a supersaturated solution. An amorphous or liquid-like NP is shown in green. The red layer represents one molecular layer and the preexisting molecular layer is shown as a black line.

NP formation & attachment is a transient process, which is difficult to capture by AFM and other techniques. Therefore, two routes have been applied to provide indirect proofs that the attached NPs come from solution. Firstly, NPs were observable by dipping supersaturated DL-Glu solution on a Si wafer, which directly proves their existence in mother liquor. Secondly, AUC measurements detected the existence of prenucleation clusters ~2 nm in diameter in an unsaturated DL-Glu solution. NPs can be clusters or their aggregates in the supersaturated solution. When the crystal is immersed in the mother liquor, NPs immediately attach to the crystal layer to lower their interfacial

energy. Molecular layer growth by NP attachments have also been observed in inorganic[125] and macromolecular crystallizations.[124, 126] However, former research failed to provide details of NP transformation into molecular layers.

Considering that the height of initial NPs (several nanometers) is obviously larger than that of a molecular layer (~0.4 nm), there will be a relaxation process for NPs to fit their height and structure to the level of a molecular layer. The size shrinkage has been observed elsewhere during the coarsening of crystalline NPs, where the coarsening NPs change shape or lose monomers to decrease the internal energy and chemical potential.[24, 127] However, in both cases, the decrease in size during the crystalline NP coarsening process is slight. Here, a large portion of NP size (or volume) is lost. A possible explanation is provided as follows. The attached NPs are amorphous- or liquid-like in nature with the existence of water molecules. The following relaxation process is a crystallization process of the remaining solute molecules, combined with the expelling of solute and solvent from NPs. This process is an entropically beneficial process. The relaxation can be realized in several other ways in other systems. For example, the structural transformation of S-layer proteins from an amorphous to crystalline phase was reported, where the condensation and relaxation were realized from conformational transformation of proteins.[6] In another case, simulation results showed that during the nucleation of colloidal crystals with oppositely charged colloids, there was a phase transformation from the initially formed liquid-or amorphous-like clustering structures to the crystalline nuclei, which continued growing into colloidal crystals.[9] The phenomena of relaxation are various and depend heavily on the system, such as the molecule, reaction condition, *etc.* The relaxation is the rate-determining step in multi-step nucleation processes.

The shrinkage process sees the disappearance of small NPs, which proves the existence of the critical height during the relaxation process. Similar results have been observed elsewhere in protein crystallization with AFM.[128] The critical height herein is different from the critical nucleus in CNT for several reasons. In CNT, the crystalline critical nucleus exists in a solution, and is a constant value in size. Herein, the critical height is variable during the relaxation process.

The pre-existing molecular layer can act as a template for the growth of new layers. It can provide the orientation for the molecular patterning, and lower the interfacial energy during the relaxation. This explanation can also explain why NPs on a Si wafer fail in growing into a molecular layer. Therefore, a succession of mass transfers changes the internal NP structure, and a multi-step process is advantageous for lowering the activation energy of nucleation. In addition, the release of solvents as well as some solute during nucleation is beneficial for the formation of densely packed nuclei from an entropic point of view.

8. Summary of the Thesis & Outlook

To precisely control the size, morphology, and polymorph of crystals is the ultimate goal in the crystallization science. A series of nucleation and crystallization theories have been put forward to understand the underlying physical mechanism of crystallization. Although crystallization is well understood from a phenomenological perspective, current theories are still far from being satisfactory in explaining many phenomena in crystallization. Evidence in biomineralization and colloidal assembly challenges classical crystallization theories, suggesting insights to the physical mechanisms on the nano- and micro-scale to facilitate the rational synthesis of high-quality crystals.

The primary objective of this thesis is to understand crystallization as a multi-step process, which passes through the formation of precursor phases on the nanoscale, the relaxation of the precursor phase into crystalline nanostructures, and the aggregation of nanocrystals (with polymeric additives) or the recrystallization into bulk crystals (without polymeric additives) on the micro- and macro-scale. The main emphasis of this thesis is on the precipitation of organics with a polymeric additive by addition of a non-solvent, but also on the crystallization of organics by a temperature drop. In particular, the multi-step crystallization is pursued to create materials such as porous microspheres and patterned thin films.

Chapter 4 provides the phase behavior of a quaternary DL-Glutamic acid (Glu)–polyethyleneimine (PEI)–water–EtOH system. The presented model system is used to aid a description of interactions between the target molecules and oppositely charged polyelectrolytes, and in turn how this interaction influences the phase behavior of such a quaternary system. It is found that these interactions can effectively be tuned by varying Glu/PEI w/w and the solvent components, resulting in precipitation from a polymer-induced liquid precursor (PILP), coacervation or the formation of homogeneous mixtures. Coacervation is observed to occur over a wide range of Glu/PEI with various volumes, and the composition of coacervates is characterized by NMR. Different from metastable liquid precursors in the precipitation of Glu, coacervates are a thermodynamically stable phase rich in solute as proven by the path independence of reaching a thermodynamic equilibrium. Therefore, thermodynamically stable coacervates have to be distinguished

from metastable PILP phase as the latter is relatively difficult to handle due to its transient properties. In the second part of this chapter, the Glu-PEI aqueous solution is characterized. The combination of atomic force microscopy, small angle scattering, and ξ-potential measurements confirms the coexistence of monomers and Glu/PEI complexes and the aggregates of complexes. This case study reveals that the existence of preexisting complexes is the prerequisite for the formation of liquid precursors in the precipitation processes, and that there might be a direct structural transformation between the Glu/PEI complexes in aqueous solution and the metastable liquid precursors in a water-EtOH mixture.

The next chapter concerns the mechanism of Glu precipitation with PEI as an additive. The experiments are performed by mixing Glu-PEI aqueous solution with a non-solvent – EtOH. The results presented herein support the hypothesis that the precipitation of organic compounds bearing an opposite charge to the polyelectrolyte additive is a multi-step process starting with a liquid-liquid (L-L) phase separation. The combination of stopped flow and small angle scattering demonstrates that the initially formed liquid precursors pass through an alteration of growth and coalescence before the nucleation of nanoplatelets within them. The nucleation period of liquid precursors is as such a fast process, and is beyond the limit of data collection. Therefore, the possibility of a very rapid L-L phase separation being spinodal in nature followed by a binodal phase separation cannot be discounted, or likewise a binodal process from the very beginning due to the fast mass diffusion in solution compared to polymer blends cannot be ruled out. In the following step, the coalescent PILP droplets grow into spherical PILP superstructures to lower their interfacial energies. The nucleation of nanoplatelets happens within each PILP droplet thereafter. Finally, nanoplatelets reorient themselves, and self-organize in a radial direction into the final crystalline microspheres. Therefore, the precipitation of Glu with PEI as an additive is a multi-step process, including a liquid-liquid phase separation, the nucleation of nanostructures, and the self-organization of nanostructures. The existence of PEI changes the precipitation of Glu to start from a metastable L-L phase separation, which can highly decrease the nucleation barrier and accelerate the rate of precipitation. The results presented here agree well with those from protein and colloidal crystallization. The recipe was then extended to the precipitation of

organics in other oppositely charged amino acid-polyelectrolyte systems, which suggests that the multi-step mechanism is general with regard to the precipitation of organics with an oppositely charged polymer additive. The liquid precursor routes can shape the polymer controlled inorganic crystallization or the precipitation of organics for the better understanding of biomineralization and for designing functional bio-inspired inorganic- and organic-polymer hybrid materials.

In Chapter 6, the multi-step crystallization route is extended to the preparation of patterned thin films in combination with an evaporation process. By dipping a quaternary DL-Lys·HCl (Lys)–polyacrylic acid (PAA)–water–EtOH dispersion on a hydrophilic slide, the solvent evaporation induces precipitation and the formation of a thin film in sequence. Different from the generally accepted surface-induced heterogeneous nucleation route, from which single crystalline domains are always formed, nanoparticle-based mesocrystalline thin films are obtained instead. The fast evaporation process caused by the volatile solvent EtOH is responsible for the homogeneous nucleation of NPs. Then, the following complete evaporation causes the mesocrystallization of a continuous spherulitic thin film along the receding line of the liquid, which again transforms into a mesocrystalline thin film. Furthermore, annealing is used to optimize the property of the mesocrystalline thin films. The dipole-dipole interactions between neighbouring NPs provide the orientation forces for the formation of mesocrystalline domains. The multi-step formation of mesocrystalline thin films is advantageous for obtaining large area crack-free thin films. As evaporation is a non-equilibrium process, it can be used to tune the kinetics of crystallization. Therefore, hierarchical or periodical thin films can be formed by starting the evaporation from the recrystallization of microspheres. This is the first report for the preparation of mesocrystalline thin films with four hierarchy levels by using bottom-up approaches on a free-standing slide. The results reveal that evaporation provides an easy but effective way for the formation of patterned structures on the micro- and macro-scale on a free standing solid surface via the positioning of NPs after their fast nucleation, resulting in different kinds of patterns. This is possible by controlling the concentration of NPs, solvent evaporation rate, and other physical forces. Spherulitic L-Lys·HCl–PAA thin films are prepared as a comparison to DL-Lys·HCl analogues, suggesting that the morphology also depends heavily on the

lattice energy, since the molecular interactions between DL-Lys·HCl or L-Lys·HCl and PAA are the same, whilst the lattice energies of DL-Lys·HCl or L-Lys·HCl are different. To rationally control the lattice energy of the target crystals, the interactions between ions and polymeric additives in combination with the processing route can be a productive and general way to prepare high quality biomimetic thin films.

Non-classical crystallizations are not limited to crystallizations with oppositely charged polymers as additives. Chapter 7 concerns the nucleation and growth of a new molecular layer on the growing DL-Glu·H_2O crystals from a supersaturated mother liquor by using in-situ atomic force microscopy (AFM). There is no observation of the growth on the preexisting molecular layers by a molecular attachment. Instead, the nucleation and growth of a molecular layer proceed via a nanoparticle (NP) attachment and relaxation process, before the observation of the growth of a newly formed molecular layer. Since NP attachment to the crystal surface is too fast to observe by using in-situ AFM, two indirect proofs for the existence of NPs in the mother liquor are provided as follows. Analytical ultracentrifugation proves the existence of clusters even in the unsaturated mother liquor; the attachment and relaxation of NPs on a silicon wafer is observed within the mother liquor. Therefore, NPs (~2-6 nm) are attributed to the clusters (~2 nm) or cluster aggregates according to their different sizes. Both the smooth surface of NPs and their lack of height steps reveal that NPs are amorphous in nature. Although the growth of a molecular layer by NP attachment has been reported elsewhere such as in protein crystallization systems, the details of the structural transformation from NPs to crystalline molecular layers are still lacking. As revealed in this thesis, the height shrinkage of NPs, combined to the structural transformation from 3D amorphous-like NPs to 2D crystalline nuclei, is observed during the relaxation process. During this period, small NPs disappear, which proves the existence of a critical height of NPs. The nucleation and growth of a newly formed molecular layer from NP relaxation is contradictory to the classical nucleation theory, which hypothesizes that the nuclei show the same crystallographic properties as the bulk crystals. Different from theoretical or simulating predictions, which suggest a transient structural transformation during molecular crystallization, experimental results herein prove that the relaxation is the rate-determining step, and is possibly long enough for time-resolved characterization such as

AFM. The relaxation can be realized by conformational transformation in protein assembly or by size shrinkage in the current molecular system. The formation of a molecular layer by NP attachment and relaxation (e.g. clusters, liquids, amorphous materials, or nanocrystals) rather than attachment of single molecules provides a different picture from the currently held classical nucleation theory regarding the growth of single crystals from solution.

There are plenty opportunities alongside with the extremely difficult technical bottlenecks and theoretical limits within the understanding of multi-step crystallizations. Several experimental routes are suggested as follows to advance the understanding of the rational design of functional materials.

1. Understanding Crystallization from Colloidal Assembly

Colloidal assembly is a supporting system to mimic nucleation in molecular crystallizations. Colloids, especially anisotropic ones with inhomogeneous charge distributions, are preferred to mimic molecular crystallization because molecules are often anisotropic with asymmetric charge distributions. In addition, biomacromolecules, nanocrystals, and even carbon fullerenes are closer to molecules in size, and their surface properties can be tuned conveniently by chemical modification or adsorption. Therefore, studying their assembly by using AFM and small angle scattering is a promising route to find more details for the better understanding of nucleation in molecular crystallization systems.

2. Rational Selection, Design, and Ordering of Polyelectrolytes

To rationally understand the interactions between polyelectrolyte functional groups and organic molecules, phage display selection can be used to find out those peptides, which interact effectively with organic crystals. Then, artificial peptides can be synthesized and used as additives for precipitation of organics. Furthermore, artificial peptides or polyelectrolytes can be grafted to the surface to form patterned structures on the micro- or nano-scale, which can be used as templates for the selective growth of nanocrystals.

3. Biomimetic Thin Films

A biomimetic route is an effective way to introduce hierarchy into thin films on a free standing surface. Future work will focus on the preparation of biomimetic thin films with unique orientation by using insoluble polymer matrices as substrates. In addition, lithography and patterning can be combined to precisely control the nucleation points in grains. To find forces which can provide the order across microscale and macroscale is also meaningful for the design of patterned thin films.

9. References

1. Volmer, M., *Kinetik der Phasenbildung*. Steinkopff: Dresden u. a., 1939; p 220.
2. Ostwald, W., Studien über die Bildung und Umwandlung fester Körper. *Zeitschrift für Physikalische Chemie* **1897,** 22, 289–330.
3. ten Wolde, P. R.; Frenkel, D., Enhancement of protein crystal nucleation by critical density fluctuations. *Science* **1997,** 277, (5334), 1975-1978.
4. Galkin, O.; Vekilov, P. G., Control of protein crystal nucleation around the metastable liquid-liquid phase boundary. *Proceedings of the National Academy of Sciences of the United States of America* **2000,** 97, (12), 6277-6281.
5. Vekilov, P. G., Dense liquid precursor for the nucleation of ordered solid phases from solution. *Crystal Growth & Design* **2004,** 4, (4), 671-685.
6. Chung, S.; Shin, S.-H.; Bertozzi, C. R.; De Yoreo, J. J., Self-catalyzed growth of S layers via an amorphous-to-crystalline transition limited by folding kinetics. *Proceedings of the National Academy of Sciences* **2010,** 107, 16536-16541.
7. Aasland, S.; McMillan, P. F., DENSITY-DRIVEN LIQUID-LIQUID PHASE-SEPARATION IN THE SYSTEM AL2O3-Y2O3. *Nature* **1994,** 369, (6482), 633-636.
8. Auer, S.; Frenkel, D., Prediction of absolute crystal-nucleation rate in hard-sphere colloids. *Nature* **2001,** 409, (6823), 1020-1023.
9. Sanz, E.; Valeriani, C.; Frenkel, D.; Dijkstra, M., Evidence for out-of-equilibrium crystal nucleation in suspensions of oppositely charged colloids. *Physical Review Letters* **2007,** 99, (5), 055501/1-055501/4.
10. Gasser, U.; Weeks, E. R.; Schofield, A.; Pusey, P. N.; Weitz, D. A., Real-space imaging of nucleation and growth in colloidal crystallization. *Science* **2001,** 292, (5515), 258-262.
11. Mann, S., *Biomineralization. Principles and Concepts in Bioinorganic Materials Chemistry*. Oxford Univ. Press: New York, 2001.
12. Cölfen, H.; Antonietti, M., *Mesocrystals and Nonclassical Crystallization*. John Wiley & Sons Ltd: 2008.
13. Wang, T. X.; Colfen, H.; Antonietti, M., Nonclassical crystallization: Mesocrystals and morphology change of CaCO3 crystals in the presence of a polyelectrolyte additive. *Journal of the American Chemical Society* **2005,** 127, (10), 3246-3247.
14. Inumaru, K.; Nakajima, H.; Ito, T.; Misono, M., Porous aggregates of unidirectionally oriented (NH4)(3)PW12O40 microcrystallites: Epitaxial self-assembly. *Chemistry Letters* **1996**, (7), 559-560.
15. Navrotsky, A., Energetic clues to pathways to biomineralization: Precursors, clusters, and nanoparticles. *Proceedings of the National Academy of Sciences of the United States of America* **2004,** 101, (33), 12096-12101.
16. Rieger, J.; Frechen, T.; Cox, G.; Heckmann, W.; Schmidt, C.; Thieme, J., Precursor structures in the crystallization/precipitation processes of CaCO3 and control of particle formation by polyelectrolytes. *Faraday Discussions* **2007,** 136, 265-277.
17. Gower, L. B.; Odom, D. J., Deposition of calcium carbonate films by a polymer-induced liquid-precursor (PILP) process. *Journal of Crystal Growth* **2000,** 210, (4), 719-734.
18. de Kruif, C. G.; Weinbreck, F.; de Vries, R., Complex coacervation of proteins and anionic polysaccharides. *Current Opinion in Colloid & Interface Science* **2004,** 9, (5), 340-349.
19. Mullin, J. W.; Leci, C. L., EVIDENCE OF MOLECULAR CLUSTER FORMATION IN SUPERSATURATED SOLUTIONS OF CITRIC ACID. *Philosophical Magazine* **1969,** 19, (161), 1075-&.
20. Stradner, A.; Sedgwick, H.; Cardinaux, F.; Poon, W. C. K.; Egelhaaf, S. U.; Schurtenberger, P., Equilibrium cluster formation in concentrated protein solutions and colloids. *Nature* **2004,** 432, (7016), 492-495.

21. Shukla, A.; Mylonas, E.; Di Cola, E.; Finet, S.; Timmins, P.; Narayanan, T.; Svergun, D. I., Absence of equilibrium cluster phase in concentrated lysozyme solutions. *Proceedings of the National Academy of Sciences of the United States of America* **2008,** 105, (13), 5075-5080.
22. Gebauer, D.; Völkel, A.; Cölfen, H., Stable Prenucleation Calcium Carbonate Clusters. *Science* **2008,** 322, (5909), 1819-1822.
23. Pouget, E. M.; Bomans, P. H. H.; Goos, J.; Frederik, P. M.; de With, G.; Sommerdijk, N., The Initial Stages of Template-Controlled CaCO3 Formation Revealed by Cryo-TEM. *Science* **2009,** 323, (5920), 1555-1458.
24. Zheng, H. M.; Smith, R. K.; Jun, Y. W.; Kisielowski, C.; Dahmen, U.; Alivisatos, A. P., Observation of Single Colloidal Platinum Nanocrystal Growth Trajectories. *Science* **2009,** 324, (5932), 1309-1312.
25. Imai, H., Self-organized formation of hierarchical structures. In *Biomineralization I: Crystallization and Self-Organization Process*, Springer-Verlag Berlin: Berlin, 2007; Vol. 270, pp 43-72.
26. Penn, R. L.; Banfield, J. F., Imperfect oriented attachment: Dislocation generation in defect-free nanocrystals. *Science* **1998,** 281, (5379), 969-971.
27. Palermo, V.; Samori, P., Molecular self-assembly across multiple length scales. *Angewandte Chemie-International Edition* **2007,** 46, (24), 4428-4432.
28. Aizenberg, J.; Weaver, J. C.; Thanawala, M. S.; Sundar, V. C.; Morse, D. E.; Fratzl, P., Skeleton of Euplectella sp.: Structural hierarchy from the nanoscale to the macroscale. *Science* **2005,** 309, (5732), 275-278.
29. Horn, D.; Rieger, J., Organic nanoparticles in the aqueous phase - theory, experiment, and use. *Angewandte Chemie-International Edition* **2001,** 40, (23), 4331-4361.
30. Gibbs, J. W., In *The Collected Works of J.W. Gibbs*, Yale Univ. Press: New Haven, 1948.
31. Becker, R.; Döring, W., Kinetic treatment of germ formation in supersaturated vapour. *Annalen der Physik* **1935,** 24, (8), 719-752.
32. Sear, R. P., Nucleation: theory and applications to protein solutions and colloidal suspensions. *Journal of Physics: Condensed Matter* **2007,** 19, (3), 033101.
33. Oswald, H. R.; Feitknecht, W.; Brunner, P. In *Applicazioni della microscopia e della differazione elettronica alla chimica inorganica: La ossidazione dell'idrossido(II) di manganese con l'ossigeno molecolare.* , From Molecule to Cell: Symposium on Electron Microscopy, Roma, 1963; Buffa, P., Ed. CNR: Roma, 1963; pp 141-160.
34. Talanquer, V.; Oxtoby, D. W., Crystal nucleation in the presence of a metastable critical point. *Journal of Chemical Physics* **1998,** 109, (1), 223-227.
35. Smoluchowski, M. V., Versuch einer mathematischen Theorie der koagulationskinetik kolloider sösungen. *Z Phys Chemie* **1918,** 92, 129-168.
36. Söhnel, O.; Garside, J., *Precipitation - Basic principles and industrial applications*. Butterworth-Heinemann Ltd: 1992.
37. Ostwald, W., *Lehrbuch der Allgemeinen Chemie*. Leipzig, Germany., 1896; Vol. 2.
38. Lamer, V. K.; Dinegar, R. H., THEORY, PRODUCTION AND MECHANISM OF FORMATION OF MONODISPERSED HYDROSOLS. *Journal of the American Chemical Society* **1950,** 72, (11), 4847-4854.
39. Lin, M. Y.; Lindsay, H. M.; Weitz, D. A.; Ball, R. C.; Klein, R.; Meakin, P., UNIVERSALITY IN COLLOID AGGREGATION. *Nature* **1989,** 339, (6223), 360-362.
40. Cahn, J. W.; Hilliard, J. E., FREE ENERGY OF A NONUNIFORM SYSTEM .1. INTERFACIAL FREE ENERGY. *Journal of Chemical Physics* **1958,** 28, (2), 258-267.
41. Cahn, J. W.; Hilliard, J. E., FREE ENERGY OF A NONUNIFORM SYSTEM .3. NUCLEATION IN A 2-COMPONENT INCOMPRESSIBLE FLUID. *Journal of Chemical Physics* **1959,** 31, (3), 688-699.
42. Cahn, J. W., ON SPINODAL DECOMPOSITION. *Acta Metallurgica* **1961,** 9, (9), 795-801.

43. Binder, K.; Stauffer, D., STATISTICAL-THEORY OF NUCLEATION, CONDENSATION AND COAGULATION. *Advances in Physics* **1976,** 25, (4), 343-396.
44. Cook, H. E., BROWNIAN MOTION IN SPINODAL DECOMPOSITION. *Acta Metallurgica* **1970,** 18, (3), 297-&.
45. Langer, J. S.; Baron, M.; Miller, H. D., NEW COMPUTATIONAL METHOD IN THEORY OF SPINODAL DECOMPOSITION. *Physical Review A* **1975,** 11, (4), 1417-1429.
46. Hillert, M., ON THEORY OF NORMAL AND ABNORMAL GRAIN GROWTH. *Acta Metallurgica* **1965,** 13, (3), 227-&.
47. Thompson, C. V., GRAIN-GROWTH IN THIN-FILMS. *Annual Review of Materials Science* **1990,** 20, 245-268.
48. Thompson, C. V., SECONDARY GRAIN-GROWTH IN THIN-FILMS OF SEMICONDUCTORS - THEORETICAL ASPECTS. *Journal of Applied Physics* **1985,** 58, (2), 763-772.
49. Binnig, G.; Quate, C. F.; Gerber, C., ATOMIC FORCE MICROSCOPE. *Physical Review Letters* **1986,** 56, (9), 930-933.
50. Roiter, Y.; Minko, S., AFM single molecule experiments at the solid-liquid interface: In situ conformation of adsorbed flexible polyelectrolyte chains. *Journal of the American Chemical Society* **2005,** 127, (45), 15688-15689.
51. van de Hulst, H. C., *Light Scattering by Small Particles*. John Wiley: 1957.
52. Raz, S.; Weiner, S.; Addadi, L., Formation of high-magnesian calcites via an amorphous precursor phase: Possible biological implications. *Advanced Materials* **2000,** 12, (1), 38-+.
53. Addadi, L.; Raz, S.; Weiner, S., Taking advantage of disorder: Amorphous calcium carbonate and its roles in biomineralization. *Advanced Materials* **2003,** 15, (12), 959-970.
54. Olszta, M. J.; Cheng, X. G.; Jee, S. S.; Kumar, R.; Kim, Y. Y.; Kaufman, M. J.; Douglas, E. P.; Gower, L. B., Bone structure and formation: A new perspective. *Materials Science & Engineering R-Reports* **2007,** 58, (3-5), 77-116.
55. Homeijer, S. J.; Barrett, R. A.; Gower, L. B., Polymer-Induced Liquid-Precursor (PILP) Process in the Non-Calcium Based Systems of Barium and Strontium Carbonate. *Crystal Growth & Design* **2010,** 10, (3), 1040-1052.
56. Homeijer, S. J.; Olszta, M. J.; Barrett, R. A.; Gower, L. B., Growth of nanofibrous barium carbonate on calcium carbonate seeds. *Journal of Crystal Growth* **2008,** 310, (11), 2938-2945.
57. Wohlrab, S.; Cölfen, H.; Antonietti, M., Crystalline, porous microspheres made from amino acids by using polymer-induced liquid precursor phases. *Angewandte Chemie-International Edition* **2005,** 44, (26), 4087-4092.
58. Ma, Y. R.; Mehltretter, G.; Plug, C.; Rademacher, N.; Schmidt, M. U.; Cölfen, H., PY181 Pigment Microspheres of Nanoplates Synthesized via Polymer-Induced Liquid Precursors. *Advanced Functional Materials* **2009,** 19, (13), 2095-2101.
59. Boal, A. K.; Ilhan, F.; DeRouchey, J. E.; Thurn-Albrecht, T.; Russell, T. P.; Rotello, V. M., Self-assembly of nanoparticles into structured spherical and network aggregates. *Nature* **2000,** 404, (6779), 746-748.
60. Bronstein, L. H.; Sidorov, S. N.; Valetsky, P. M.; Hartmann, J.; Colfen, H.; Antonietti, M., Induced micellization by interaction of poly(2-vinylpyridine)-block-poly(ethylene oxide) with metal compounds. Micelle characteristics and metal nanoparticle formation. *Langmuir* **1999,** 15, (19), 6256-6262.
61. Antonietti, M.; Conrad, J.; Thünemann, A., POLYELECTROLYTE-SURFACTANT COMPLEXES - A NEW-TYPE OF SOLID, MESOMORPHOUS MATERIAL. *Macromolecules* **1994,** 27, (21), 6007-6011.
62. Perriman, A. W.; Colfen, H.; Hughes, R. W.; Barrie, C. L.; Mann, S., Solvent-Free Protein Liquids and Liquid Crystals. *Angewandte Chemie-International Edition* **2009,** 48, (34), 6242-6246.

63. Decher, G., Fuzzy nanoassemblies: Toward layered polymeric multicomposites. *Science* **1997,** 277, (5330), 1232-1237.
64. Cousin, F.; Gummel, J.; Ung, D.; Boue, F., Polyelectrolyte-protein complexes: Structure and conformation of each specie revealed by SANS. *Langmuir* **2005,** 21, (21), 9675-9688.
65. Turgeon, S. L.; Schmitt, C.; Sanchez, C., Protein-polysaccharide complexes and coacervates. *Current Opinion in Colloid & Interface Science* **2007,** 12, (4-5), 166-178.
66. Veis, A.; Aranyi, C., PHASE SEPARATION IN POLYELECTROLYTE SYSTEMS .1. COMPLEX COACERVATES OF GELATIN. *Journal of Physical Chemistry* **1960,** 64, (9), 1203-1210.
67. Bronstein, L. M.; Sidorov, S. N.; Gourkova, A. Y.; Valetsky, P. M.; Hartmann, J.; Breulmann, M.; Colfen, H.; Antonietti, M., Interaction of metal compounds with 'double-hydrophilic' block copolymers in aqueous medium and metal colloid formation. *Inorganica Chimica Acta* **1998,** 280, (1-2), 348-354.
68. Cooper, C. L.; Dubin, P. L.; Kayitmazer, A. B.; Turksen, S., Polyelectrolyte-protein complexes. *Current Opinion in Colloid & Interface Science* **2005,** 10, (1-2), 52-78.
69. Turgeon, S. L.; Beaulieu, M.; Schmitt, C.; Sanchez, C., Protein-polysaccharide interactions: phase-ordering kinetics, thermodynamic and structural aspects. *Current Opinion in Colloid & Interface Science* **2003,** 8, (4-5), 401-414.
70. Gummel, J.; Cousin, F.; Verbavatz, J. M.; Boue, F., Wide scale range structure in polyelectrolyte-protein dense complexes: Where Sans meets freeze-fracture microscopy. *Journal of Physical Chemistry B* **2007,** 111, (29), 8540-8546.
71. Lages, S.; Lindner, P.; Sinha, P.; Kiriy, A.; Stamm, M.; Huber, K., Formation of Ca2+-Induced Intermediate Necklace Structures of Polyacrylate Chains. *Macromolecules* **2009,** 42, (12), 4288-4299.
72. Gong, J.; Yao, P.; Duan, H. W.; Jiang, M.; Gu, S. H.; Chunyu, L., Structural transformation of cytochrome c and apo cytochrome c induced by sulfonated polystyrene. *Biomacromolecules* **2003,** 4, (5), 1293-1300.
73. Gotliv, B. A.; Addadi, L.; Weiner, S., Mollusk shell acidic proteins: In search of individual functions. *Chembiochem* **2003,** 4, (6), 522-529.
74. Huang, S. C.; Naka, K.; Chujo, Y., A carbonate controlled-addition method for amorphous calcium carbonate spheres stabilized by poly(acrylic acid)s. *Langmuir* **2007,** 23, (24), 12086-12095.
75. Faatz, M.; Grohn, F.; Wegner, G., Amorphous calcium carbonate: Synthesis and potential intermediate in biomineralization. *Advanced Materials* **2004,** 16, (12), 996-+.
76. Gower, L. B., Biomimetic Model Systems for Investigating the Amorphous Precursor Pathway and Its Role in Biomineralization. *Chemical Reviews* **2008,** 108, (11), 4551-4627.
77. Politi, Y.; Arad, T.; Klein, E.; Weiner, S.; Addadi, L., Sea urchin spine calcite forms via a transient amorphous calcium carbonate phase. *Science* **2004,** 306, (5699), 1161-1164.
78. Xu, A. W.; Yu, Q.; Dong, W. F.; Antonietti, M.; Colfen, H., Stable amorphous CaCO3 microparticles with hollow spherical superstructures stabilized by phytic acid. *Advanced Materials* **2005,** 17, (18), 2217-2221.
79. DiMasi, E.; Kwak, S. Y.; Amos, F. F.; Olszta, M. J.; Lush, D.; Gower, L. B., Complementary control by additives of the kinetics of amorphous CaCO3 mineralization at an organic interface: In-situ synchrotron x-ray observations. *Physical Review Letters* **2006,** 97, (4).
80. Schwahn, D.; Ma, Y. R.; Cölfen, H., Mesocrystal to single crystal transformation of D,L-alanine evidenced by small angle neutron scattering. *Journal of Physical Chemistry C* **2007,** 111, (8), 3224-3227.
81. Pipich, V.; Balz, M.; Wolf, S. E.; Tremel, W.; Schwahn, D., Nucleation and growth of CaCO3 mediated by the egg-white protein ovalbumin: A time-resolved in situ study using small-angle neutron scattering. *Journal of the American Chemical Society* **2008,** 130, (21), 6879-6892.

82. Kasai, H.; Nalwa, H. S.; Oikawa, H.; Okada, S.; Matsuda, H.; Minami, N.; Kakuta, A.; Ono, K.; Mukoh, A.; Nakanishi, H., A NOVEL PREPARATION METHOD OF ORGANIC MICROCRYSTALS. *Japanese Journal of Applied Physics Part 2-Letters* **1992,** 31, (8A), L1132-L1134.
83. Taden, A.; Landfester, K.; Antonietti, M., Crystallization of dyes by directed aggregation of colloidal intermediates: A model case. *Langmuir* **2004,** 20, (3), 957-961.
84. Bertorelle, F.; Lavabre, D.; Fery-Forgues, S., Dendrimer-tuned formation of luminescent organic microcrystals. *Journal of the American Chemical Society* **2003,** 125, (20), 6244-6253.
85. Ma, Y. R.; Börner, H. G.; Hartmann, J.; Cölfen, H., Synthesis of DL-alanine hollow tubes and core-shell mesostructures. *Chemistry-a European Journal* **2006,** 12, (30), 7882-7888.
86. Wohlrab, S.; Pinna, N.; Antonietti, M.; Cölfen, H., Polymer-induced alignment of DL-alanine nanocrystals to crystalline mesostructures. *Chemistry-a European Journal* **2005,** 11, (10), 2903-2913.
87. Lindfors, L.; Skantze, P.; Skantze, U.; Rasmusson, M.; Zackrisson, A.; Olsson, U., Amorphous drug nanosuspensions. 1. Inhibition of Ostwald ripening. *Langmuir* **2006,** 22, (3), 906-910.
88. Maier, N. M.; Franco, P.; Lindner, W., Separation of enantiomers: needs, challenges, perspectives. *Journal of Chromatography A* **2001,** 906, (1-2), 3-33.
89. Towler, C. S.; Davey, R. J.; Lancaster, R. W.; Price, C. J., Impact of molecular speciation on crystal nucleation in polymorphic systems: The conundrum of gamma glycine and molecular 'self poisoning'. *Journal of the American Chemical Society* **2004,** 126, (41), 13347-13353.
90. Lutsko, J. F.; Nicolis, G., Theoretical evidence for a dense fluid precursor to crystallization. *Physical Review Letters* **2006,** 96, (4), 046102/1-046102/4.
91. Weber, C. H. M.; Chiche, A.; Krausch, G.; Rosenfeldt, S.; Ballauff, M.; Harnau, L.; Gottker-Schnetmann, I.; Tong, Q.; Mecking, S., Single lamella nanoparticles of polyethylene. *Nano Letters* **2007,** 7, (7), 2024-2029.
92. Rill, R. L., LIQUID-CRYSTALLINE PHASES IN CONCENTRATED AQUEOUS-SOLUTIONS OF NA+ DNA. *Proceedings of the National Academy of Sciences of the United States of America* **1986,** 83, (2), 342-346.
93. Kobayashi, S.; Hobson, L. J.; Sakamoto, J.; Kimura, S.; Sugiyama, J.; Imai, T.; Itoh, T., Formation and structure of artificial cellulose spherulites via enzymatic polymerization. *Biomacromolecules* **2000,** 1, (2), 168-173.
94. Krebs, M. R. H.; MacPhee, C. E.; Miller, A. F.; Dunlop, L. E.; Dobson, C. M.; Donald, A. M., The formation of spherulites by amyloid fibrils of bovine insulin. *Proceedings of the National Academy of Sciences of the United States of America* **2004,** 101, (40), 14420-14424.
95. List, B., Proline-catalyzed asymmetric reactions. *Tetrahedron* **2002,** 58, (28), 5573-5590.
96. Schaffer, T. E.; IonescuZanetti, C.; Proksch, R.; Fritz, M.; Walters, D. A.; Almqvist, N.; Zaremba, C. M.; Belcher, A. M.; Smith, B. L.; Stucky, G. D.; Morse, D. E.; Hansma, P. K., Does abalone nacre form by heteroepitaxial nucleation or by growth through mineral bridges? *Chemistry of Materials* **1997,** 9, (8), 1731-1740.
97. Lange, F. F., Chemical solution routes to single-crystal thin films. *Science* **1996,** 273, (5277), 903-909.
98. Emanuele Treossi, A. L. X. F. V. P. K. M. P. S., Temperature-Enhanced Solvent Vapor Annealing of a C3 Symmetric Hexa-peri-Hexabenzocoronene: Controlling the Self-Assembly from Nano- to Macroscale. *Small* **2009,** 5, (1), 112-119.
99. van Hameren, R.; Schon, P.; van Buul, A. M.; Hoogboom, J.; Lazarenko, S. V.; Gerritsen, J. W.; Engelkamp, H.; Christianen, P. C. M.; Heus, H. A.; Maan, J. C.; Rasing, T.; Speller, S.; Rowan, A. E.; Elemans, J.; Nolte, R. J. M., Macroscopic hierarchical surface patterning of porphyrin trimers via self-assembly and dewetting. *Science* **2006,** 314, (5804), 1433-1436.

100. Grosso, D.; Cagnol, F.; Soler-Illia, G.; Crepaldi, E. L.; Amenitsch, H.; Brunet-Bruneau, A.; Bourgeois, A.; Sanchez, C., Fundamentals of mesostructuring through evaporation-induced self-assembly. *Advanced Functional Materials* **2004,** 14, (4), 309-322.
101. Aizenberg, J.; Black, A. J.; Whitesides, G. H., Oriented growth of calcite controlled by self-assembled monolayers of functionalized alkanethiols supported on gold and silver. *Journal of the American Chemical Society* **1999,** 121, (18), 4500-4509.
102. Xu, G. F.; Yao, N.; Aksay, I. A.; Groves, J. T., Biomimetic synthesis of macroscopic-scale calcium carbonate thin films. Evidence for a multistep assembly process. *Journal of the American Chemical Society* **1998,** 120, (46), 11977-11985.
103. Fricke, M.; Volkmer, D., Crystallization of calcium carbonate beneath insoluble monolayers: Suitable models of mineral-matrix interactions in biomineralization? In *Biomineralization I: Crystallization and Self-Organization Process*, Springer-Verlag Berlin: Berlin, 2007; Vol. 270, pp 1-41.
104. Sugawara, A.; Nishimura, T.; Yamamoto, Y.; Inoue, H.; Nagasawa, H.; Kato, T., Self-organization of oriented calcium carbonate/polymer composites: Effects of a matrix peptide isolated from the exoskeleton of a crayfish. *Angewandte Chemie-International Edition* **2006,** 45, (18), 2876-2879.
105. Amos, F. F.; Sharbaugh, D. M.; Talham, D. R.; Gower, L. B.; Fricke, M.; Volkmer, D., Formation of single-crystalline aragonite tablets/films via an amorphous precursor. *Langmuir* **2007,** 23, (4), 1988-1994.
106. Kim, Y. Y.; Douglas, E. P.; Gower, L. B., Patterning inorganic (CaCO3) thin films via a polymer-induced liquid-precursor process. *Langmuir* **2007,** 23, (9), 4862-4870.
107. Granasy, L.; Pusztai, T.; Tegze, G.; Warren, J. A.; Douglas, J. F., Growth and form of spherulites. *Physical Review E* **2005,** 72, (1), 15.
108. Weiner, S.; Wagner, H. D., The material bone: Structure mechanical function relations. *Annual Review of Materials Science* **1998,** 28, 271-298.
109. Sidorenko, A.; Krupenkin, T.; Taylor, A.; Fratzl, P.; Aizenberg, J., Reversible switching of hydrogel-actuated nanostructures into complex micropatterns. *Science* **2007,** 315, (5811), 487-490.
110. Oaki, Y.; Imai, H., Hierarchically organized superstructure emerging from the exquisite association of inorganic crystals, organic polymers, and dyes: A model approach towards suprabiomineral materials. *Advanced Functional Materials* **2005,** 15, (9), 1407-1414.
111. Rabani, E.; Reichman, D. R.; Geissler, P. L.; Brus, L. E., Drying-mediated self-assembly of nanoparticles. *Nature* **2003,** 426, (6964), 271-274.
112. Deegan, R. D.; Bakajin, O.; Dupont, T. F.; Huber, G.; Nagel, S. R.; Witten, T. A., Capillary flow as the cause of ring stains from dried liquid drops. *Nature* **1997,** 389, (6653), 827-829.
113. Wada, K., SPIRAL GROWTH OF NACRE. *Nature* **1966,** 211, (5056), 1427-&.
114. Cartwright, J. H. E.; Checa, A. G.; Escribano, B.; Sainz-Diaz, C. I., Spiral and target patterns in bivalve nacre manifest a natural excitable medium from layer growth of a biological liquid crystal. *Proceedings of the National Academy of Sciences of the United States of America* **2009,** 106, (26), 10499-10504.
115. Zaikin, A. N.; Zhabotin, A. M., CONCENTRATION WAVE PROPAGATION IN 2-DIMENSIONAL LIQUID-PHASE SELF-OSCILLATING SYSTEM. *Nature* **1970,** 225, (5232), 535-537.
116. Keller, A., Investigations on banded spherulites. *Journal of Polymer Science* **1959,** 39, (135), 151-173.
117. Sugawara, A.; Ishii, T.; Kato, T., Self-organized calcium carbonate with regular surface-relief structures. *Angewandte Chemie-International Edition* **2003,** 42, (43), 5299-5303.

118. Wang, T. X.; Xu, A. W.; Colfen, H., Formation of self-organized dynamic structure patterns of barium carbonate crystals in polymer-controlled crystallization. *Angewandte Chemie-International Edition* **2006,** 45, (27), 4451-4455.
119. Sakamoto, T.; Oichi, A.; Oaki, Y.; Nishimura, T.; Sugawara, A.; Kato, T., Three-Dimensional Relief Structures of CaCO3 Crystal Assemblies Formed by Spontaneous Two-Step Crystal Growth on a Polymer Thin Film. *Crystal Growth & Design* **2009,** 9, (1), 622-625.
120. Sakamoto, T.; Oichi, A.; Sugawara, A.; Kato, T., Self-organization of patterned CaCO3/polymer composite films: Tuning of their morphologies by the change of molecular weights of acidic polymers. *Chemistry Letters* **2006,** 35, (3), 310-311.
121. Sakamoto, T.; Oichi, A.; Nishimura, T.; Sugawara, A.; Kato, T., Calcium Carbonate/Polymer Thin-Film Hybrids: Induction of the Formation of Patterned Aragonite Crystals by Thermal Treatment of a Polymer Matrix. *Polymer Journal* **2009,** 41, (7), 522-523.
122. Kuznetsov, Y. G.; Malkin, A. J.; McPherson, A., Atomic-force-microscopy studies of phase separations in macromolecular systems. *Physical Review B* **1998,** 58, (10), 6097-6103.
123. Asakura, S.; Oosawa, F., INTERACTION BETWEEN PARTICLES SUSPENDED IN SOLUTIONS OF MACROMOLECULES. *Journal of Polymer Science* **1958,** 33, (126), 183-192.
124. McPherson, A.; Malkin, A. J.; Kuznetsov, Y. G., Atomic force microscopy in the study of macromolecular crystal growth. *Annual Review of Biophysics and Biomolecular Structure* **2000,** 29, 361-410.
125. Blank, S.; Arnoldi, M.; Khoshnavaz, S.; Treccani, L.; Kuntz, M.; Mann, K.; Grathwohl, G.; Fritz, M., The nacre protein perlucin nucleates growth of calcium carbonate crystals. *Journal of Microscopy-Oxford* **2003,** 212, 280-291.
126. Malkin, A. J.; Kuznetsov, Y. G.; McPherson, A., In situ atomic force microscopy studies of surface morphology, growth kinetics, defect structure and dissolution in macromolecular crystallization. *Journal of Crystal Growth* **1999,** 196, (2-4), 471-488.
127. Ross, F. M.; Tersoff, J.; Tromp, R. M., Coarsening of Self-Assembled Ge Quantum Dots on Si(001). *Physical Review Letters* **1998,** 80, (5), 984.
128. Malkin, A. J.; Land, T. A.; Kuznetsov, Y. G.; McPherson, A.; Deyoreo, J. J., INVESTIGATION OF VIRUS CRYSTAL-GROWTH MECHANISMS BY IN-SITU ATOMIC-FORCE MICROSCOPY. *Physical Review Letters* **1995,** 75, (14), 2778-2781.

Acknowledgement

The stay in MPIKG has been among my most enjoyable memories. The experience of working, entertaining, and sporting in a small village – Golm with a bunch of scientists is really memorable.

Firstly, I sincerely thank Prof. Markus Antonietti for allowing me to pursue my Ph.D. study under his extraordinary leadership. As a researcher, his diligence, curiosity and consistence always serve as a high standard that inspires me to develop myself throughout my ongoing career. I also thank him for helping me to make several important decisions and his deep patience during my thesis writing.

My thesis is mainly advised by Prof. Helmut Cölfen. He offered me a fantastic project to work on and was always available for discussion. He prefers those most meaningful and challenging projects to tackle with, which provided me a chance to go through the crystallization and colloid fields and to continue my career with clear goals.

My project was under the collaborations among three groups. Prof. Laurie Gower and Prof. Dirk Volkmer have been providing insight advice to my projects. I must thank the deep patience from physicists Dr. Dietmar Schwahn and Dr. Vitaliy Pipich when we worked together during the SANS measurements and data analysis. I am also thankful to Dr. Barbara Aichmayer, who worked a lot on my weak signals in SAXS measurements. Dr. Peter Cernoch's help in DLS & SAXS measurements is also highly appreciated.

I also owe a lot from people in the institute and around for their kindly and constructive advice. They are Dr. Klaus Tauer, Dr. Helmut Schladd, Dr. Hans Börner, Dr. Dayang Wang, Dr. Xinchen Wang, Dr. Jens Weber, and Dr. Jiayin Yuan. I appreciate the help from Dr. Robin White, Dr. Zoe Schnepp, and Dipl.-Chem. Andreas Picker for their kindly help for reading and correcting my thesis, despite of their hard work.

I would thank technicians who spent much time with my samples, especially Antje Völkel (AUC), Anne Hellig (AFM) and Margit Barth. I also thank our secretaries: Annette Pape, Annemarie Schulz, and Katja Schulze. I also show my thanks to the group members I overlapped with. I acknowledge the following undergraduate students I supervised: Eric Schönemann, Adria Suarez, Sarah Hutchinson, Felicia Svelund, and Harris Manning.

I would not reach this point without the love from my parents. They clarified the importance of education when I was a boy and respected every important decision I have made. My wife, Jing, always brings me delicious foods, deep patience and good taste and has been sharing every up and down with me. Their supports are the most valuable things to me. Finally, I am looking forward to meeting my son…….

Appendixes

1. Abbreviations

AUC	analytical ultracentrifugation
B	birefringence
(ρp-ρ0)2	contrast factor
C	solubility
CNT	classical nucleation theory
C_r	particle number concentration
C_s	saturated concentration
C_s^x	threshold concentration
D	diffusion coefficient
d	thickness
DFT	density function theory
e.v.	electron volt
əψ/əΩ	the differential cross section
f	frictional coefficient
f(θ)	wetting prefactor
F_0	focal length of the objective
F_b	buoyant force
F_f	frictional force
F_s	centrifuged force
F_t	focal length of the tube lens
g	the vector of the scattering center to the one integrating particle
G	rate of nucleation
Glu	DL-Glutamic acid
G_v	change of free energy per unit volume
His	L-Histidine
I	incident flux
I'	scattered flux
K	reactions rate coefficients
k	spring constant
k_B	Boltzmann's constant
L-L	liquid-liquid
Lys	DL-Lys·HCl
M	mobility of grain boundary
m	index number in the rate of grain growth
M_s	molar mass of solute
M_w	molecular weight
n	refractive index
N_A	avogadro constant
NMR	nuclear magnetic resonance

NP	nanoparticle
N_p/V	particle number density
OM	optical microscopy
P(q)	shape factor
PAA	polyacrylic acid
PEI	polyethyleneimine
PILP	polymer-induced liquid precursor
POM	polarized optical microscopy
Pro	L-Proline
q	scattering vector
r	radius
R	retardance
r*	critical size
R_g	the radius of gyration
s	incident wave vector
s'	scattered wave vector
S(q)	structure factor
Se	sedimentation coefficient
SEM	scanning electron microscopy
t	time
T'	transmission
T	absolute temperature
T*	critical temperature
TEM	transmission electron microscopy
u	velocity
u_B	velocity of grain boundary motion
u_s	rate of grain growth
ν	volume of molecule
V	volume
V_p	volume of one scattering body
WAXS	wide angle x-ray scattering
W	mass
X	molar fraction or composition
x	deflection
X*	critical molar fraction or critical composition
z	structural size
α	constant number in grain growth
β	interaction term
γ	surface tension
γ_b	average grain boundary energy per unit area of the grain boundary
γ_s	surface tension of a certain grain
ΔG^{mix}	Gibbs free energy of mixing
ΔG_s	energy loss for creating new interface
ΔG_v	energy gain for creating new volume

ΔH^{mix}	Enthalpy of mixing
ΔS^{mix}	Entropy of mixing
$\Delta\mu$	the driving force for grain growth
ε	detector efficiency
η	viscosity
θ	contact angle
λ	volume ratio
ρ	scattering length densities
ρ_{sol}	density of solvent
σ	interfacial tension
τ	induction time
Ω	solid angle
ω_{AB}	interaction between A and B
ω_r	angular velocity
$\bar{r}$	average radius
$\bar{v}$	partial specific volume
φ	the mass ratio of Glu/PEI
φ"	the mass ratio of His/PAA
φ"	the mass ratio of Lys/PAA

2. Experiments

Materials

DL-Glutamic acid monohydrate, L-Glutamic acid, D-Glutamic acid (Glu), and DL-Lys·HCl (Lys) are from Aldrich; polyethylenimine (PEI) with various Mws at 600, 1,300, 2,000 or 750,000 are from Aldrich; PAA, 63 wt% aqueous solution with Mw ~2,000 is from Acros Organics; the microscope cover slides from Fisher Scientific with 10 mm in diameter; CD_3OD is from Aldrich (99.8 atom % D); water is double distilled water; D_2O is from Aldrich (99.9 atom % D).

Chapter 4

1. Sample Preparation

A series of aqueous solutions containing various concentrations of Glu and PEI were prepared. Then, the aqueous solution was mixed with EtOH at different volume ratios. The mixture was heated in the oven at 40°C overnight and was left at 25°C for at least 24 h before the measurements.

2. Titration Measurements

A series of aqueous solutions were mixed with EtOH to determine the phase boundary of the quaternary system. The measurements were performed by dipping EtOH into the aqueous solution with stirring. After adding a certain volume of EtOH, the mixture became turbid and the EtOH volume was recorded. The measurements were performed at R.T.

3. NMR Measurements

After separating the coacervate phase from the supernatant phase by centrifuging samples at 7,000 rpm for 5 min, the solvent in both phases was evaporated thoroughly in the vacuum oven at 40°C for 24 h. Afterwards, 1 ml D_2O was added into the tube to solubilize the remaining solute for NMR measurements.

Section 5.2

A series of aqueous solutions containing a quantity of Glu and PEI were prepared. The solvent could be pure water, 1 M NaOH or 0.5 M H_2SO_4 aqueous solution. The above aqueous solution was stirred for 24 hours at 60°C or R.T. before it was quickly mixed with EtOH at various volume ratios. The mixture was then kept quiescent for 48 h at R.T. for the completing the precipitation. Finally, the precipitates were rinsed with EtOH for three times to remove the unbound PEI completely before characterization.

Section 6.1

First, aqueous solutions with various concentrations of Lys and PAA were prepared with double distilled water. Then, Lys-PAA aqueous solution was mixed with EtOH 1/9 (v/v). After being shaken for 10 seconds, the above dispersion was dipped onto the microscope cover slide with a micropipettor. The slide was left in air or in the oven for solvent evaporation for 24 hours.

Section 6.2

Firstly, an aqueous solution containing 70 $g \cdot L^{-1}$ Lys and 7 $g \cdot L^{-1}$ PAA was prepared by using double distilled water. Then, Lys-PAA aqueous solution was mixed with EtOH

1/9 (v/v). The white precipitates formed within 24 hours. After being sonicated for 1 min, 21 μL dispersion was dropped on the hydrophilic microscope cover slide with a micropipette. The slide was left in air for solvent evaporation for 24 hours.

Section 6.3

The procedure is similar to that in section 6.2. the only difference is that the aqueous solution used here contains 30 $g \cdot L^{-1}$ Lys and 3 $g \cdot L^{-1}$ PAA.

Section 6.4.1 & 6.4.2

With the same procedure described in Section 6.1, L-Lys·HCl was used instead of DL-Lys·HCl.

Chapter 7

First, a DL-Glu saturated solution was prepared at 50ºC. This solution was cool down to 20ºC for the formation of a supersaturated solution for AFM measurements. The scanning was directly on the surface of a DL-Glu·H_2O crystal. Both the crystal and tip were infiltrated into a droplet, which contains a supersaturated DL-Glu·H_2O mother liquor. The droplet volume is between 0.2 and 0.4 ml. In the blank experiments, the tip was immersed into the droplet which contains supersaturated DL-Glu·H_2O or water for the scanning. The scanning was performed directly on the silicon surface.

Characterization

Light microscopic images were taken with a Leica DMRB microscope and a birefingence microscope (LC-PolScope).

SEM measurements were performed on a LEO 1550 GEMINI.

AFM images were recorded on a multimode AFM (Veeco Instruments) with a tapping mode. Wide-angle X-ray scattering diffractograms were recorded on a Bruker D8 advance diffractometer.

Nitrogen sorption measurements were performed at 77K using a Quadrasorb machine from Quantachrome Instruments.

Metrohm - 716 DMS Titrino was used to measure the pH values of a series of aqueous solutions.

As to nuclear magnetic resonance measurements, the ^1H measurements were carried out on a Bruker-DMX 400 instrument at 25°C.

AUC experiments were performed on a XL-I ultracentrifuge (Beckman Coulter, PaloAlto, CA) equipped with a Raleigh interference optics. Other centrifugation experiments were performed on a preparative ultracentrifugation instrument.

The neutron experiments were performed using the KWS1 diffractometer at the FRM II at the Technische Universitaet, München. The experiments were performed with neutrons of 5, 12 and 19 Å in wavelength to find the appropriate Q range. The data obtained from the samples were corrected for the background scattering, sensitivity of the individual detector channels, and finally evaluated in an absolute scale from calibration with a secondary standard. The scattering from pure solvents were measured and used for background correction. The transmission describing the decrease of non-scattered neutrons by the sample was automatically measured for all spectra.

The time-resolved small-angle X-ray scattering (SAXS) measurements were performed on the beamline ID2. The wavelength is 1 nm and the measuring distance is 2 m and 8 m.

The static SAXS measurements were performed on a Nanostar Bruker AXS with the distance 25.5 cm. Samples for SANS and time-resolved SAXS measurements were mixed by using a stopped flow equipment, where there is no dead time for mixing.

Other Preparations

1. Cleaning of Glass Slide

The slides were rinsed in a solution containing an equal volumes of concentrated H_2SO_4 (96-98 wt%) and aqueous H_2O_2 solution (40 wt%) at R.T. for 24 hours before being used.

2. Glu Preparation

Glu was prepared by a recrystallization process. First, a supersaturated Glu aqueous solution was prepared by mixing DL-Glu·H_2O powder with water at 50°C. After the remaining powders were filtered out, the supersaturated aqueous solution was charged quickly into EtOH 1/9 (v/v). It took several days for Glu to precipitate completely, before the Glu powder was dried in a vacuum oven.

YUAN JIANG

The Max Planck Institute of Colloids and Interfaces (MPIKG) | Colloid Chemistry Department
Am Mühlenberg 1, Potsdam, 14476, Germany
Tel. +49 (331) 567 - 9513 | YUAN.JIANG@mpikg.mpg.de

RESEARCH INTERESTS

To understand multistep structural transformations in crystallization

To mimic crystallization with colloids (proteins, nanoparticles, and fullerenes) as building blocks

To synthesize functional materials via biomimetic routes

EDUCATION

01/08 - present	MPIKG, Germany	Ph.D. (expected)	physical chemistry
09/02 - 05/05	NANJING UNIVERSITY, China	M.S.	inorganic chemistry
09/98 - 06/02	SHANDONG UNIVERSITY, China	B.S.	chemistry

EXPERIENCE

08 – present, MPIKG, Germany

Advisors: Prof. Markus Antonietti & Prof. Helmut Cölfen

Aimed at the fundamental understanding of non-classical crystallizations

– Detected the transformation of liquid precursors into crystalline materials by using time-resolved small angle scatterings
– Extended the PILP route to the preparation of microspheres as well as biomimetic thin films
– Visualized the restructuring of clusters on a single crystalline layer with atomic force microscopy, which is the key step for the nucleation of a new molecular layer

06 – 07, UNIVERSITY AT BUFFALO, USA

– Teaching Assistants for *Principles of Chemical Engineering* & *Chemical Engineering Thermodynamics*

02 – 05, NANJING UNIVERSITY, China

Advisor: Prof. Zheng Xu

Designed for a series of patterned structures for the design of functional materials

– Constructed conjugated polymer (CP) and CP/fullerene nanotube arrays within alumina membranes with the wetting method
– Prepared colloidal crystals with monodisperse CP colloids as building blocks
– Fabricated monodisperse polymeric colloids and assembled them into colloidal crystals for the construction of Cu_2O and ZnO inverse opals
– Teaching Assistant for *College Chemistry Experiments*

1/02 – 5/02, THE SHANGHAI INSTITUTE OF ORGANIC CHEMISTRY, China

Advisors: Dr. Min Shi & Prof. Tongshan Sun

– Tested a series of Baylis-Hillman reactions by using imidazole as a catalyst
– Examined the chemical fixation of CO_2 fixation by using epoxy alkanes or alicyclic amines as a reactant and binaphthyldiamino Cu salen-type complexes as catalysts

PUBLICATIONS

In preparation

Jiang, Y.; Cölfen, H., et al., The Phase Diagram & Composition of Glu – PEI – Water – Ethanol System.

Jiang, Y.; Cölfen, H., et al., Characterization of Amino Acid/Polyelectrolyte Nanocomplexes in Aqueous Solution.

Jiang, Y.; Pipich, V.; Schwahn D.; Cölfen, H., The Mechanism of Precipitation from Metastable Polymer-induced Liquid Precursors

Jiang, Y.; Cölfen, H., et al., Two-Dimensional DL-Glu·H_2O Nucleation & Growth from Cluster Restructuring.

Jiang, Y.; Cölfen, H., et al., Hierarchical Macroporous Glutamic Acid Microspheres from Polymer-Induced Liquid Precursors.

Jiang, Y.; Cölfen, H., et al., Hierarchical Thin Films Combining Microsphere Reprecipitation and a Dewetting Process.

Jiang, Y.; Cölfen, H., et al., Self-Organized Hybrid Thin Films Combining Microsphere Reprecipitation and a Dewetting Process.

Jiang, Y.; Cölfen, H., et al., Mesocrystalline Thin Films from a Combination of Polymer-Induced Liquid Precursors and a Dewetting Process.

Published

Li, X.; **Jiang, Y.**; Shi, Z. W.; Xu, Z., Two growth modes of metal oxide in the colloidal crystal template leading to the formation of two different macroporous materials. *Chemistry of Materials* **2007,** 19, (22), 5424-5430.

Li, X.; Tao, F. F.; **Jiang, Y.**; Xu, Z., 3-D ordered macroporous cuprous oxide: Fabrication, optical, and photoelectrochemical properties. *Journal of Colloid and Interface Science* **2007,** 308, (2), 460-465.

Jiang, Y.; Li, X.; Liu, H. J.; Xu, Z.; Shen, X. P.; Ma, X.; Xue, Z. L., Fabrication of monodisperse colloidal array with confinement effects. *Chemical Communications* **2006**, (1), 75-77.

Tao, F. F.; Guan, M. Y.; **Jiang, Y.**; Zhu, J. M.; Xu, Z.; Xue, Z. L., An easy way to construct an ordered array of nickel nanotubes: The triblock-copolymer-assisted hard-template method. *Advanced Materials* **2006,** 18, (16), 2161-2164.

Jiang, Y.; Xu, Z., Preparation of an ordered array of PVK and PVK-C-60 nanotubes with template method. *Chinese Journal of Inorganic Chemistry* **2005,** 21, (9), 1389-1391.

Shen, X. P.; Liu, H. J.; Fan, X.; **Jiang, Y.**; Hong, J. M.; Xu, Z., Construction and photoluminescence of In_2O_3 nanotube array by CVD-template method. *Journal of Crystal Growth* **2005,** 276, (3-4), 471-477.

Shen, X. P.; Yuan, A. H.; Hu, Y. M.; **Jiang, Y.**; Xu, Z.; Hu, Z., Fabrication, characterization and field emission properties of large-scale uniform ZnO nanotube arrays. *Nanotechnology* **2005,** 16, (10), 2039-2043.

Shi, M.; **Jiang, Y.**, The Baylis-Hillman reactions of aldehydes with methyl vinyl ketone in the presence of imidazole, binol and silica gel. *Journal of Chemical Research-S* **2003**, (9), 564-566.

ORAL PRESENTATIONS

09/09, “Hybrid Mesocrystal Thin Films from Polymer-Induced Liquid Precursors,” 44th Biennial Meeting of the German Colloid Society, Hamburg, Germany.

09/09, “Hybrid Mesocrystal Thin Films from Polymer-Induced Liquid Precursors,” EUROMAT 2009, Glasgow, UK.

05/09, “Polymer-Induced Liquid Precursors in Amino Acid Crystallization Systems,” Summer School of Colloid Chemistry Department, MPIKG, Binz, Germany.

POSTERS

08/10, “Non-classical Routes in Organic Crystallizations,” The Gordon Research Conference on Biomineralization, New London, NH, USA.

06/09, “Polymer-Induced Liquid Precursors in Amino Acid Systems,” The 2009 Summer School on Amorphous Solids in Physics and Biology, Neuhardenberg, Germany.

06/09, “Polymer-Induced Liquid Precursors in Amino Acid Systems,” Annual Graduate Research Open House of MPIKG, Potsdam, Germany.

10/08, “Polymer-Induced Liquid Precursor in Amino Acid Systems,” Biological Approaches in Materials Sciences, Rottach-Egern, Germany.

10/07, “Carbon Nanotube Dispersion and Separation – Challenges and Opportunities,” Annual Graduate Open House of the Chemical & Biological Engineering Department, University at Buffalo, Buffalo, USA.

AWARDS

Excellent Students Leader(98 – 99), People’s Scholarship (98 – 01), Paper Award – Xiaoqing River Pollution Investigation Report (99), College Thesis Award – Baylis-Hillman Reaction Catalysis with Imidazole (02), SHANDONG UNIVERSITY.

Full Stipend with Graduate Tuition Scholarship, UNIVERSITY AT BUFFALO (06 – 07)

Max-Planck Society Scholarship (08 – 10)